A COMPUTATIONAL STUDY OF VORTEX RINGS INTERACTION WITH A CONSTANT-TEMPERATURE HEATED WALL

By

Hussam Hikmat Jabbar

A DISSERTATION

Submitted to
Michigan State University
in partial fulfillment of the requirements
for the degree of

Mechanical Engineering - Doctor of Philosophy

2020

ABSTRACT

A COMPUTATIONAL STUDY OF VORTEX RINGS INTERACTION WITH A CONSTANT-TEMPERATURE HEATED WALL

By

Hussam Hikmat Jabbar

This study is motivated by understanding the connections between the vortical structures in impinging jets and the wall heat transfer. The particular objectives of the study are: (1) examining how the stage of evolution of vortex pairing in the jet might influence the wall heat transfer; (2) establishing correlations between the vortex characteristics and the Nusselt number (Nu) distribution; (3) exploring the physics of the thermal boundary layer behavior and the associated near-wall flow that causes the enhancement and the deterioration in heat transfer during vortex-wall interaction; and finally (4) evaluating a newly published hypothesis of the mechanisms of the heat transfer enhancement and deterioration during this interaction.

To address the first two objectives, CFD simulations are conducted of three simplified model problems involving the interaction of isolated axisymmetric vortex rings with a flat, constant-temperature, heated wall. The cases represent three scenarios of vortex-wall interaction: before (Case I), during (Case II) and after (Case III) pairing. The results show that when two vortices concurrently interact with the wall and undergo pairing (Case II), a significant instantaneous enhancement in Nu is attained in comparison to that associated with a single vortex interacting with the wall (Cases I and III). In all three cases, a deterioration in Nu is observed simultaneously with the enhancement (but at different radial locations) due to the formation of the secondary vortex (SV). However, the net effect of vortex-wall interaction on the heat transfer remains positive with Case II producing the highest heat transfer rate than the other cases.

Two additional CFD cases are conducted to address the third objective. Both cases are the same as Case I except for one parameter. In the first of the additional cases, the thermal diffusivity is set to zero ($\alpha = 0$) to understand the role of diffusion in heat transfer enhancement. Analysis of this case is complemented with a simple analytical model based on the unsteady 1D energy equation with wall-normal (axial) velocity perturbation. The results lead to the hypothesis that the axial velocity induced by the primary vortex (PV) toward the wall is the main factor for enhancement of the heat transfer on the downwash side of the vortex core by causing thinning of the thermal boundary layer (TBL). Thermal diffusion is found to limit this enhancement and cause the TBL to thicken when the downwash velocity weakens.

In the second of the additional cases, the wall shear stress is set to zero ($\tau = 0$) to eliminate separation of the boundary layer, and hence evaluate the role of separation in deterioration of Nu. As in the case of Nu enhancement, the results show that the axial velocity is the leading factor driving the Nu deterioration. Surprisingly, eliminating separation leads to even smaller minimum Nu; found to be caused by closer approach of the PV toward the wall in the absence of the secondary vortex (due to separation elimination). Nevertheless, the overall effect of eliminating separation is positive since the closer proximity of the PV to the wall also causes significant Nu enhancement on the downwash side, producing a net positive Nu change.

Finally, trajectories of selected fluid particles are tracked in a thermofluidic boundary-layer-resolved Lagrangian analysis in order to evaluate a recently published "surface renewal model" that explains the mechanisms of heat transfer due to vortex-wall interaction. The results show that while some elements of this hypothesis, regarding the heat transfer enhancement on the downwash side, are valid, the hypothesis is based on the wrong physics when it comes to the heat transfer deterioration on the upwash side.

Copyright by HUSSAM HIKMAT JABBAR 2020 Dedicated to the memory of my father, to my mother, my loving wife, and my kids

ACKNOWLEDGMENTS

First, I would like to sincerely thank my wife Fatma for her love, patience and support, and I want to tell her that, without you, my life would have been so hard while getting the PhD degree. You are the one who has made this journey so much easier and enjoyable; this will last in my heart and my mind forever. Thanks to my kids, Hasan and Hikmat, who were a relief of stresses in my daily life. The love, care, tenderness, and cordiality I owe you are beyond what I can say.

I also would like to thank my family. My Dad, who passed away as I started my PhD program: "Thank you for believing in me. I did not disappoint you, and I never will. I know your eyes are around me to keep me safe, and that you pray for me all the time". Thanks to my Mom for everything, and specially for your prayers that never let me down.

Special thanks to my advisor, Dr. Ahmed Naguib for his advice, support, patience during (what he calls) "the education process", he broadened my viewpoint about getting the Ph.D. degree beyond the scientific aspect.

Special thanks to all my colleagues and friends who gave me the support, advice, comments and help, even with words, to make my life and getting the degree much easier than I thought.

I would like to thank and acknowledge the Higher Committee of Education Development in Iraq (HCED) for providing the financial support for my studies, and I would also like to thank all the great staff administering the award. I would like to acknowledge the support of National Science Foundation for partially funding this project through NSF grant number CBET-1603720.

Finally, a sincere and special thanks to all the unsung heroes who sacrifice their lives and lifetimes to make others' lives a better life.

TABLE OF CONTENTS

LIST OF FIGURES	
LIST OF TABLES	
CHAPTER 1 INTRODUCTION	
1.1. Background	
1.1.1. Impinging Conventional Jets	
1.1.2. Impinging Synthetic Jets	
1.1.3. Heat Transfer from Vortex-Wall Interaction Arising in Jets or in	
Isolation	
1.2. Motivation and Scope	
1.3. Objectives	
•	
CHAPTER 2 COMPUTATIONAL DETAILS AND VALIDATION	
2.1. Validation of the Computational Approach: Set-A Computations	
2.2. Main Computations: Set- <i>B</i> Computations	
2.3. Additional Computation: Set-C Computations	
•	
CHAPTER 3 VORTEX-WALL INTERACTION AND HEAT TRANSFER	
3.1. General Considerations	
3.1.1. Normalization	
3.1.2. Calculation of Vortex Characteristics	
3.1.3. Wall Friction Coefficient and Nusselt Number Calculation	
3.1.4. Separation Detection	
3.2. Evolution of the Flow Field and Nusselt Number	
3.3. Heat Transfer Enhancement: Maximum <i>Nu_r</i>	
3.4. Heat Transfer Deterioration: Minimum <i>Nu_r</i>	
3.5. Overall Effect: Average Nu_r	
CHAPTER 4 BOUNDARY-LAYER-RESOLVED ANALYSIS OF NUSSELT	
NUMBER BEHAVIOR	
4.1. Eulerian Analysis	
4.1.1. Maximum Nu_r : Case I and Case $\alpha = 0$ Comparison	
4.1.2. Thermal Boundary Layer Profiles and Nusselt Number Based on TBI	\mathcal{L}
Thickness	,
4.1.3. Analytical Model	
4.1.4. Minimum Nu_r : Case I and Case $\tau = 0$ Comparison	
4.2. Lagrangian Analysis	
4.2.1. Description of the Surface Renewal Model	
4.2.2 Evaluation of the Surface Renewal Model	

CHAPTER 5 CONCLUSIONS AND RECOMMENDATIONS	124
5.1. Vortex Rings-Wall Interaction and Heat Transfer	124
5.2. Heat Transfer Mechanism	126
5.3. Recommendations	130
APPENDICES	132
APPENDIX A: Computational Validation	133
APPENDIX B: Derivation of Q Value in Cylindrical Coordinate	142
APPENDIX C: 1D Model Solution	147
BIBLIOGRAPHY	156

LIST OF FIGURES

Figure 1.1	A schematic of the normally impinging conventional jet	3
Figure 1.2	Schematic of a synthetic jet during the suction (top) and the ejection (bottom) phase	4
Figure 1.3	Time-resolved flow visualization and concurrent radial wall-pressure distribution of an axisymmetric impinging jet at four time instants, as indicated on top of the images. The impingement wall is located at $z/D = 2$, and the jet centerline at $r/D = 0$. Yellow arrows track the pairing of two vortices. Seen in the figure is the development of a strong negative surface-pressure spike in the wall-jet region $(r/D > 1)$ from an initially broad negative peak of approximately -2 Pa at $r/D \approx 0.9$ and time $t = 5$ ms (top left plot), to a focused negative peak of -7 to -8 Pa at $r/D \approx 1.3$ and time $t = 8$ ms (bottom right plot). The jet exit velocity is 4.3 m/s and the jet Reynolds number based on diameter and exit velocity is $Re_D = 7,334$. Based on Al-Aweni [23]	11
Figure 2.1	Effect of the grid resolution (a) and the computational time step (b) on the temporal evolution of the peak vorticity within the core of the primary vortex. Computations are done using experimental data from Gendrich et $al.$ [14] as initial condition. The legend in the left plot shows the number of grid elements in the r and z directions, while the legend in the right plot provides the computational time step size	18
Figure 2.2	Comparison between the experimental and the computational results of the temporal evolution of the maximum and minimum vorticity value in the core of the primary (PV) and the secondary (SV) vortices respectively. The origin of the time axis is based on the experiments of Gendrich <i>et al.</i> [14] and it corresponds to the time of the velocity field data employed to initialize the computation	20
Figure 2.3	Comparison between the experimental and the computational results of the trajectories of the primary and the secondary vortices (PV and SV respectively)	21
Figure 2.4	Comparison between the experimental and the computational results of the temporal evolution of the maximum vorticity value of the boundary layer (BL). The origin of the time axis is based on the experiments of Gendrich <i>et al.</i> [14] and it corresponds to the time of the velocity field data employed to initialize the computation	22

Figure 2.5	Sketch illustrating the computational domain and boundary and initial conditions for Cases II and III of computational set B : a) a pair of Gaussian-core vortices (Case II); b) a single Gaussian-core vortex with twice the initial circulation and core radius (Case III). The problem setup of Case I is the same as Case II with the only difference being the removal of the inner vortex. The computational domain spans only one single azimuthal plane due to flow axisymmetry. The flow visualization images on top are taken from Al-Aweni [23] and are used to determine R_o and Z_o shown on the corresponding sketches on bottom	25
Figure 2.6	a) Temporal evolution of the wall-normal temperature profile obtained from Equation 2.9. The profile evolves monotonically in the direction indicated by the arrow. Different times are represented by different line colors, with the time step between two successive lines equal to $5\Delta t$. The thick solid black line outlines the temperature profile selected to initialize the temperature field; b) The initial temperature field of the computational domain, with a magnification of the TBL	29
Figure 2.7	Comparison of the number of the grid points (n) within $\delta_{th,min}$ for Case I and Case $\alpha=0$ versus time. The number of grid points is depicted as fractional multiple of the grid spacing. The actual number of grid points, which is an integer, is the largest integer number below the value shown.	31
Figure 2.8	The evolution of $Nu_{r,max}$ calculated using different orders of accuracy of the finite difference applied to data from; a) CFD on the old computational mesh; b) Lagrangian-Eulerian (L-E) passive scalar evaluation on the new fine mesh. Plot (a) also contains the second-order finite-difference result from plot (b) for direct comparison	34
Figure 3.1	Figure 3.1 Vorticity distribution of a Gaussian vortex demonstrating the vortex border as defined by the core radius and the Q-criterion (Equation 3.1)	39
Figure 3.2	Time evolution of the vorticity field (Case I), showing an example snapshots during the early stages of SV formation. The broken red line represents the SV border calculated by the Q-criterion	40
Figure 3.3	a) and b) show two snapshots of the normalized near-wall vorticity field and the concurrent radial distribution of the wall friction coefficient (C_f) and Nusselt number (Nu_r) of Case I. The ordinate is stretched relative to the abscissa in the vorticity-field plot to magnify the view, distorting the appearance of the flow features	42

Figure 3.4	Time evolution of the initially-Gaussian-core vortex as it interacts with a heated wall (Case I). Shown at each time instant: the azimuthal-vorticity field (top), the near-wall temperature field (middle) and line plots (bottom) of Nusselt number (Nu_r) and the wall-friction coefficient (C_f). The broken gray line represents the primary separation point of the hydrodynamic boundary layer beneath the PV, and the broken black line depicts the location of the minimum δ_{th}	46
Figure 3.5	Time evolution of the two initially-Gaussian-core vortex rings as they interact with a heated wall (Case II). Shown at each time instant: the azimuthal-vorticity field (top), the near-wall temperature field (middle) and line plots (bottom) of Nusselt number (Nu_r) and the wall-friction coefficient (C_f). The broken gray line represents the primary separation point of the hydrodynamic boundary layer beneath the PV, and the broken black line depicts the location of the minimum δ_{th}	47
Figure 3.6	Time evolution of the initially-Gaussian-core vortex (with twice the initial circulation and core radius of Case I) as it interacts with a heated wall (Case III). Shown at each time instant: the azimuthal-vorticity field (top), the near-wall temperature field (middle) and line plots (bottom) of Nusselt number (Nu_r) and the wall-friction coefficient (C_f). The broken gray line represents the primary separation point of the hydrodynamic boundary layer beneath the PV, and the broken black line depicts the location of the minimum δ_{th}	48
Figure 3.7	Comparison of the maximum Nusselt number evolution with time for the one- and the two-vortex rings interacting with a heated wall: a) dimensional, and b) non-dimensional time. The semi-infinite transient-diffusion solution (based on Equation 2.9) is included for reference in (a)	50
Figure 3.8	Comparison of the temporal evolution of the total circulation associated with the primary vorticity for the one- and the two- vortex rings interacting with a heated wall: a) dimensional; and b) non-dimensional plot	51
Figure 3.9	Temporal evolution of the radial locations of the maximum local Nusselt number, the maximum wall friction coefficient, the minimum TBL thickness, and the core center of the primary vortex: a) Case I; b) Case II; c) Case III. The magenta line in (b) displays the average of the radial loci of the inner and the outer vortex cores	55

Figure 3.10	Temporal evolution of the maximum local Nusselt number, the minimum TBL thickness, and the wall-normal location of the core center of the primary vortex: a) Case I; b) Case II; c) Case III. The magenta line in (b) displays the average of the radial loci of the inner and the outer vortex cores	56
Figure 3.11	Comparison of the minimum Nusselt number evolution with time for the one- and the two- vortex rings interacting with a heated wall: a) dimensional; and b) non-dimensional time. The semi-infinite transient-diffusion solution (based on Equation 2.9) is included for reference in (a)	57
Figure 3.12	Temporal evolution of the radial locations of the $Nu_{r,min}$, the primary separation point and the core center of the primary vortex: a) Case I; b) Case II; c) Case III. The magenta line in (b) displays the average of the radial loci of the inner and the outer vortex cores	59
Figure 3.13	Temporal evolution of the $Nu_{r,min}$ and the wall-normal location of the core of the primary vortex: a) Case I; b) Case II; c) Case III. The magenta line in (b) displays the average of the radial loci of the inner and outer vortex cores	60
Figure 3.14	A snapshot of the evolution of vortex-wall interaction for Case I, demonstrating the two criteria used to define the radial domain boundary for calculation of the radially-averaged $Nu_r(t)$: vorticity field (top) and concurrent radial distribution of the Nusselt number (bottom). The figure shows the SV at its maximum radial location. (I) and (II) in the figure represent, respectively, the maximum radial location of the SV, and the radial location where Nu_r deviates by 10% from the unsteady diffusion value	62
Figure 3.15	Comparison of the radially-averaged Nusselt number evolution with time for the one- and the two-vortex rings interacting with a heated wall: a) dimensional; and b) non-dimensional time. The semi-infinite transient-diffusion solution (based on Equation 2.9) is included for reference in (a)	63
Figure 3.16	Temporal evolution of the SV circulation for all three cases	65
Figure 3.17	Trajectory of the core center of the PV (for Cases I and III), and the inner vortex (for Case II). The black markers on each trajectory show the initial position of the PV, while the similar-shaped colored markers on the same line indicate the initial time of formation of SV	66

Figure 4.1	Evolution of $Nu_{r,max}$ with time for Case I and Case $\alpha = 0$. The vertical black broken lines represent the selected time steps that are used for comparison between the two cases	70
Figure 4.2	Time evolution of the initially-Gaussian-core vortex ring as it interacts with a heated wall: left (Case I) and right (Case $\alpha = 0$). Shown at each time instant: the azimuthal-vorticity field and velocity-field vectors (top), the near-wall temperature field (middle) and a line plot (bottom) of Nusselt number (Nu_r). The broken black line depicts the location of the maximum Nu_r . In snapshots c through f, $Nu_{r,max}$ for $\alpha = 0$ (right column) is scaled before plotting to fit in a similar plot window as shown in the left column. The scaling factor is included in the axis label.	72
Figure 4.3	Temporal evolution of the radial location of the maximum local Nusselt number for Case I and Case α =0	75
Figure 4.4	a) Temporal evolution of $Nu_{r,max}$, for Case I and Case $\alpha=0$, and the wall-normal location of the core center of the PV. For Case $\alpha=0$, $Nu_{r,max}$ is divided by a factor of 3 to fit on the same plot with Case I. b) The temporal evolution of the rate of change of $Nu_{r,max}$ for Case $\alpha=0$, and the wall-normal location of the core center of the PV	76
Figure 4.5	Normalized temperature profiles versus the axial coordinate scaled with δ_{th} : a) Case I, and; b) Case $\alpha=0$. The solid black curve represents the unsteady diffusion solution normalized in the same manner as the other profiles. The temperature profiles chosen at the radial location of $Nu_{r,max}$ for different time steps.	77
Figure 4.6	Evolution of $Nu_{r,max}$, scaled with δ_{th} , for Case I and Case $\alpha=0$. The broken black line represents the unsteady-diffusion theoretical value obtained from Equation 4.4	79
Figure 4.7	Evolution of $Nu_{r,max}$ and minimum thickness of TBL $(\delta_{th,min})$; a) Case I; and b) Case $\alpha=0$	80
Figure 4.8	Sketch of the problem of one-dimensional thermal boundary layer with uniform suction	81
Figure 4.9	a) Amplitude, and b) phase shift response of the unsteady temperature gradient at the wall due to harmonic variation in the suction velocity in the form $-v_0\cos(\hat{\omega}t^*)$	86

Figure 4.10	a) Evolution of Nu and the normalized axial velocity of the first node above the wall, and; b) Evolution of Nu and the TBL thickness, at $(r - R_o)/a_o \approx 1$, where the maximum of $Nu_{r,max}$ of Case I occurs. The black broken line in (a) shows the zero value of u_z^*	88
Figure 4.11	Normalized temperature profiles versus the axial coordinate scaled with δ_{th} at $(r - R_o)/a_o \approx 1$, the same radial location considered in Figure 4.10, for Case I. The solid black curve represents the unsteady diffusion solution normalized in the same manner as the other profiles	89
Figure 4.12	Time evolution of the initially-Gaussian-core vortex ring as it interacts with a heated wall (Case I) in the original Eulerian frame of reference (as in Chapter 3). Shown at each time instant: the azimuthal-vorticity field and velocity-field vectors (top) and the near-wall temperature field (bottom). The broken black line depicts the location of the maximum of $Nu_{r,max}$ at $((r-R_o)/a_o \approx 1)$	90
Figure 4.13	a) the evolution of Nu and the normalized axial velocity of the first node above the wall, and b) the evolution of Nu and $I^* = \int_0^t -u_z^*(t)dt$, at $((r-R_o)/a_o \approx 1)$ for Case $\alpha=0$	91
Figure 4.14	a) Normalized radial location of $Nu_{r,min}$ and the primary separation point illustrates the three regions of study; b) TBL normalized temperature profiles at the selected time instants. The semi-infinite unsteady diffusion temperature profile is added for reference	95
Figure 4.15	a) Temporal evolution of $Nu_{r,min}$; b) Temporal evolution of $Nu_{r,max}$ for Case I and Case $\tau = 0$.	96
Figure 4.16	Temporal evolution of $Nu_{r,avg}$ (see Equation 4.28) for Case I and Case $\tau=0$	97
Figure 4.17	Time evolution of the initially-Gaussian-core vortex rings as they interact with a heated wall: Case I (left) and Case $\tau = 0$ (right). Shown at each time instant: the azimuthal-vorticity field and the velocity field vectors (top), the near-wall temperature field (middle) and line plots (bottom) of Nusselt number (Nu_r) . The broken black line depicts the location of the $Nu_{r,min}$ while the broken white line depicts the ridge of thickest TBL	100
Figure 4.18	a) Temperature profiles normalized by the core radius of the PV and; b) normalized wall-normal velocity profiles, for the six selected time steps: Case I (top) and Case $\tau = 0$ (bottom)	105

Figure 4.19	Temporal evolution of the $Nu_{r,min}$ and the wall-normal location of the core of the PV. a) Case I; b) Case τ =0	106
Figure 4.20	Temperature profiles normalized by the TBL thickness at the six selected time steps for Case $\tau=0$. The profiles are the same as in the bottom of Figure 4.18a but with different normalization of z	107
Figure 4.21	Radial distribution of u_z^* at the first grid point above the wall concurrently with the radial distribution of Nu_r at the six selected time steps. a) Case I; b) Case $\tau = 0$. In (b) Nu_r is divided by a factor of 2 for $t^* \ge 21.3$ to fit the results on the same scale as at other times.	109
Figure 4.22	The temporal evolution of the normalized radial location of $u_{z,max}^*$ and $Nu_{r,min}$. a) Case I; b) Case $\tau = 0$	109
Figure 4.23	a) Temporal evolution of the radial location of $Nu_{r,min}$ and the PV core center for Case I and Case $\tau=0$; b) Normalized offset from the PV core center $(r_{Nu_{r,min}}-R_{PV})$ for Case I and Case $\tau=0$. The black broken line in (b) represents the average of the offset for (Case $\tau=0$)	111
Figure 4.24	a) Schematic used in "surface-renewal" model development; b) qualitative illustration of the convective-heat transfer augmentation prediction (Equation (4.32)) as a function of non-dimensional location y/L from the vortex core center. The figure is reproduced from a sketch in Hubble <i>et al.</i> [22]	112
Figure 4.25	Temporal evolution of; a) $Nu_{r,max}$; and b) $Nu_{r,min}$, showing the selected time instants at which particles are identified and tracked backward in time	117
Figure 4.26	The trajectories of the selected particles: a) $Nu_{r,max}$; b) $Nu_{r,min}$. The black markers on each plot indicate the starting time of backward integration (shown in the legend) to calculate the particle trajectory history and the arrows indicating the initial position of the particles	120
Figure 4.27	Evolution of the temperature of the selected particles: a) $Nu_{r,max}$; b) $Nu_{r,min}$. The black markers on each plot indicate the starting time of backward integration (shown in the legend) to calculate the particle trajectory and temperature history before reaching the wall. Noting that $(\theta = 0)$ corresponding to the higher temperature	121

Figure 4.28	History of the rate of temperature rise of the selected particles: a) $Nu_{r,max}$; b) $Nu_{r,min}$. The black markers on each plot indicate the starting time of backward integration (shown in the legend) to calculate the particle trajectory and temperature history before reaching the wall.	121
Figure A.1	Evolution of the maximum vorticity at the core center of the PV for different grid resolutions and a domain size of $0.06 \text{ m} \times 0.06 \text{ m}$	133
Figure A.2	Evolution of the maximum vorticity at the core center of the SV for different grid resolutions and a domain size of $0.06 \text{ m} \times 0.06 \text{ m}$	134
Figure A.3	Evolution of the maximum vorticity of the BL for different grid resolutions and a domain size of 0.06 m \times 0.06 m.	134
Figure A.4	Evolution of the maximum of Nu_r for different grid resolutions and a domain size $0.06 \text{ m} \times 0.06 \text{ m}$	135
Figure A.5	Evolution of the maximum vorticity at the center of the PV for two different domain sizes while keeping the same grid resolution (0.00012 m)	135
Figure A.6	Evolution of the maximum vorticity at the center of the SV for two different domain sizes while keeping the same grid resolution (0.00012 m).	136
Figure A.7	Evolution of the maximum vorticity of the BL for two different domain sizes while keeping the same grid resolution (0.00012 m)	136
Figure A.8	Evolution of the maximum of Nu_r for two different domain sizes while keeping the same grid resolution.	137
Figure A.9	Evolution of the maximum vorticity at the center of the PV for different time-step sizes, and a domain size of $0.06~\text{m}\times0.06~\text{m}$ and $715\times715~\text{grid}$ elements.	137
Figure A.10	Evolution of the maximum vorticity at the center of the SV for different time-step sizes, and a domain size of $0.06~\text{m}\times0.06~\text{m}$ and $715\times715~\text{grid}$ elements.	138
Figure A.11	Evolution of the maximum vorticity of the BL for different time-step sizes, and a domain size of $0.06 \text{ m} \times 0.06 \text{ m}$ and $715 \times 715 \text{ grid elements}$	138

Figure A.12	Evolution of the maximum of Nu_r for different time-step sizes, and a domain size of $0.06 \text{ m} \times 0.06 \text{ m}$ and $715 \times 715 \text{ grid elements}$	139
Figure A.13	Evolution of the maximum vorticity at the center of the PV for different number of iterations, and a domain size of $0.06~\text{m}\times0.06~\text{m}$ and $715\times715~\text{grid}$ elements. The legend shows the number of iterations	139
Figure A.14	Evolution of the maximum vorticity at the center of the SV for different number of iterations, and a domain size of $0.06~\text{m}\times0.06~\text{m}$ and $715\times715~\text{grid}$ elements. The legend shows the number of iterations	140
Figure A.15	Evolution of the maximum vorticity of the BL for different number of iterations, and a domain size of 0.06 m \times 0.06 m and 715 \times 715 grid elements. The legend shows the number of iterations.	140
Figure A.16	Evolution of the maximum of Nu_r evolution for different number of iterations, and a domain size of 0.06 m \times 0.06 m and 715 \times 715 grid elements. The legend shows the number of iterations	141

LIST OF TABLES

Table 2.1	Maximum percentage errors for the results in Appendix A	27

CHAPTER 1

INTRODUCTION

1.1. Background

The present study is motivated by impinging jet flows. One of the most common uses of these jets is the heating and cooling of the impingement surface, because of their ability to produce high heat transfer rates. Many studies exist on characterizing this heat transfer process, and on relating these characteristics to the flow parameters and features; e.g. see Jambunathan *et al.* [1], Carlomagno and Ianiro [2] and references therein. In existing works, connections between the jet vortices and the heat transfer are described from a phenomenological point of view without establishing a quantitative correlation between the characteristics and evolution of the vortices and the surface heat transfer. Such information is necessary to formulate a robust, in-depth understanding of how the interaction of the jet vortices with the impingement wall affects the convective heat transfer coefficient. The resulting insight should be valuable for developing effective flow control strategies to improve the heating/cooling effectiveness of impinging jets.

To focus on understanding the physics of the wall thermal transport in the presence of vortex-wall interaction, the present investigation considers simple model problems involving the interaction of isolated vortex rings with a heated wall in the absence of the jet flow. Before discussing existing knowledge on the heat transfer from vortex-wall interaction, a very brief summary is provided of the main features of impinging conventional and synthetic jets. This is followed with a review of studies of the influence of the vortical structures on wall heat transfer, either as features of an impinging jet or as isolated vortices interacting with the wall.

1.1.1. Impinging Conventional Jets

Impinging jets are widely used in industrial and manufacturing processes. The flow configuration of an impinging jet consists of a jet flow impinging on a surface, which is typically a flat plate (see Figure 1.1). There are several classifications of impinging jets, depending on different factors. For example, the angle of impingement of the jet (oblique or normal relative to the wall), the shape of the jet exit (round, slit, etc.), among others. Regardless of the classification, the flow is characterized by three main regions. The free jet region, which extends from the jet exit to the point where there is no significant influence due to the presence of the wall. In this region, the flow acts as a free jet, and the shear layer of the jet is inviscibly unstable such that small disturbances can grow exponentially immediately downstream of the jet exit. The early amplification of these shear layer disturbances can be predicted using linear stability theory; e.g. see Drubka et al [3] and Drazen [4]. The initial instability ultimately leads to "rolling up" of the shear layer to form vortices which in turn interact with each other and merge as they move farther downstream from the jet exit; e.g. see Michalke [5] and Popiel and Trass [6]. The merging of the vortices was studied by Ho and Huang [7] in a free shear layer. By controlling the forcing frequency of the shear layer, they were able to control the number of vortices involved in the merging process. In a natural jet, merging typically occurs between vortex pairs, leading to doubling of the vortex size and halving of the vortex-passing frequency. This mechanism leads to the growth of the jet shear layer, to ultimately reach the jet centerline at the end of the potential core.

The second region is the stagnation region, which corresponds to the zone where there is a change in the main flow direction from being normal to being parallel to the wall, and the flow becomes directed outwards in the radial direction (r). This region is typically defined to extend

from the jet centerline to r/D = 1. The third region is the wall-jet region, in which the mean flow takes the form of a wall jet. In this zone, which is established for r/D > 1, unsteady boundary layer separation occurs due to the interaction of the jet vortices with the wall. This separation frequently leads to the formation of a secondary vortex with an opposite sense of vorticity to that of the jet vortices; e.g. see Walker *et al.* [8].

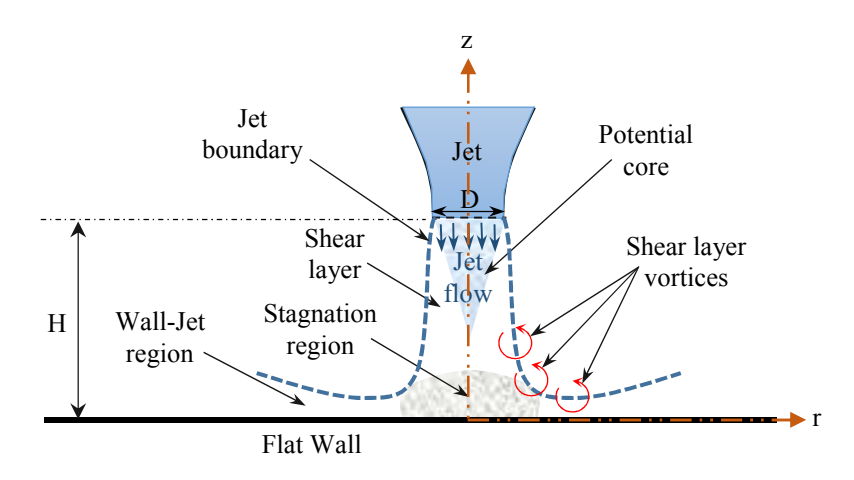


Figure 1.1 A schematic of the normally impinging conventional jet.

1.1.2. Impinging Synthetic Jets

A synthetic jet is different from a conventional jet in that, while the former adds mean momentum to the fluid as the latter, the synthetic jet has zero net mass flow rate through the jet orifice. As illustrated in Figure 1.2, a typical synthetic jet consists of a cavity with an oscillating diaphragm forming one of the cavity walls, and an orifice existing in one of the other walls. The oscillating diaphragm generates suction and ejection of the fluid, which leads to the production of vortical structure during the ejection phase. The vortices advect away from the orifice by their self-induced velocity. Unlike free jets, vortex merging has not been observed to occur in synthetic jets. For more information, see Glezer and Amitay [9], for non-impinging synthetic jets, and Greco *et al.* [10], for impinging ones.

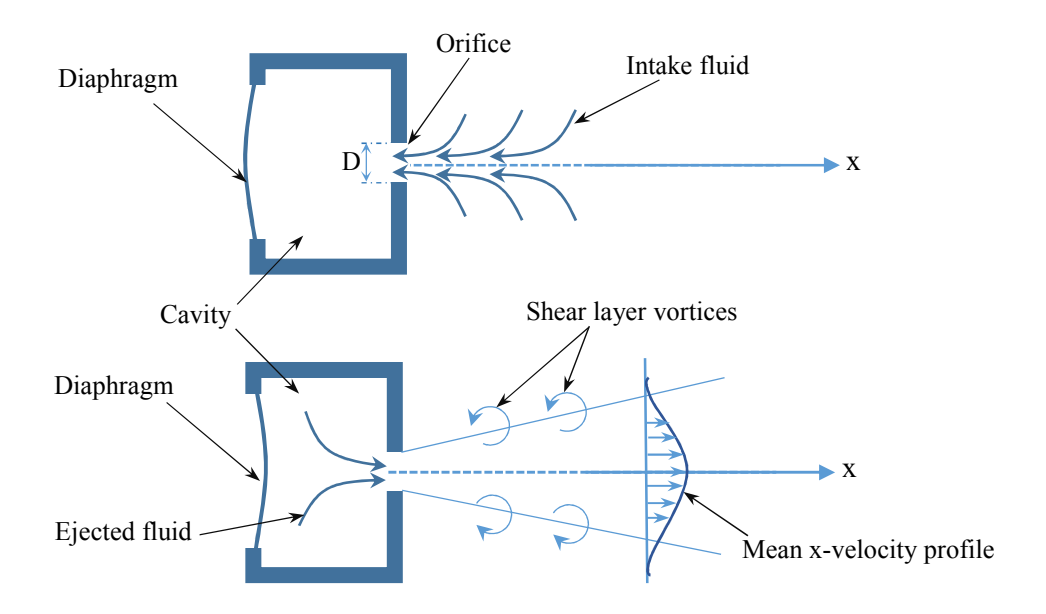


Figure 1.2 Schematic of a synthetic jet during the suction (top) and the ejection (bottom) phase.

1.1.3. Heat Transfer from Vortex-Wall Interaction Arising in Jets or in Isolation

The main flow features are well documented in the literature when a single vortex ring, or a pair of counter-rotating rectilinear vortices, interacts with a flat wall in an isothermal flow field (e.g. see Doligalski and Walker [11], Fabris et al. [12], Orlandi and Verzicco [13] and Gendrich et al. [14]). The vortex ring (primary vortex) moves towards the wall via the "self-induced" velocity while being stretched parallel to the wall, increasing the ring's diameter. As the primary vortex (PV) nears the wall, the opposite-sign boundary layer vorticity beneath the vortex intensifies. A consequent inviscid (primary vortex's pressure signature)/viscous (boundary layer) interaction leads to unsteady separation of the boundary layer. Subsequently, a secondary vortex (SV) ring forms from the erupting shear layer, leading to reversing of the initial primary vortex motion; an effect known as "vortex rebound". Tertiary and higher-order vortex rings are also produced if the primary vortex retains sufficient energy while hovering near the wall in the rebound process.

One of the very few studies considering vortex-wall interaction in the presence of wall heat transfer is Martin and Zenit [15]. These authors numerically studied a pair of *two-dimensional* counter-rotating line vortices interacting with a flat constant-temperature heated wall. They found that the spatial *mean* Nusselt number (*Nu*) over the heated wall segment reached its maximum when the vortices "arrived at the wall", followed by a decrease due to boundary layer separation and formation of the secondary vortex. The correlation between the Nusselt number and the vortical structures was made based on simultaneous observations of the instantaneous vorticity and temperature fields, together with the temporal evolution of the mean Nusselt number. No effort was made to quantify the vortex properties and correlate them with the Nusselt number. Moreover, the characteristics of the surface distribution of the Nusselt number and their connections with the vortical structures were not examined.

Reulet *et al.* [16] conducted an experimental study of a two-dimensional vortex interacting with a laminar boundary layer on a flat plate placed downstream of the vortex generator. They found the unsteady behavior of the boundary layer and the convective heat transfer coefficient to be strongly coupled with the dynamic evolution of the vortex. Specifically, they observed modulation of the boundary layer thickness in the form of thinning followed by thickening as the vortex advected past the location of measurement of the unsteady heat transfer coefficient. The thinning and the thickening of the boundary layer was accompanied by an increase and a decrease in Nusselt number respectively.

The effect of convective heat transfer on unsteady boundary layer separation resulting from vortex-wall interaction was studied by Cassel [17]. His results showed that there is a strong coupling between fluid motion induced by the vortex and the heat transfer within the boundary layer. Specifically, he showed that the unsteady separation of the boundary layer causes a high

temperature gradient in the temperature field and enhances the mixing between the fluid near the wall, in the thermal boundary layer region, and the outer flow.

Chung and Lou [18], in their study of the unsteady heat transfer of an impinging jet, relate the strong fluctuation in the instantaneous Nusselt number to the unsteadiness of the flow field. They propose that "unsteady separation induces a secondary maximum and a local minimum of the instantaneous heat transfer along the impinging wall". The unsteady separation causes thickening in the thermal boundary layer and decreases the heat transfer rate, while the formation of the secondary vortex was reasoned to cause reduction of the thermal boundary layer by engulfing the outer cold fluid around the secondary vortex.

Hadžiabdić and Hanjalić [19] performed large-eddy simulations of a round normally impinging jet for an orifice-to-plate distance of two jet diameters in order to study the vortical structures and turbulence, and their correlation with the local heat transfer coefficient. They concluded that the dip (local minimum) between the primary and secondary peaks in the radial distribution of the Nusselt number is a consequence of local periodic separation of the boundary layer and thickening of the thermal boundary layer. Specifically, the recirculating fluid trapped within the separation zone was heated, causing a reduction in the fluid's heat removal capacity.

Pavlova and Amitay [20] conducted an experiment using an impinging synthetic jet to cool a heated surface. They found the synthetic jet to be three times more effective in cooling the surface than a continuous jet at the same Reynolds number. Also, the authors used different operating frequencies for the synthetic jet, and they found the heat removal from the surface to be better at high frequencies, for a small jet-to-plate distance, while low frequencies provided more effective cooling for large jet-to-plate spacing. The cooling enhancement for small spacing was attributed

to the promotion of near-wall accumulation and breakdown of vortices by high-frequency forcing before the vortices reach the plate. At large jet-to-plate separation, the low frequency excitation resulted in individual vortices impinging separately on the heated surface. The former scenario resulted in approximately 20-25% higher maximum Nusselt number.

Another interesting study of cooling via an impinging synthetic jet was reported by Greco et al. [21]. These authors found differences in the quantitative and the qualitative Nusselt number distribution on the impingement plate, depending on the stroke length of the synthetic jet. These differences were attributed to the change in the vortical structures of the jet and their interaction with the wall as the stroke length was varied. The connection between the stroke length and the flow features was identified in an earlier study by Greco et al. [9]. At low stroke length, the jet produced periodic vortex rings that interacted with the wall. At large stroke length, each ejection of a primary vortex from the jet's orifice was followed by a trailing jet surrounded by a number of vortices, forming from Kelvin-Helmholtz instability. The trailing jet possessed a relatively long potential core and the overall heat transfer characteristics, in this case, were very similar to a continuous free jet flow. In contrast, for a short stroke length, the potential core was shorter and the characteristic inner (primary) peak in the Nusselt number at small jet-to-plate spacing disappeared altogether for sufficiently short stroke length. In this case, the heat transfer was affected by individual interactions of the periodic vortex rings with the wall.

More recently, Hubble *et al.* [22] conducted simultaneous particle image velocimetry and unsteady-heat-transfer measurements when an axisymmetric vortex ring impinges on a flat wall. The resulting detailed data set demonstrated substantial enhancement in the convective heat transfer coefficient, relative to natural convection, beneath the vortex ring. The enhancement occurred at a radial location that was offset from the core center of the vortex, on the side where a

downwash toward the wall is "induced" by the ring. On the upwash side of the induced flow, no heat transfer enhancement was found. This asymmetric influence of the vortex on the wall heat transfer was explained through a "surface renewal model", where particles on the downwash side exhibit short residence time in the thermal boundary layer (TBL), making them relatively cool when they reach the wall. In contrast, particles on the upwash side are assumed to pass beneath the vortex first, lengthening their residence time in the TBL, and hence exhibit more heating before reaching the wall. The hypothesis is based on the behavior of fluid particles within the thermal boundary layer, which the authors do not resolve in their work.

1.2. Motivation and Scope

The collective outcome of the above studies leads to two main conclusions regarding the influence of vortex-wall interaction on the wall heat flux:

- 1. The interaction leads to enhancement in the heat transfer rate (relative to pure conduction or natural convection) on the "downwash side" of the vortex, where the boundary layer becomes thin;
- 2. An accompanying reduction in the heat transfer rate takes place on the "upwash side", where the boundary layer becomes thick and separates.

Though valuable, these findings do not provide a detailed understanding of the vortex-wall interaction physics leading to the observed change in the heat transfer character. These connections between the vortices and the heat transfer are made based on phenomenological, qualitative, description rather than through quantifying the vortex properties and correlating them with the wall heat flux and the thermal boundary layer behavior. This limitation is presumably in part due to the need to have access to spatio-temporal information of the velocity and the temperature fields

with sufficient resolution to resolve the hydrodynamic and thermal boundary layers, along with the various flow features. With the exception of the work of Martin and Zenit [15], the subset of the above studies concerned with isolated vortex-wall interaction, are experimental and do not resolve the boundary layer or measure the temperature field. On the other hand, although the study of Martin and Zenit [15] is computational, the authors only report on gross characterization of the concurrent evolution of the vortex and the average *Nu* on the wall.

Given the above, the present study is planned to take advantage of CFD's ability to provide access to the time- and the space-resolved velocity and temperature fields. The computation is done using the commercial code Ansys-Fluent to solve problems involving a single and two axisymmetric vortex rings interacting with a heated constant-temperature flat wall. Problems utilizing a single vortex are studied for two reasons:

- 1. To quantify the time evolution of the vortex properties (core center location and circulation) and correlate these properties with the characteristics of the time-dependent, radial distribution of *Nu*;
- 2. To study the details of the vortex-wall interaction and how they affect the hydrodynamic and thermal development of fluid particles within the boundary layer. This study is not only aimed at understanding the interaction physics leading to *Nu* augmentation/reduction but also at directly assessing the validity of the recent "surface renewal model" hypotheses of Hubble *et al.* [22].

On the other hand, computations involving two vortex rings are motivated by gaining basic understanding of the effect of vortex pairing on heat transfer in impinging jets. A significant parameter in impinging jets is the distance H between the jet exit and the impingement plate relative to the jet diameter D. This distance can fundamentally alter the details of the vortex-wall

interaction. At small H/D, the jet vortices interact with the wall after they first form via the initial Kelvin-Helmholtz instability of the jet's shear layer. As H/D increases, the jet vortices have room to pair before reaching the wall, but this pairing could happen while the vortices travel past, and interact with the wall; or, if H/D is sufficiently large, before reaching the wall. In the former scenario, vortex-vortex interaction takes place simultaneously with vortex-wall interaction, which could have a significant influence on wall effects. An example of such effects (details are shown in Figure 1.3) is found in the Ph.D. study of Al-Aweni [23]. Al-Aweni found that the pairing of two vortex rings as they travel past the wall in the wall-jet region of an impinging jet produced very strong spikes of negative wall pressure of magnitude of the order of the dynamic pressure of the jet.

Though surface pressure is not necessarily linked with surface heat transfer, Al-Aweni's finding raises questions concerning the possibility of other significant surface effects of near-wall vortex pairing. Of specific importance to the present work is what influence does such pairing have on the heat transfer from the impingement surface? And, how does the interaction of pairing vortices with a flat wall differ from that of a single vortex, produced before or after pairing, from the perspectives of both the flow and the heat-transfer details?

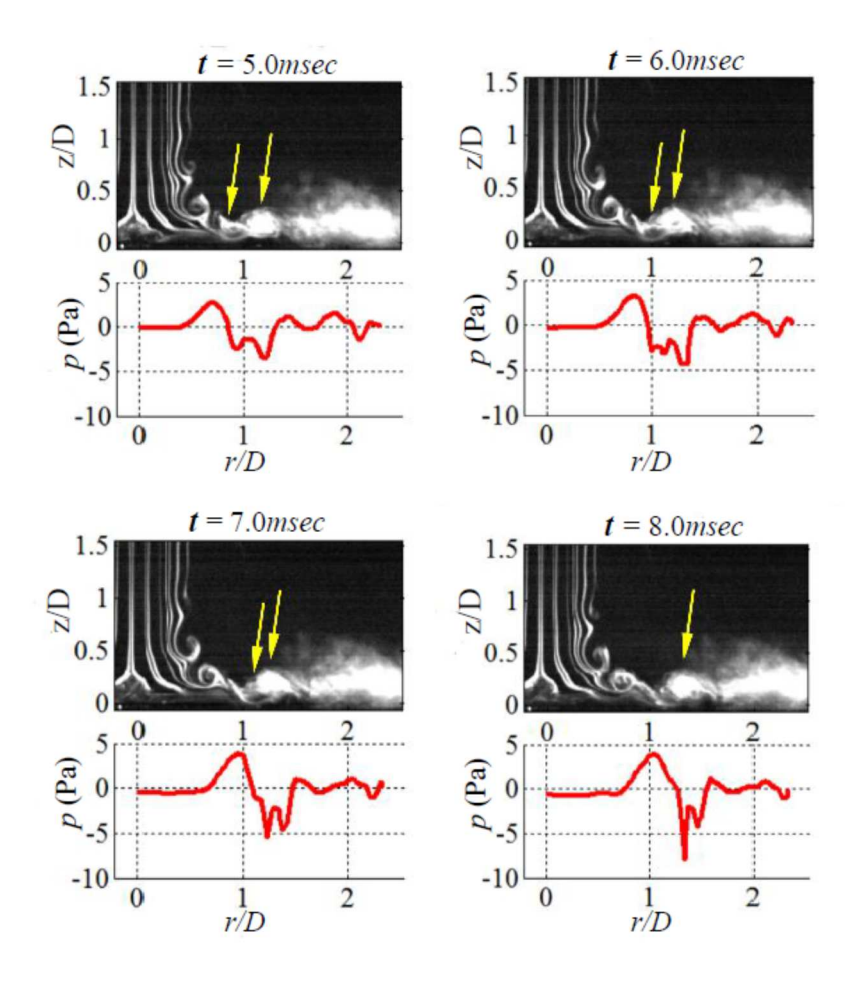


Figure 1.3 Time-resolved flow visualization and concurrent radial wall-pressure distribution of an axisymmetric impinging jet at four time instants, as indicated on top of the images. The impingement wall is located at z/D = 2, and the jet centerline at r/D = 0. Yellow arrows track the pairing of two vortices. Seen in the figure is the development of a strong negative surface-pressure spike in the wall-jet region (r/D > 1) from an initially broad negative peak of approximately -2 Pa at $r/D \approx 0.9$ and time t = 5 ms (top left plot), to a focused negative peak of -7 to -8 Pa at $r/D \approx 1.3$ and time t = 8 ms (bottom right plot). The jet exit velocity is 4.3 m/s and the jet Reynolds number based on diameter and exit velocity is $Re_D = 7,334$. Based on Al-Aweni [23].

The present thesis is also intended to inform concurrent impinging-jet control efforts in the Flow Physics and Control Laboratory (FPaCL) at Michigan State University. One of the control strategies in these efforts, which are aimed at the enhancement of heat transfer in impinging jets, targets acceleration/deceleration of vortex pairing such that the phase of vortex-vortex-wall interaction is most favorable from heat transfer perspective. Therefore, the present work is instrumental in providing insight for informed development of the aforementioned control strategy.

The present computations are only concerned with axisymmetric interactions of vortex rings with a flat wall. This focus might seem disconnected from the reality of jet vortices which evolve from the initially axisymmetric form to complex 3D structures by the end of the potential core in naturally developing free and impinging jets (e.g. see Yule [24], Kataoka et al. [25] and Violato et al. [26]). However, as mentioned above, this research is specifically motivated by developing jet control strategies to enhance the heat transfer rate resulting from vortex-wall interactions. Under the effect of control via axisymmetric forcing, it is well known that the jet vortical structures can remain coherent and axisymmetric over a larger domain of development than possible under natural, unforced conditions. Examples may be found in the works of Schram [27] at a jet Reynolds number of up to 93,000, for free jets, and Didden and Ho [28] at a jet Reynolds number of 19,000, for impinging jets. Moreover, even for natural impinging jets, we expect axisymmetric interactions to be relevant at small H/D values that do not extend to the vicinity of the potential core. This is demonstrated in the flow visualizations of Popiel and Trass [6] for H/D = 1.2 and 2 at Reynolds numbers up to 20,000. Finally, from the perspective of understanding of fundamental phenomena, developing physical insight into the influence of the

interactions of axisymmetric vortices on thermal transport with a flat wall is an important first step prior to tackling the more complex problem involving three-dimensional, distorted vortex rings.

1.3. Objectives

The specific objectives of this research are as follows:

- 1. To set up the CFD simulation of the vortex-ring-wall interaction problem in Ansys-Fluent and validate the approach using the experimental data of Gendrich *et al.* [14] in the absence of heat transfer. This step employs experimental data to initialize the computation and is intended to provide confidence in the overall computational approach for the velocity field. No equivalent experimental data were accessible for validation of the thermal aspects of the computations.
- 2. To compare the effect of pairing of two vortices as they interact with the wall to that of a single vortex on the unsteady wall heat transfer. Two "single-vortex" cases are considered: one where the vortex is identical to one of the vortices in the "pairing problem", and the other with the vortex having twice the circulation and the core radius of one of the pairing vortices. These two single-vortex cases represent situations where a vortex approaches the wall before and after pairing. These simulations are initialized using a model vortex having Gaussian vorticity distribution within the core. The analysis of this part of the investigation will include quantifying the vortex characteristics and correlating their time-dependent behavior to the Nusselt number, the wall shear stress, and the thermal boundary layer.
- 3. To utilize the CFD data sets to understand the fundamental vortex-wall interaction physics through boundary-layer-resolved analysis. This study, which is undertaken in an attempt to understand the mechanisms of Nusselt number augmentation/reduction, includes

tracking of fluid particles within the thermal and hydrodynamic boundary layer in order to evaluate the surface renewal hypothesis of Hubble *et al.* [22].

CHAPTER 2

COMPUTATIONAL DETAILS AND VALIDATION

Three different sets of computations are conducted in the present work. The first of these (referred to as set A) involves velocity field calculations only and is used for validation of the computational approach by comparing against experimental data. The second (set B) is employed for the investigation of the heat transfer due to the interaction of one or two vortex rings with a flat constant-temperature heated wall. Two different single-vortex cases are considered. The first (Case I) employs a vortex ring that is identical to one of the rings in the two-vortex simulation (Case II). The second, utilizes a vortex ring with twice the circulation and core-radius size (Case III). The three simulations in set B represent three scenarios where vortex-wall interaction takes place before (Case I), during (Case II) and after (Case III) vortex pairing. The third (set C) is an additional set of calculations employed for getting more information of the detailed physics of the vortex interaction with the heated wall. Two cases are conducted in this set: the first case is in the absence of thermal diffusivity ($\alpha = 0$), and the second one employing a slip-wall boundary condition (by setting the wall shear stress $\tau = 0$). For simplicity, these cases will be referred to as (Case $\alpha = 0$), and (Case $\tau = 0$). The computational details of each set are given below.

2.1. Validation of the Computational Approach: Set-A Computations

No experimental data sets were found for the case of an isolated vortex-ring pair interacting with a wall. In contrast, there are a few experimental studies of the velocity field of an isolated vortex-ring interacting with a flat wall (e.g. Fabris *et al.* [12] and Gendrich *et al.* [14]). However, none of these works includes heating or cooling of the impingement wall. Therefore, validation of the current CFD approach is only done for velocity field calculations. For this

purpose, the whole-field data of Gendrich *et al.* [14] were readily accessible to the author. This data set includes measurements of the radial and wall-normal components of the velocity of an axisymmetric vortex ring impinging on a flat wall. The initial circulation Γ_o of the vortex ring results in a Reynolds number $Re_{\Gamma} = \Gamma_o/v = 4500$; where ν is the kinematic viscosity. Significantly, at the experiment's Reynolds number and initial vortex-ring parameters, the entire flow remains axisymmetric and non-turbulent (i.e. without the development of 3D instability and small-scale turbulence) for the entire duration of the measurements; which extends well beyond the duration of all computations conducted here. Thus, this case is appropriate for comparison against the unsteady, laminar, axisymmetric calculation framework used in the present investigation.

The flow features and sequence of events of an isolated vortex ring impinging normally on a flat wall is well understood from literature. The flow evolution (which may be seen via the vorticity field snapshots in Figure 3.4 for computation set *B*) starts with the ring propelling itself towards the wall via the "self-induced" velocity, while stretching radially outwards, because of the no-penetration wall boundary condition (i.e. the "induced" velocity influence of the image vortex). In the process, a radially-outward flow near the wall is established, creating a boundary layer with vorticity opposite in sign to that of the primary vortex. When the initial (primary) vortex (also referred to as PV hereafter) gets sufficiently close to the wall, its surface pressure imprint causes the boundary layer (BL) to separate, and the resulting shear layer rolls up into a secondary vortex (SV) of opposite vorticity sign to the PV. Subsequent mutual interaction of the PV and SV arrests the outward radial movement of the PV, while the SV orbits around the PV, making its way from a radially outboard position relative to the PV towards the axis of symmetry. The SV eventually ejects away from the wall, if sufficiently strong, and the PV produces tertiary and "higher order" vortices, in a process similar to that of generating the SV; if the PV retains sufficient energy.

Ansys Fluent 17.1 is employed for the present computations by using water, with temperature-dependent properties, as the fluid. The computational domain is half of axisymmetric box with three sides walls, extending over a domain of 0.06 m by 0.06 m in the radial (r) and wallnormal (z) directions (the domain is the same as illustrated in Figure 2.5 for computational set B). The domain size was set to be sufficiently large so that the side and the top wall presence does not influence the vortex evolution (see Table 2.1). A uniform grid with the same resolution in the radial and wall-normal directions, $\Delta r = \Delta z = 0.00012 \, m$, is employed. Grid-independence studies (Figure 2.1a) show that this grid size (corresponding to 500×500 grid points) is sufficient to resolve the vorticity (ω) evolution of the primary vortex. An implicit second-order scheme is selected for the time advancement with a time step size of $\Delta t = 0.001 \, s$. Figure 2.1b demonstrates that this time step size is appropriate. The no-slip boundary condition is used on three of the domain boundaries, with the condition of axisymmetry imposed on the fourth boundary. Experimental data of the velocity field are used to initialize the calculation. Because the computational grid is more than eight times smaller than the experimental grid (1 mm), linear interpolation is used to map the initial velocity field from the experiments onto the CFD grid.

A pressure-based solver is used for the simulation, employing pressure-velocity coupling (PISO scheme) with zero skewness correction and one neighboring correction. The spatial discretization is least squares cell-based for gradients, standard for pressure, second-order upwind for density and third-order MUSCL for both momentum and energy. A second order implicit scheme is used for the transient formulation. The solution control employed the default underrelaxation factors in Ansys Fluent 17.1, and the solution is monitored by setting the residual to a very small value to obtain 200 iterations per time step, ensuring the convergence of the solution

for all quantities. Solution convergence with a number of iterations is checked by conducting several simulations with different number of iterations.

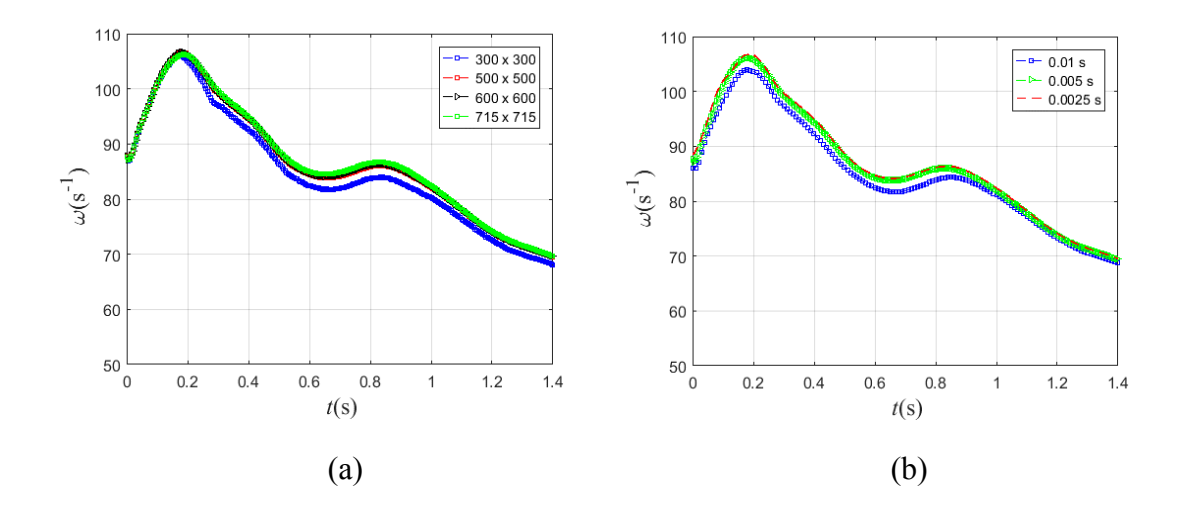


Figure 2.1 Effect of the grid resolution (a) and the computational time step (b) on the temporal evolution of the peak vorticity within the core of the primary vortex. Computations are done using experimental data from Gendrich $et\ al.$ [14] as initial condition. The legend in the left plot shows the number of grid elements in the r and z directions, while the legend in the right plot provides the computational time step size.

The vorticity (ω) in Equation 2.1 is used to calculate the out of plane vorticity (where u_r and u_z are the radial and wall-normal components of velocity). The derivatives in Equation 2.1 are calculated using the central second-order-accurate finite-difference method for the entire domain, while forward and backward second-order-accurate finite differences are used for the boundaries. Equations 2.2 through 2.4 show the finite-difference form for the central, forward and backward difference (e.g. see Fornberg [29]), respectively, for a generic function $\zeta(x)$:

$$\omega = \frac{\partial u_z}{\partial r} - \frac{\partial u_r}{\partial z} \tag{2.1}$$

$$\frac{\partial \zeta(x_i)}{\partial x} = \frac{\zeta(x_{i+1}) - \zeta(x_{i-1})}{2\Delta x} \tag{2.2}$$

$$\frac{\partial \zeta(x_i)}{\partial x} = \frac{-3\zeta(x_i) + 4\zeta(x_{i+1}) - \zeta(x_{i+2})}{2\Delta x}$$
 (2.3)

$$\frac{\partial \zeta(x_i)}{\partial x} = \frac{3\zeta(x_i) - 4\zeta(x_{i+1}) + \zeta(x_{i+2})}{2\Delta x}$$
 (2.4)

Considering some of the vortex characteristics, Figure 2.2 shows the temporal evolution of the maximum and the minimum azimuthal vorticity value within the core of the primary and the secondary vortex respectively. The spatial locations of the vorticity peaks correspond to the vortex core "centers", the locus of which at different time instants is used to identify the motion trajectory of the vortices (Figure 2.3). In Figure 2.2, the initial PV vorticity increases due to the outward motion of the ring and associated vortex stretching. As mentioned earlier, subsequent to the formation of SV, the outward radial motion of the PV ceases, which causes the vortex stretching to stop, and the PV vorticity decays while getting subtly modulated due to jitter in the radial location of the PV. In contrast, the vorticity magnitude of the SV generally decreases monotonically with time.

The qualitative features of the vorticity evolution described above are in excellent agreement between the experiment and the computation. Quantitatively, the PV vorticity is captured very well in the computation; though some small differences are seen in the vorticity modulation during the decay phase. On the other hand, initially, there is a sizable difference between the experiment and the computation in capturing the vorticity of the SV. With the progress

of time, this difference disappears, and the two data sets provide the same results. The cause for the initial discrepancy is unknown. The computational vorticity results are computed using velocity data extracted at locations matching those in the experiment (i.e. on a 1-mm grid, which is coarser than the CFD grid). Therefore, the discrepancy is not attributed to the influence of the lower spatial resolution of the experiments on calculating vorticity.

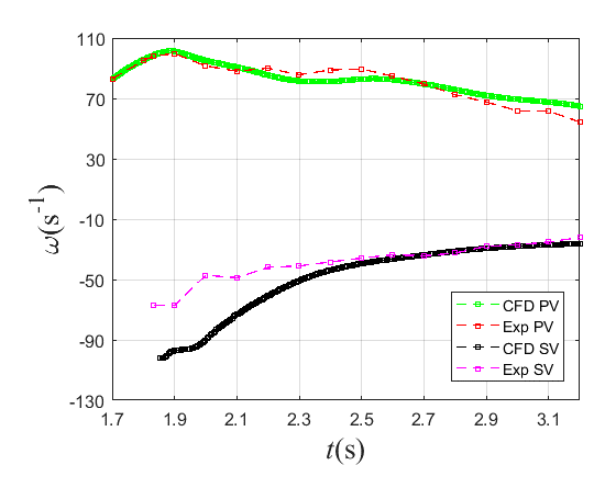


Figure 2.2 Comparison between the experimental and the computational results of the temporal evolution of the maximum and minimum vorticity value in the core of the primary (PV) and the secondary (SV) vortices respectively. The origin of the time axis is based on the experiments of Gendrich *et al.* [14] and it corresponds to the time of the velocity field data employed to initialize the computation.

Figure 2.3 shows that the CFD reproduces the experimentally observed trajectories of the primary and secondary vortices reasonably well. Again, the qualitative agreement is very good, while some quantitative differences are present. These differences relate primarily to the fine details of the modulation of the r and z locus of the PV core center, and the SV trajectory as it ejects away from the wall towards the end of the computation.

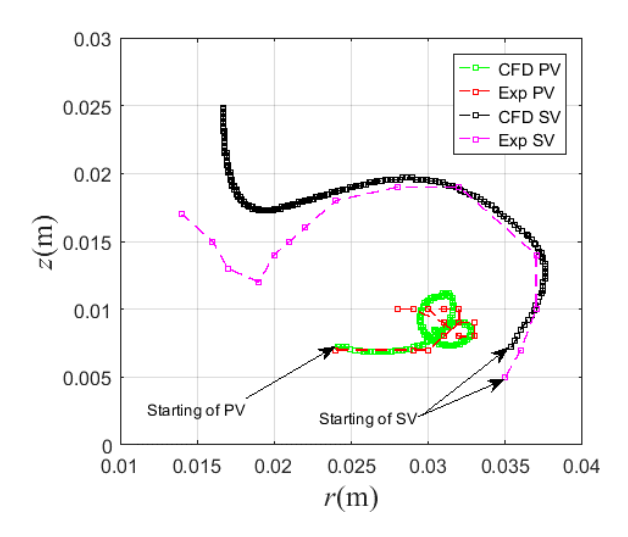


Figure 2.3 Comparison between the experimental and the computational results of the trajectories of the primary and the secondary vortices (PV and SV respectively).

Another quantity that is considered in comparing the experimental and the computational results is the maximum boundary layer vorticity at a given time instant (which is proportional to the negative of the maximum wall shear stress). The maximum BL vorticity is tracked in time and compared to the corresponding experimental results in Figure 2.4 The figure depicts a generally good agreement in the quantitative and qualitative features of the BL vorticity evolution. The main difference between the two results is a rather small time delay in the evolution of the boundary layer in the CFD case. Also noteworthy is that given the small discrepancy between the two cases, the discrepancy in the early evolution of the SV vorticity (Figure 2.2) is apparently not caused by a difference in boundary layer evolution.

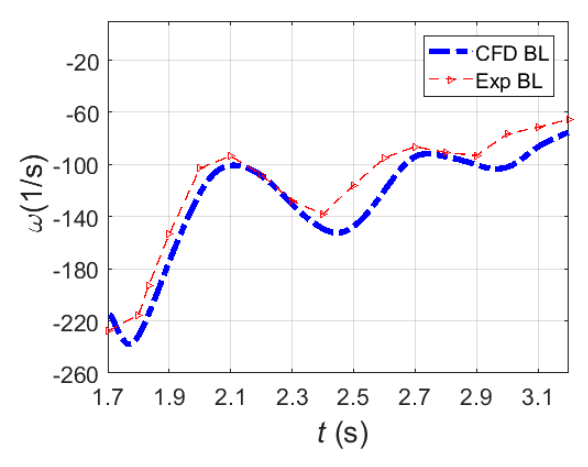


Figure 2.4 Comparison between the experimental and the computational results of the temporal evolution of the maximum vorticity value of the boundary layer (BL). The origin of the time axis is based on the experiments of Gendrich *et al.*[14] and it corresponds to the time of the velocity field data employed to initialize the computation.

2.2. Main Computations: Set-B Computations

The second (main) computation set is employed for the investigation of the heat transfer due to the interaction of one or two vortex rings with a flat constant-temperature heated wall, using air as the working fluid. Three computational cases are conducted: the first utilizing an initial condition of a single vortex ring (Case I). The second, using two vortex rings (Case II) with the initial circulation and core radius of each vortex equal to those of the vortex in the first case. And the third (Case III), is for a single vortex with twice the circulation and the core radius of the first case. The three simulations in this set represent three scenarios where vortex-wall interaction takes place before (Case I), during (Case II) and after (Case III) vortex pairing. Because no experimental data could be found in the literature concerning the interaction of two isolated vortex rings with a wall, it was not possible to conduct the main simulation for this work employing an initial

condition based on experimental data. Instead, the initial condition is defined mathematically using Gaussian vorticity distribution in the vortex core; specifically:

$$\omega(r, z, t = 0) = \omega_o e^{-\frac{(r - R_o)^2 + (z - Z_o)^2}{a_o^2}}$$
(2.5)

$$\Gamma_o = \pi \ a_o^2 \ \omega_o \tag{2.6}$$

where ω_o , R_o and Z_o are the initial vorticity and radial and wall-normal coordinates of the vortex core center respectively, a_o is the initial vortex core radius and Γ_o is the initial vortex circulation. The corresponding radial (u_r) and wall-normal (u_z) velocity components are given by:

$$u_r(r,z,t=0) = -\frac{\Gamma_o}{2\pi} \left[1 - e^{-\frac{(r-R_o)^2 + (z-Z_o)^2}{a_o^2}} \right] \frac{(z-Z_o)}{(r-R_o)^2 + (z-Z_o)^2}$$
(2.7)

$$u_z(r,z,t=0) = \frac{\Gamma_o}{2\pi} \left[1 - e^{-\frac{(r-R_o)^2 + (z-Z_o)^2}{\alpha_o^2}} \right] \frac{(r-R_o)}{(r-R_o)^2 + (z-Z_o)^2}$$
 (2.8)

Equations 2.7 and 2.8 are derived from a 2D vortex with Gaussian vorticity distribution in the core. While the problem examined is axisymmetric, the associated velocity is expected to approach that of a 2D vortex in the limit of $a_0/R_0 \ll 1$, which is satisfied for Case I. For the other cases, the largest a_o/R_o is 0.32, which may lead to some errors in the initial condition satisfying the Navier-Stokes equations. However, any initial errors should die out quickly in the iterative

numerical solution, so that by the time the averaged Nusselt number starts to be affected by the primary vortex (Figure 3.15a), the solution adheres to the Navier-Stokes equations. This is also confirmed by Shrikhande [30] who found that the Gaussian vortex model given by Equations 2.7 and 2.8 provide reasonable comparison with the experimental data of an axisymmetric vortex ring interacting with a flat wall.

Generally speaking, the initial coordinates R_o and Z_o of the vortex core center, in the single-ring case, and the relative placement of core centers, in the dual-ring case could significantly affect the details of the vortex-wall/vortex-vortex interaction. Though this initial placement may be parameterized and varied systematically, this would require running numerous cases (particularly for the scenario with two vortex rings) and will likely make it difficult to reach useful general conclusions. Thus, to define the initial locations of the vortex rings in a focused, physically meaningful way, use is made of the application motivating this work: impinging jets. Specifically, the initial location of the core centers is selected to match typical locations of vortices in the impinging-jet flow visualization images of Al-Aweni [23].

The top half of Figure 2.5a and 2.5b shows sample flow visualization of the jet flow when the impingement wall is placed at 2D and 3D (D is the jet diameter) respectively away from the jet exit. In the former case, two vortices (labeled "inner" and "outer") are seen near the wall. From time-resolved visualization of these vortices, it is known that they pair as they travel radially outwards parallel to the wall. The r and z coordinates of the core centers of these vortices are approximated from the image in the top of Figure 2.5a and used for defining the initial condition for Case II. For the single-vortex "pre-pairing" case, a vortex with the identical characteristics of the outer vortex is used for the initial condition. Similarly, for the "post-pairing" single-vortex case, where pairing is complete before reaching the wall, the initial vortex core center location is

found using the flow visualization in Figure 2.5b. This is demonstrated in the latter figure for a vortex that is visually larger than the vortices in Figure 2.5a due to the completion of vortex pairing ahead of the impingement wall when the plate is farther away from the jet.

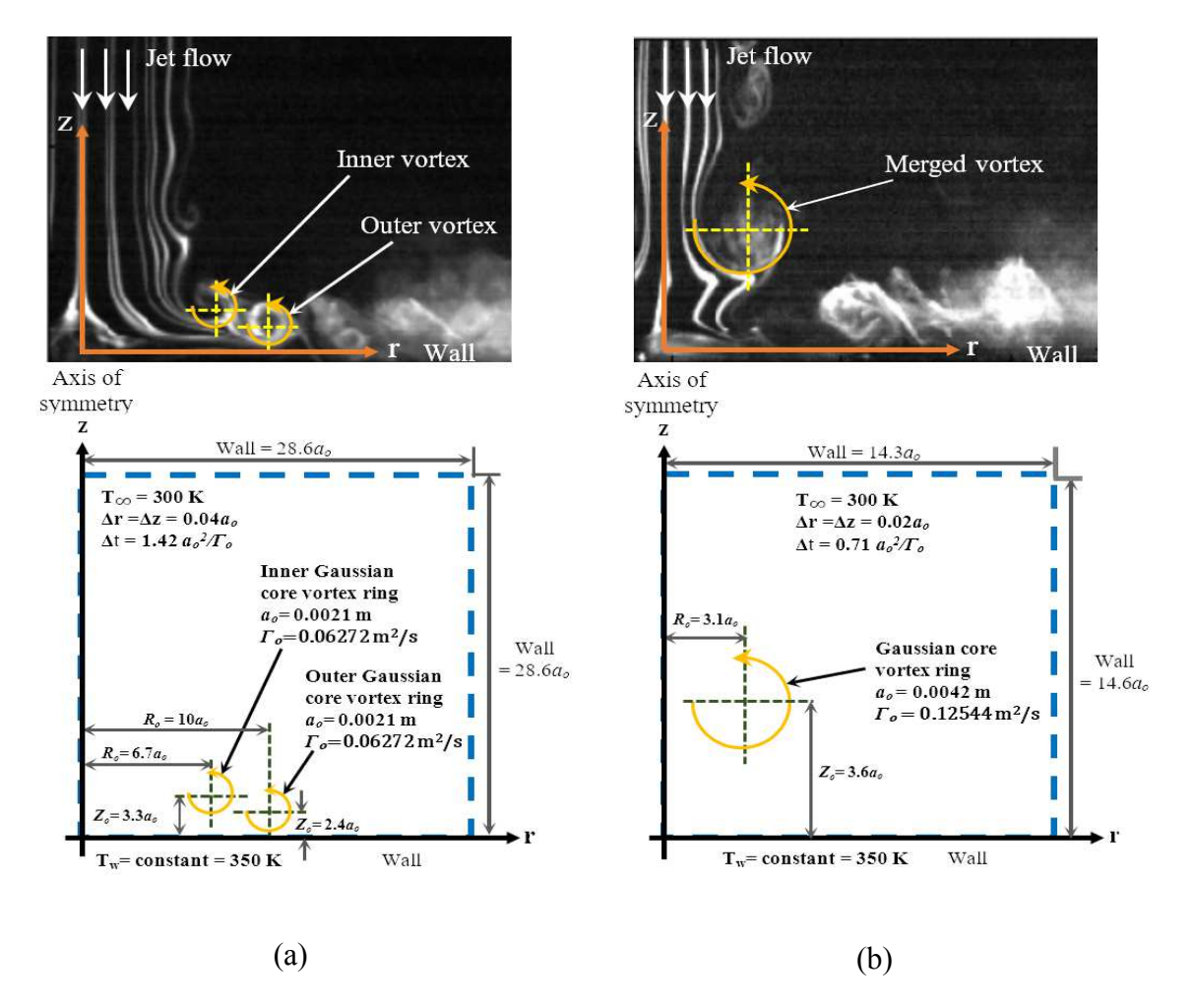


Figure 2.5 Sketch illustrating the computational domain and boundary and initial conditions for Cases II and III of computational set B: a) a pair of Gaussian-core vortices (Case II); b) a single Gaussian-core vortex with twice the initial circulation and core radius (Case III). The problem setup of Case I is the same as Case II with the only difference being the removal of the inner vortex. The computational domain spans only one single azimuthal plane due to flow axisymmetry. The flow visualization images on top are taken from Al-Aweni [23] and are used to determine R_o and Z_o shown on the corresponding sketches on bottom.

For Cases I and II, the initial outer vortex core radius, a_o is set to be an order of magnitude smaller than the vortex ring radius to minimize the influence of this parameter on the results (i.e. in the limit of a thin vortex ring; $a_o/R_o \rightarrow 0$). Specifically, a_o/R_o is set to 0.1 in Case I. In Case III, a_o for the inner vortex is kept the same as for the outer, and in Case III, the post-pairing single-vortex case, the initial core radius is chosen to be twice that used in the other two cases, as previously mentioned.

The computational domain is illustrated in the bottom part of Figure 2.5. Because of the flow axisymmetry, the computation is conducted in a single azimuthal plane of size $0.06 \text{ m} \times 0.06 \text{ m}$ (28.6 a_o in Case I and II, and $14.3a_o$ in Case III). The spatial and temporal resolutions of the simulations are $\Delta r = \Delta z = 8.39 \times 10^{-5} \text{ m}$ ($\Delta r = \Delta z \approx 0.04a_o$ in Case I and II, and $0.02a_o$ in Case III) and $\Delta t = 0.0001 \, s$ ($\Delta t = \frac{1.42a_o^2}{\Gamma_o}$ in Case I and II, and $\Delta t = \frac{0.71a_o^2}{\Gamma_o}$ in Case III) respectively.

The grid and the temporal resolutions, and the domain size are selected by conducting domain, grid, and time-step independence studies (see Appendix A). Upon convergence, the maximum error in different flow and thermal quantities is summarized in the Table 2.1.

Table 2.1 Maximum percentage errors for the results in Appendix A

	Maximum percentage error %			
	Spatial resolution	Temporal resolution	Domain size	Number of iterations
Primary vortex peak vorticity	1.2	0.57	0.25	1.5×10 ⁻⁰⁸
Secondary vortex peak vorticity	1	3.4	0.36	2×10 ⁻⁰⁸
Boundary layer vorticity	1.7	1.5	0.8	4×10 ⁻⁰⁸
Maximum Nusselt number	0.6	0.4	0.4	0

The initial vortex circulation is found by setting the vortex Reynolds number $Re_{\Gamma} = \Gamma_o/\nu =$ 4,000 for the inner and outer vortices. For the post-pairing case (Case III), the circulation is doubled, resulting in $Re_{\Gamma} = 8000$. The gravity term in the governing equations is turned off to exclude the influence of buoyancy and natural heat convection. This enables focus on heat transfer mechanisms that are only related to the vortex-wall interaction.

The temperature of all boundaries is set to 300 K, except for the bottom wall which is kept at a higher temperature of 350 K. In early simulations, a uniform temperature field of 300 K was prescribed everywhere for the initial condition of the fluid. However, the "step" change in temperature near the wall made it difficult to properly resolve the early evolution of the thermal boundary layer. To resolve this issue, an initial thermal boundary layer (TBL) is prescribed based on the semi-infinite-domain unsteady-diffusion solution above an infinite constant-temperature flat wall (Incropera and *et al.* [31]):

$$\frac{T(z,t) - T_w}{T_{\infty} - T_w} = \operatorname{erf}\left(\frac{z}{2\sqrt{\alpha t}}\right)$$
 (2.9)

where T_{∞} and T_{w} are the temperatures of the fluid, outside the thermal boundary layer, and the wall respectively, α is the thermal diffusivity and t is time.

Figure 2.6a shows the wall-normal temperature profile evolution with time using Equation 2.9 in increments of $5\Delta t$ (where Δt is the computational time step). The profile obtained after ten increments (shown with a thick black line) is chosen to initialize the temperature field in order to avoid the initial infinite temperature gradient at the wall associated with a step temperature profile (depicted in the same plot with a thick broken black line). The selected time instant of 0.005s provides a reasonable balance between ensuring that multiple grid points are present within the initial thermal boundary layer (approximately twelve points for the selected time) and that the TBL is small enough such that it is initially unaffected by the vortical flow. The latter condition enables observation of the evolution of the interaction of the vortical flow with the TBL from the beginning. The resulting initial temperature field is depicted in Figure 2.6b, which includes a magnified view of the initial thermal boundary layer.

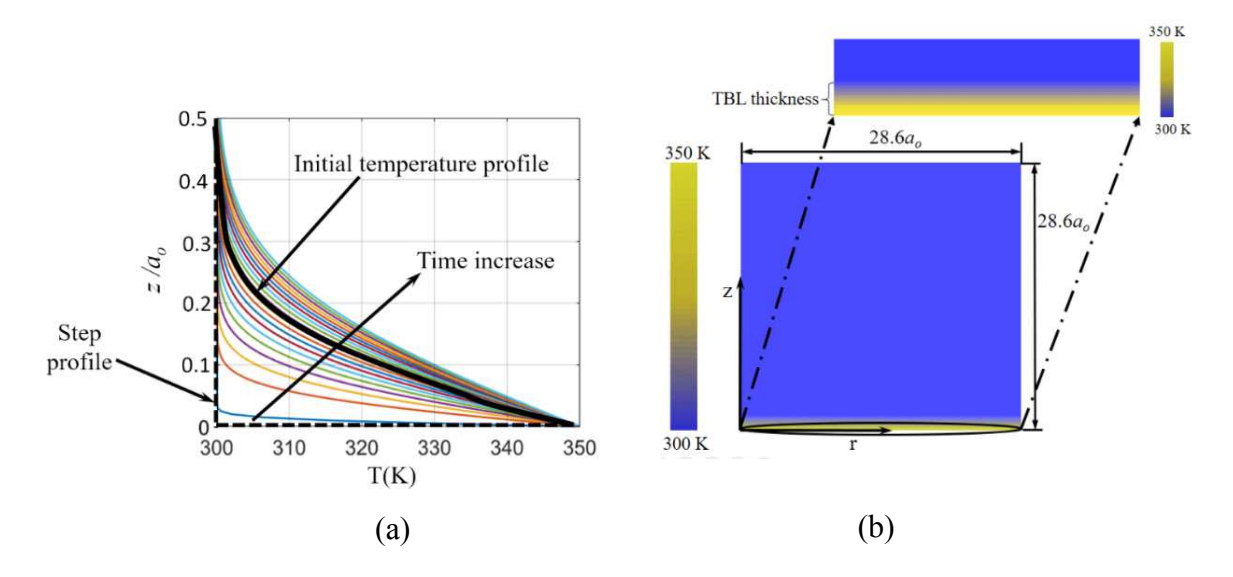


Figure 2.6 a) Temporal evolution of the wall-normal temperature profile obtained from Equation 2.9. The profile evolves monotonically in the direction indicated by the arrow. Different times are represented by different line colors, with the time step between two successive lines equal to $5\Delta t$. The thick solid black line outlines the temperature profile selected to initialize the temperature field; b) The initial temperature field of the computational domain, with a magnification of the TBL.

2.3. Additional Computation: Set-C Computations

Two additional computations are conducted in order to get more information about the detailed physics of the heat transfer enhancement and deterioration during vortex-wall interaction. Both of these cases focus on single-vortex-ring interaction with the wall, and they have the same exact working fluid (air) and parameters as Case I except for one parameter of interest that is altered. The first additional case (Case $\alpha=0$) is conducted by setting the thermal conductivity of the fluid k=0; where $\alpha=\frac{k}{\rho c_p}$ and ρ and c_p are the density and the constant-pressure specific heat, respectively, of the fluid. The initial temperature field is kept the same as in Case I, in spite

of setting the thermal diffusivity to zero. This case enables examination of the vortex interaction with the thermal boundary layer without the thermal diffusivity, aiding in exploring the role of thermal diffusion on the temporal evolution of the radial distribution of the Nusselt number Nu_r . In other words, Case $\alpha = 0$ facilitates observing how the temperature field evolves under pure convective effects resulting from the flow field of vortex-wall interaction.

A computational difficulty was encountered in simulating Case $\alpha = 0$. As will be seen in Chapter 3, the PV is associated with both a downwash towards, and an upwash away from the wall. On the downwash side, the TBL becomes thinner due to the movement of the fluid towards the wall. This results in increasing the temperature gradients in the TBL, which strengthens diffusive effects that oppose the convective thinning of the thermal boundary layer. Thus, thermal diffusion limits the thinning of the boundary layer. When $\alpha = 0$, the opposing mechanism disappears, and the TBL continuously thins on the downwash side, eventually making the computational mesh resolution inadequate to correctly resolve the temperature field and compute the wall temperature gradient (which is necessary for obtaining the Nusselt number). Figure 2.7 demonstrates this problem by showing the corresponding number of the grid points (which are depicted as fractional multiple of the grid spacing of the original CFD calculation) in the minimum thermal boundary layer thickness ($\delta_{th,min}$) at a given time instant for both Case α =0 and Case I. As seen from the figure, the number of grid points reduces to only two grid points within the $\delta_{th,min}$ halfway through the computation. In comparison, the thinnest TBL thickness encountered in Case I contains seven grid points.

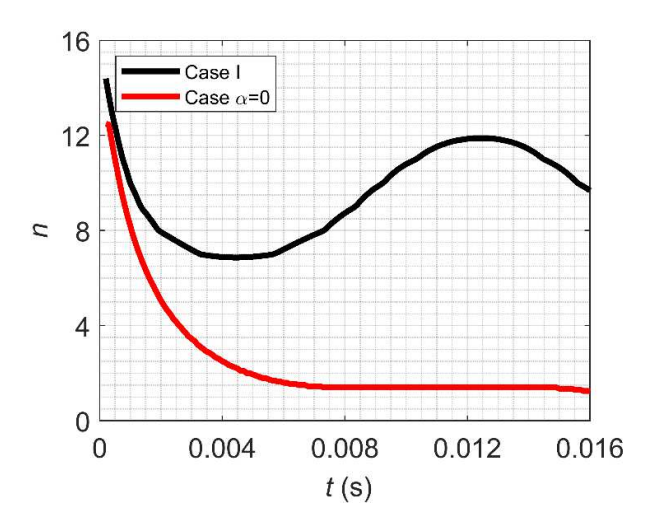


Figure 2.7 Comparison of the number of the grid points (n) within $\delta_{th,min}$ for Case I and Case $\alpha = 0$ versus time. The number of grid points is depicted as fractional multiple of the grid spacing. The actual number of grid points, which is an integer, is the largest integer number below the value shown.

In order to avoid the added cost of computational time when using a finer mesh resolution, an alternative technique is used to compute the temperature field from post-processing of the velocity field. Since the present computation is incompressible, the velocity field calculation is unaffected by the temperature calculation and the issues arising from setting $\alpha = 0$. The post-processing calculation method is based on this point, along with the fact that, when $\alpha = 0$, the thermal energy equation reduces to the material derivative of temperature is equal to zero, i.e. $\frac{DT}{Dt} = 0$. This means a fluid particle's temperature stays the same as the particle moves due to the presence of the vortex-wall interaction flow field.

Based on the above, by treating temperature as a passive scalar, the evolution of the initial temperature field with time is obtained via a Lagrangian description by following the particle trajectories. To obtain the equivalent Eulerian description at any given time, the spatially non-

uniform instantaneous Lagrangian description of the temperature field is interpolated on a uniform Eulerian grid that is much denser than the original computational grid. MATLAB is used for coding a program that implements this approach. In this program, the particles' locations are advanced over one time step Δt using the velocity field from Case I, employing the equations below:

$$r_n = r + u_r \times \Delta t \tag{2.10}$$

$$z_n = z + u_z \times \Delta t \tag{2.11}$$

where r_n and z_n are the new radial and axial positions of the particle respectively.

The starting particle positions at each time step always coincide with the fine-mesh Eulerian grid. At every time instant, the velocity field on this grid is found by interpolating the CFD solution onto the finer grid. The initial temperature field is the same as in Case I but interpolated on the denser grid. This gives an initial Eulerian description of the temperature field T(r,z,t=0). The new positions (r_n,z_n) of the particles after one time step result in a Lagrangian description of the field at time Δt by simply replacing the Eulerian grid coordinates with the particle coordinates; i.e. at $t=\Delta t$, $T=T(r_n,z_n,\Delta t)$. Before evolving the temperature field further to the next instant, $t=2\Delta t$, the second step is to interpolate the temperature field on the non-uniform grid $T(r_n,z_n,\Delta t)$ on the uniform Eulerian grid to advance the Eulerian field in time; i.e. to get $T(r,z,\Delta t)$. This two-step Lagrangian-Eulerian evolution is repeated for every time step, starting with the Eulerian field from the previous time step. The new fine mesh spacing is set to $\Delta z/20$ in the axial direction from the wall to $z\approx 0.005m$. On the other hand, the radial direction interval is set to $\Delta T/4$ from $r\approx 0.01m$ to $r\approx 0.05m$, where $\Delta z=\Delta r$, are the size of the mesh

elements of the CFD calculations. This \times 20 and \times 4 enhancement in spatial resolution of the temperature field in the z and r directions respectively, is focused in the near-wall, near-PV domain. Outside this domain (where no "action" is happening), the grid resolution is maintained the same as in the CFD calculations.

Figure 2.8a and 2.8b show the difference in calculating the maximum Nu_r (which, as will be seen in Chapter 4, occurs where $\delta_{th,min}$ is located) using different orders of accuracy of finite difference in Case I and Case $\alpha = 0$ respectively. The equations of the 1st and 4th order of accuracy of the forward finite difference employed in Nu_r calculation are listed below, while the 2nd order of accuracy was given in Equation (2.3).

$$\frac{\partial \zeta(x)}{\partial x} = \frac{-\zeta(x_i) + \zeta(x_{i+1})}{\Delta x} \tag{2.12}$$

$$\frac{\partial \zeta(x)}{\partial x} = \frac{\left(-\frac{25}{12}\right)\zeta(x_i) + 4\zeta(x_{i+1}) - 3\zeta(x_{i+2}) + \left(\frac{4}{3}\right)\zeta(x_{i+3}) - \left(\frac{1}{4}\right)\zeta(x_{i+4})}{\Delta x}$$
(2.13)

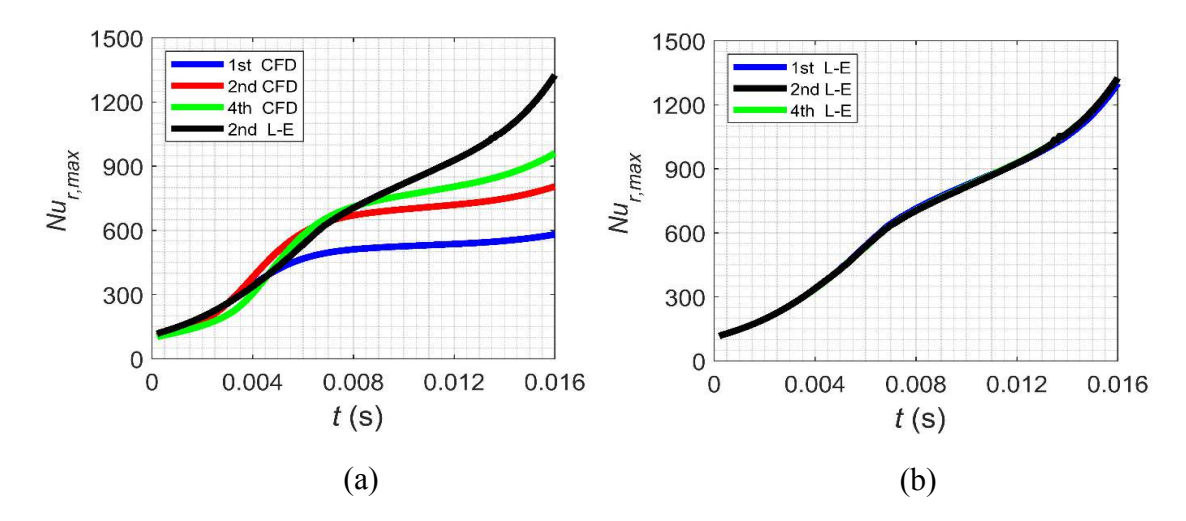


Figure 2.8 The evolution of $Nu_{r,max}$ calculated using different orders of accuracy of the finite difference applied to data from; a) CFD on the old computational mesh; b) Lagrangian-Eulerian (L-E) passive scalar evaluation on the new fine mesh. Plot (a) also contains the second-order finite-difference result from plot (b) for direct comparison.

The results in Figure 2.8 show that, except for a short duration in the early evolution, the calculation of $Nu_{r,max}$ does not converge with increasing finite-difference-scheme order when using the CFD data. This demonstrates the issue of "resolution loss" discussed in connection with Figure 2.7. In contrast, by tracking particle temperatures and interpolating on a dense Eulerian grid, the computation of $Nu_{r,max}$ is convergent even using first-order finite-difference.

The second additional computational case investigated is motivated by a deeper examination of the mechanism of the deterioration of the Nusselt number on the upwash side of the PV (see Chapter 3). Once boundary layer separation occurs, the minimum Nu_r is always found in the vicinity of the separation point (Section 3.4). To better understand the role of separation on this heat transfer deterioration, a study case is considered where separation is eliminated by allowing the flow to slip at the wall. This is achieved by setting the boundary conditions $\tau = 0$ at

the heated wall, while keeping all other initial and boundary conditions the same as Case I (set-*B*).

More details about the $\tau = 0$ and the $\alpha = 0$ cases will be discussed in Chapter 4.

CHAPTER 3

VORTEX-WALL INTERACTION AND HEAT TRANSFER

3.1. General Considerations

3.1.1. Normalization

With the exception of the Nusselt number (see Equation 3.10 below), length scales are normalized by the initial core radius of the primary vortex a_o , while time scales are normalized using the primary vortex's "turn over time" a_o^2/Γ_o , where Γ_o is the initial circulation. With these choices, the relevant velocity scale is Γ_o/a_o . For the two-vortex problem (Case II), these parameters are applicable to the inner primary vortex since, as will be seen, it is the one responsible for the initial interaction with the wall and the formation of the secondary vortex. In addition, temporal evolution is considered relative to a time offset t_o at which the primary vortex effect on the overall wall heat transfer is perceptible. This offset is determined by finding the time at which the radially-averaged Nusselt number starts to deviate from the unsteady semi-infinite heat diffusion solution (see Figure 3.15a and section 3.4). Thus, by plotting the evolution of Nusselt number versus $t^* = (t - t_o)/(a_o^2/\Gamma_o)$, the period corresponding to the primary vortex approaching the wall with no significant vortex-wall interaction is removed from the history. This makes the results independent of the initial vortex ring height above the wall. Similarly, to remove the dependence on the initial vortex ring radius, R_o is subtracted from r when presenting the radial coordinate information.

The choice of a_o as a length scale is judged to be more appropriate than the vortex-ring radius R_o . To clarify, consider two vortex rings with equal initial strength, core radius and core center location above the wall but with one ring having a significantly larger ring radius. This will cause a difference in the self-induced velocity and, hence the speed at which the rings approach

the wall. However, once both rings interact with the wall, the local induced velocity, surface pressure gradient, etc., are expected to be primarily linked to the core rather than the ring radius.

3.1.2. Calculation of Vortex Characteristics

While the PV is identified by region of the same sign (positive) vorticity, the SV is identified using the "Q-criterion" in order to separate it at earlier time of formation from the BL vorticity which has the same sign as the SV. The "Q-criterion" is a method used to determine the characteristics of a vortex, specifically, the vortex-core area and the boundary of the vortex core (see Hunt *et al* [32] and Jeong and Hussain [33]) and it is identified by applying the equation:

$$Q = \frac{1}{2} (\| \Omega \|^2 - \| S \|^2) > 0$$
 (3.1)

where (Ω) and (S) are the antisymmetric (rate of rotation) and symmetric (rate of strain) parts of the velocity gradient tenor (∇u) . $\|\Omega\|$ and $\|S\|$ are the Euclidian norms of Ω and S respectively. The terms above are mathematically represented in Equations 3.2 through 3.7 below:

$$\nabla u = S + \Omega \tag{3.2}$$

$$S = \frac{1}{2} [\nabla u + \nabla u^T] \tag{3.3}$$

$$\Omega = \frac{1}{2} \left[\nabla u - \nabla u^T \right] \tag{3.4}$$

$$|| S || = [\operatorname{tr}(SS^T)]^{1/2}$$
 (3.5)

$$\parallel \Omega \parallel = [\operatorname{tr}(\Omega \Omega^T)]^{1/2} \tag{3.6}$$

where tr(a) is the trace of the $(n \times n)$ square matrix A whose entries (a_{ii}) of *i*th row and *i*th column are used to compute the trace as defined below:

$$tr = \sum_{i=1}^{n} a_{ii} \tag{3.7}$$

The procedure for the derivation of the matrices of the strain rate and the rotation rate components is given in Appendix B. All the velocity derivatives appearing in the above equations are calculated using the second-order-accurate finite difference (see Equations 2.2 through 2.4). Once the SV core boundary is identified (i.e. Q boundary equal to 10% of Q_{max}), the center of the vortex is found by finding the position of the maximum vorticity inside the core.

As Equation 3.1 shows, a vortex is identified in a region where rotational effects dominate over those of deformation. To give a sense of what this criterion yields in the case of a well-defined vortex flow with known core radius, The Q-criterion is applied to a Gaussian vortex with vorticity distribution given by Equation 2.5. Figure 3.1 shows the vorticity distribution of the Gaussian vortex, along with two circles corresponding to the core radius a_o of the vortex (green line) and that determined using the Q-criterion (blue line). As seen from the figure, the Q-criterion gives a result comparable to a_o , which is about 10% more than the core radius of the vortex.

The circulation Γ of a vortex is calculated by integrating the vorticity over the area A occupied by the vortex, specifically:

$$\Gamma = \int_{A} \omega \, dA \tag{3.8}$$

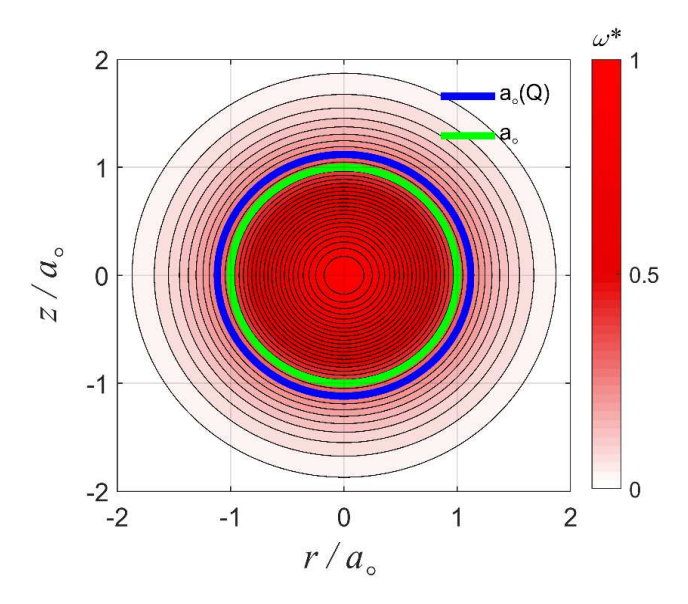


Figure 3.1 Vorticity distribution of a Gaussian vortex demonstrating the vortex border as defined by the core radius and the Q-criterion (Equation 3.1).

Equation 3.8 is evaluated numerically by multiplying the vorticity of each node (inside the specified vortex) by the area of the grid element and then summing the results to find the total circulation. Two methods are used to determine the integration area of Equation 3.8. The first method, used for calculation of the circulation of the PV, simply integrates *all* positive vorticity present within the domain. On the other hand, the second method is used for calculation of the circulation of SV by integrating the negative vorticity over the area encompassed by the borders identified using the Q-criterion. This automatically excludes the region of the BL, which also possess negative vorticity, from the secondary vortex. The vorticity field and the vortex border calculated by the Q-criterion method for SV from Case I are exemplified in Figure 3.2 at a the early time of SV formation, where the vortex is still connected to the BL.

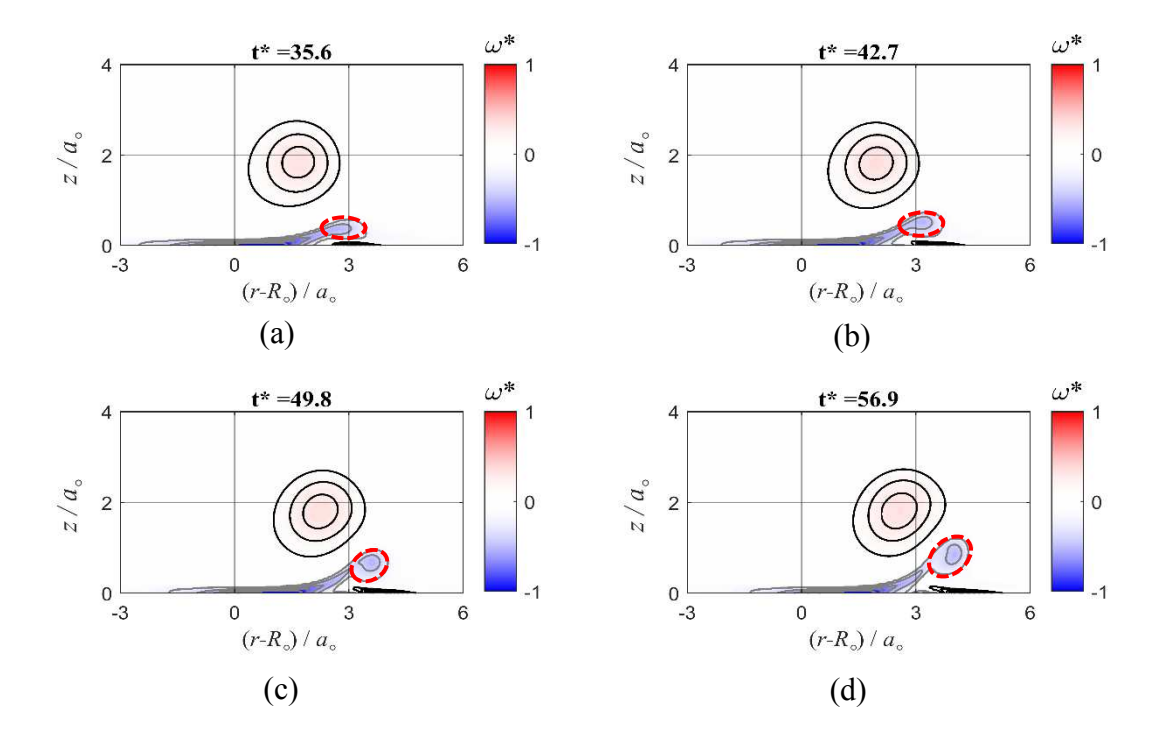


Figure 3.2 Time evolution of the vorticity field (Case I), showing an example snapshots during the early stages of SV formation. The broken red line represents the SV border calculated by the Q-criterion.

3.1.3. Wall Friction Coefficient and Nusselt Number Calculation

The wall friction coefficient (C_f) and the radial distribution of Nusselt number (Nu_r) are computed using:

$$C_f = \frac{\tau_w}{\frac{1}{2}\rho \left(\frac{\Gamma_o}{a_o}\right)^2} = \frac{\mu \frac{\partial u_r}{\partial z}\Big|_{z=0}}{\frac{1}{2}\rho \left(\frac{\Gamma_o}{a_o}\right)^2}$$
(3.9)

$$Nu_r = \frac{L_0}{T_\infty - T_W} \frac{\partial T}{\partial z} \Big|_{z=0}$$
 (3.10)

where μ is the dynamic viscosity and L_o is a characteristic length; taken here as the radial extent of the heated wall (a different representation of Nu_r , based on the thermal boundary layer thickness will also be discussed in Chapter 4). A second-order-accurate forward finite difference scheme (Equation 2.3) is employed to compute the derivatives in Equations (3.9) and (3.10). Higher-order finite difference formulae are also tested without significant change in the outcome.

3.1.4. Separation Detection

As will be seen in Section 3.3, the radial distribution of Nusselt number (Nu_r) exhibits a local minimum for all time instants. The r location of this minimum is always found in the vicinity of the boundary layer separation point (which is predominantly found directly beneath or on the "upwash side" of the vortex). In most instants, the separation location is found to coincide with the location of zero wall friction coefficient ($C_f = 0$). However, in the time period between the formation of the SV and its subsequent movement away from the wall, a secondary separation of a positive-vorticity boundary layer is formed beneath the SV (see Figure 3.3) which makes identification of the primary-vortex-induced separation point (hereafter referred to as the primary separation point) using $C_f = 0$ inaccurate. During these periods, it is found that the primary separation point is more properly identified with a local minimum in C_f . This is demonstrated in Figure 3.3, where the "primary separation point", associated with the negative-vorticity boundary layer originating from beneath the PV (seen in both subplots a and b in Figure 3.3), is compared to the "secondary separation point" of the positive-vorticity boundary layer, forming beneath the SV (seen in subplot b). The lifting of the positive-vorticity boundary layer causes the formation of a new negative-vorticity boundary layer next to the old negative-vorticity boundary layer, and the disappearance of the negative to positive vorticity transition ($C_f = 0$) at the separation point of the boundary layer beneath the PV. In this case, the separation point of the original negative-vorticity

boundary layer (primary separation point) appears to correspond to a local minimum in the wall shear stress.

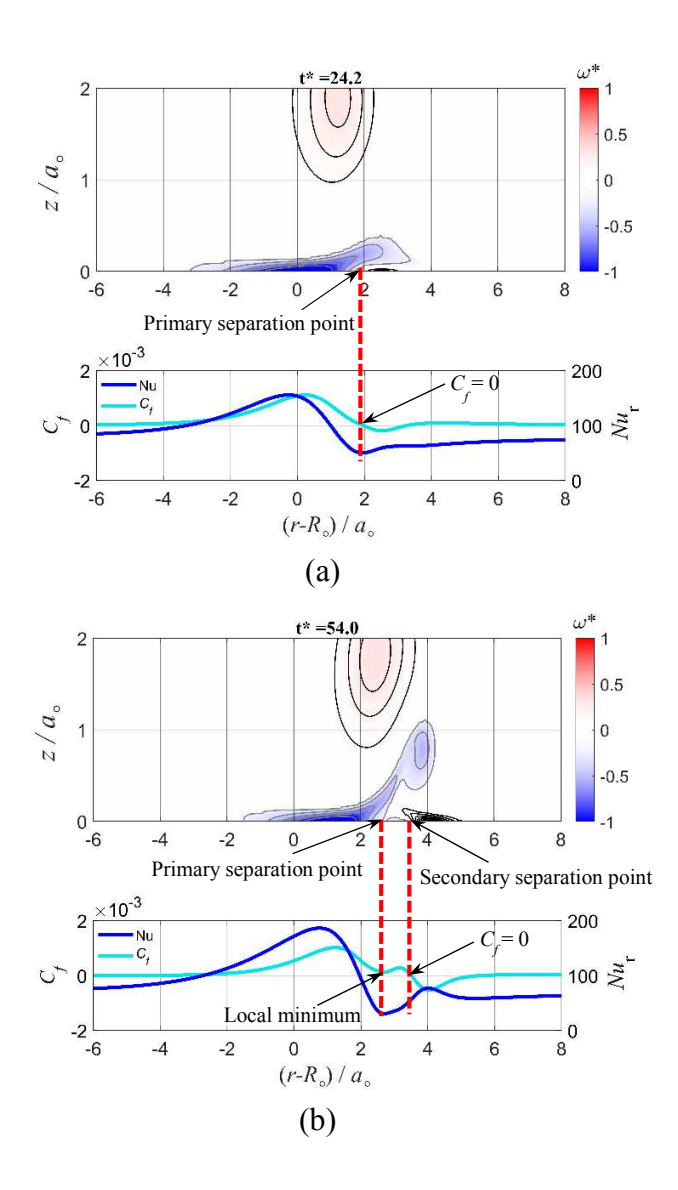


Figure 3.3 a) and b) show two snapshots of the normalized near-wall vorticity field and the concurrent radial distribution of the wall friction coefficient (C_f) and Nusselt number (Nu_r) of Case I. The ordinate is stretched relative to the abscissa in the vorticity-field plot to magnify the view, distorting the appearance of the flow features.

3.2. Evolution of the Flow Field and Nusselt Number

Figures 3.4 through 3.6 provide snapshots of the vorticity field $\omega^* = \omega a_o^2/\Gamma_o$, near-wall temperature field $\theta = (T - T_w)/(T_\infty - T_w)$, and the radial distribution of wall-friction coefficient (C_f) and local-Nusselt number (Nu_r) for all three cases investigated. The time instants at which the snapshots are captured, and the presentation style are kept the same in all three figures. Figures 3.4a to 3.4f show a time sequence from Case I, depicting a single vortex ring as it interacts with the heated wall. Each subplot in the figure contains the normalized vorticity field (top), the normalized near-wall temperature field (middle), and the concurrent C_f and Nu_r .

Between Figures 3.4a and 3.4b, the PV approaches the wall while moving radially outwards and the BL deforms. The wall shear stress is highest beneath the PV and, the Nusselt number is seen to have a local maximum in the same vicinity, but not directly beneath the PV center. Consistent with the literature, the maximum Nu_r is always seen on the "downwash" side of the vortex, and the temperature field also shows that the TBL (the zone of dense contour lines near the wall) is thinnest in the vicinity of the local Nu_r maximum. In fact, these two locations seem to coincide as seen from the plots of the Nusselt number distribution, where the black broken line identifies the location of the thinnest TBL. The thermal boundary layer thickness δ_{th} is defined as the z coordinate of the isotherm $\theta = (T - T_w)/(T_\infty - T_w) = 0.99$.

As time progresses, the BL separates leading to the formation of the SV, which is seen first in Figure 3.4b. In Figure 3.4b through 3.4f, The SV and PV mutually interact, causing the PV to "rebound", i.e. move away from the wall and radially inwards. Meanwhile, the SV orbits the PV, moving from outboard to inboard of the PV.

During the flow evolution, the peak C_f and Nu_r remain beneath the PV. However, the radial location of the two peaks do not coincide, with the Nu_r peak mostly found at a slightly smaller radial location than that of the C_f peak (this will be demonstrated more clearly in Section 3.3). Moreover, the C_f and the Nu_r distributions have different shapes during the formation and early evolution of the SV, suggesting that Reynolds analogy is not applicable during the PV-wall interaction. Overall, the observations suggest a direct connection between the PV and the maximum Nu_r , where, likely, the near-wall "induced" velocity by the PV causes thinning of the TBL beneath the PV, and hence intensification of the *wall-normal* temperature gradient at the wall, and associated enhancement in the wall heat transfer. This hypothesis will be explored further in Chapter 4, employing boundary-layer-resolved analysis.

For all time instants in Figure 3.4, the radial distribution of Nu_r also exhibits a local minimum. The r location of this minimum is always found in the vicinity of the boundary layer separation point (which, as will be seen in Section 3.4, is mostly found directly beneath or on the "upwash side" of the vortex). This may be seen in the line plots in Figure 3.4, where the separation location is identified with a vertical broken gray line.

Figures 3.5a to 3.5f exhibit the pair of vortex rings as they interact with the heated wall (Case II). The two vortex rings mutually interact before they reach the wall (not depicted in Figure 3.5). The inner vortex (the core center of which is initially located at a smaller radial location than the outer vortex) moves towards the wall and in the positive radial direction faster than the outer vortex due to a faster self-induced velocity coupled with the influence of the outer vortex. In Figure 3.5b and 3.5c, the two rings orbit around each other, while the initially smaller ring is getting stretched and "squeezed" between the outer ring and the wall, before the two rings completely merge (Figure 3.5e). In the time between that corresponding to Figures 3.5c and 3.5d, the SV forms

due to the separation of the BL and the remainder of the flow evolution becomes qualitatively similar to that of the single vortex ring interaction with the wall. This similarity includes the overall characteristics of the Nu_r radial distribution and the connection of its peak and valley with the radial location of the PV, the maximum wall-friction coefficient, the primary separation point and the TBL thickness.

Figures 3.6a to 3.6f show the evolution of Case III vortex ring (with twice the circulation and twice the core radius of Case I) as the ring interacts with the heated wall. As would be expected, the overall evolution of the flow is similar to Case I while exhibiting quantitative differences. The details of the quantitative differences between the three cases will be discussed further in the remainder of the document.

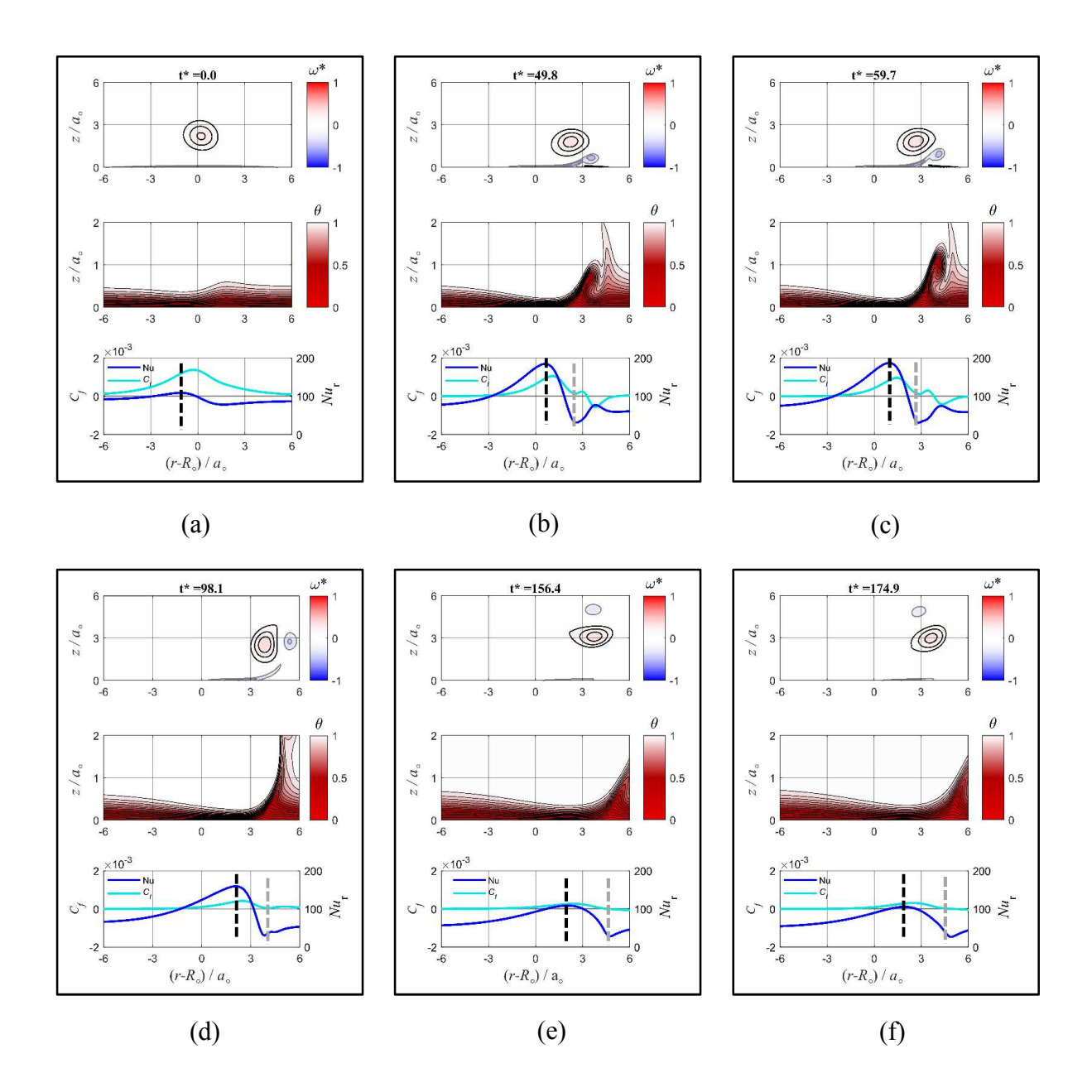


Figure 3.4 Time evolution of the initially-Gaussian-core vortex as it interacts with a heated wall (Case I). Shown at each time instant: the azimuthal-vorticity field (top), the near-wall temperature field (middle) and line plots (bottom) of Nusselt number (Nu_r) and the wall-friction coefficient (C_f). The broken gray line represents the primary separation point of the hydrodynamic boundary layer beneath the PV, and the broken black line depicts the location of the minimum δ_{th} .

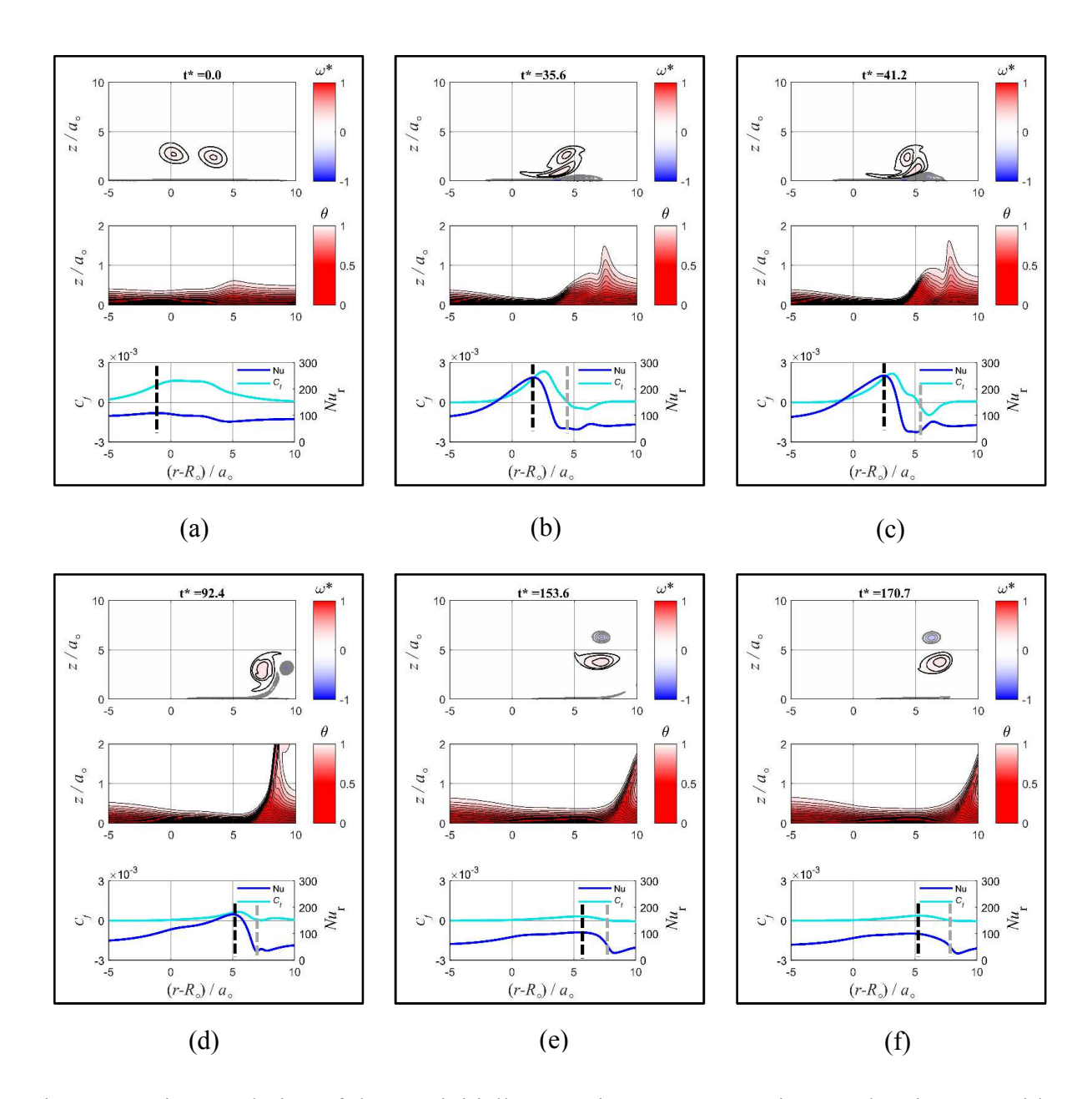


Figure 3.5 Time evolution of the two initially-Gaussian-core vortex rings as they interact with a heated wall (Case II). Shown at each time instant: the azimuthal-vorticity field (top), the near-wall temperature field (middle) and line plots (bottom) of Nusselt number (Nu_r) and the wall-friction coefficient (C_f). The broken gray line represents the primary separation point of the hydrodynamic boundary layer beneath the PV, and the broken black line depicts the location of the minimum δ_{th} .

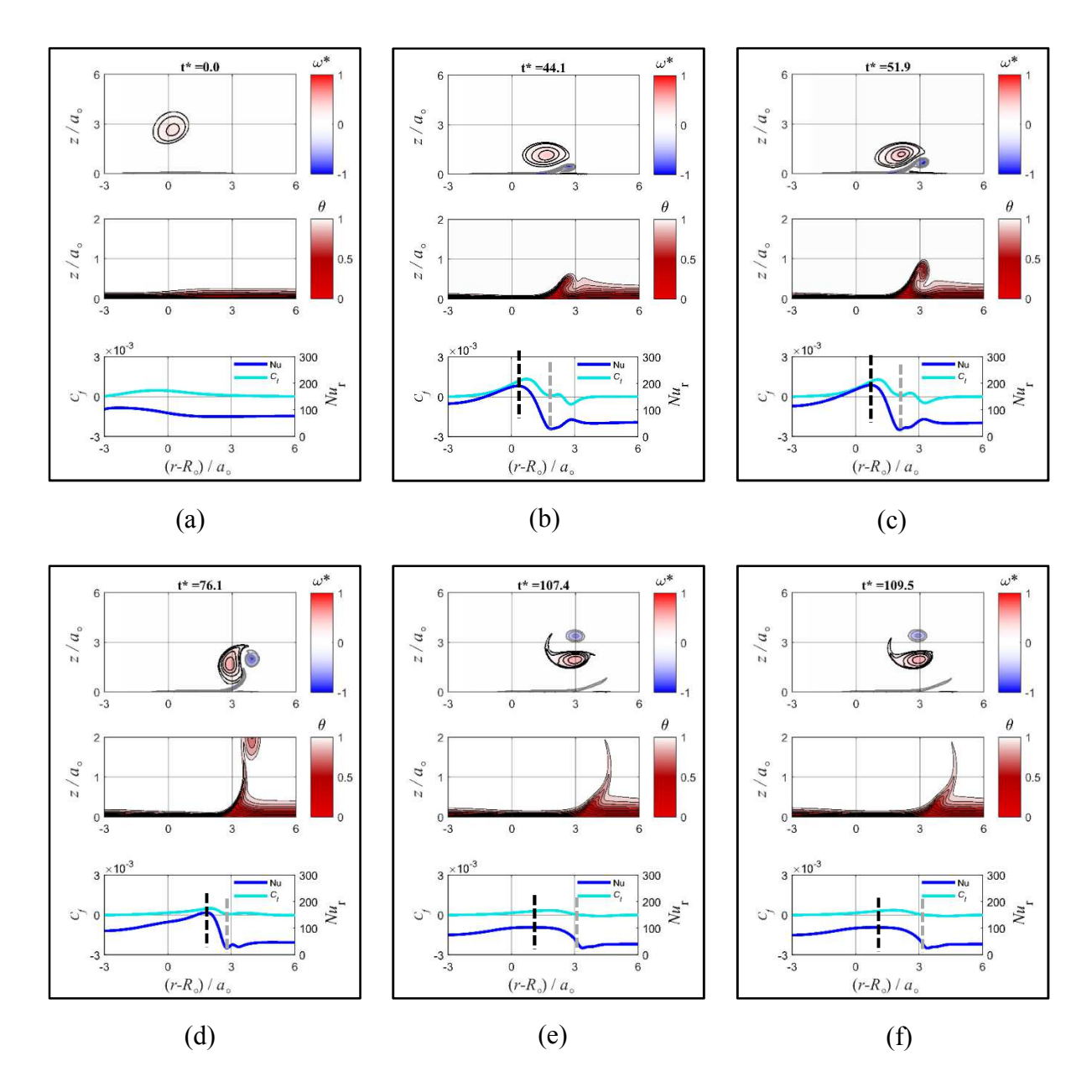


Figure 3.6 Time evolution of the initially-Gaussian-core vortex (with twice the initial circulation and core radius of Case I) as it interacts with a heated wall (Case III). Shown at each time instant: the azimuthal-vorticity field (top), the near-wall temperature field (middle) and line plots (bottom) of Nusselt number (Nu_r) and the wall-friction coefficient (C_f). The broken gray line represents the primary separation point of the hydrodynamic boundary layer beneath the PV, and the broken black line depicts the location of the minimum δ_{th} .

3.3. Heat Transfer Enhancement: Maximum Nu_r

To analyze the heat transfer enhancement associated with vortex-wall interaction, the maximum Nu_r value ($Nu_{r,max}$) and radial location ($r_{Nu_{r,max}}$) where the maximum occurs are found at each time instant. The existence of possible correlation between these quantities and the PV trajectory, the wall-friction coefficient and the TBL thickness is examined and compared between the three cases studied. The evolution of the maximum Nu_r is depicted in Figure 3.7 versus time in both dimensional and non-dimensional forms. The dimensional plot is included to enable comparison with Nu_r for the semi-infinite transient-diffusion solution (based on Equation 2.9) for reference. Overall, the CFD results are substantially higher than those of the diffusion-solution, commensurate with the expected enhancement of the heat transfer rate due to convective versus diffusive heat transfer.

For all cases, the maximum Nu_r exhibits up/down modulation with time. As seen earlier, in the discussion of Figures 3.4 through 3.6, the maximum Nu_r appears to be predominantly affected by the PV. Consequently, the modulation behavior seen in Figure 3.7 is likely caused by changes in the location and characteristics of the PV. These changes initially manifest themselves as an increasing influence of the PV as it gradually approaches the wall, which appears to produce a corresponding increase in $Nu_{r,max}$ up to a local peak for all three cases (which corresponds to snapshot c in Figures 3.4 through 3.6) within the t^* range of 40-60. This peak is largest for the case of two vortex rings, demonstrating an ability to produce a higher heat transfer rate in comparison to the single vortex ring in both Case I and Case III; i.e. "before and after pairing".

As time progresses, the initial $Nu_{r,max}$ peak decays with time, reaching a local minimum (corresponding to snapshot f in Figures 3.4 and 3.5) in the vicinity of $t^* = 174.9$ and 170.5, for

Cases I and II respectively, before starting to increase again. For Case III, the local minimum occurs at $t^* = 109.5$. The connection between the temporal evolution of the maximum Nusselt number and some of the vortex characteristics (specifically, the circulation and the radial and wall-normal location of the PV core center) is examined further below.

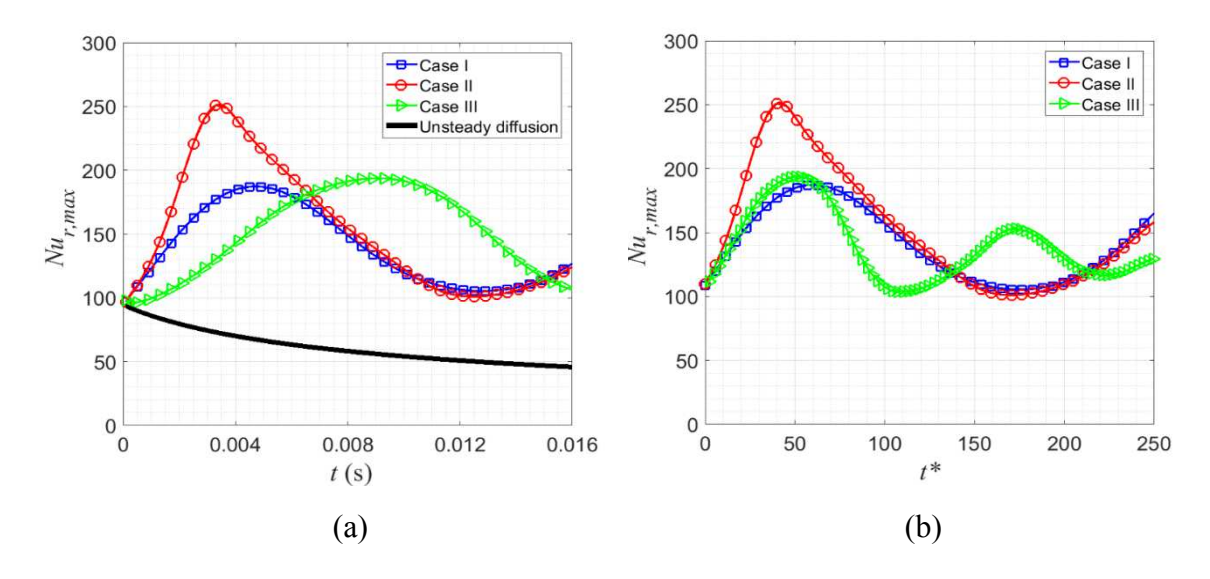


Figure 3.7 Comparison of the maximum Nusselt number evolution with time for the one- and the two-vortex rings interacting with a heated wall: a) dimensional, and b) non-dimensional time. The semi-infinite transient-diffusion solution (based on Equation 2.9) is included for reference in (a).

In order to examine possible connections between the vortex strength and the enhancement in the heat transfer, the circulation associated with the primary vorticity is calculated from the area integral of *all* positive vorticity. For Case II, this accounts for the circulation of both primary vortices. As seen in Figure 3.8, which shows the evolution of circulation versus time in both dimensional and non-dimensional forms, the circulation remains relatively constant initially before exhibiting monotonic decay with time. The decay starts approximately around the time when the secondary vortex forms. This decay is expected due to vorticity cancellation associated with the diffusion of negative and positive vorticity. Interestingly, the initial significant rise of $Nu_{r,max}$ to

its peak value in Figure 3.7 takes place during the time when the circulation is constant. Thus, the initial heat transfer enhancement for a given case is not connected to change in the vortex strength. Furthermore, since Case II and Case III have the same initial circulation, yet the former case leads to better heat transfer enhancement, this demonstrates that the initial configuration of the vortices (i.e. the specific spatial distribution of vorticity) can have a significant effect on the wall heat transfer.

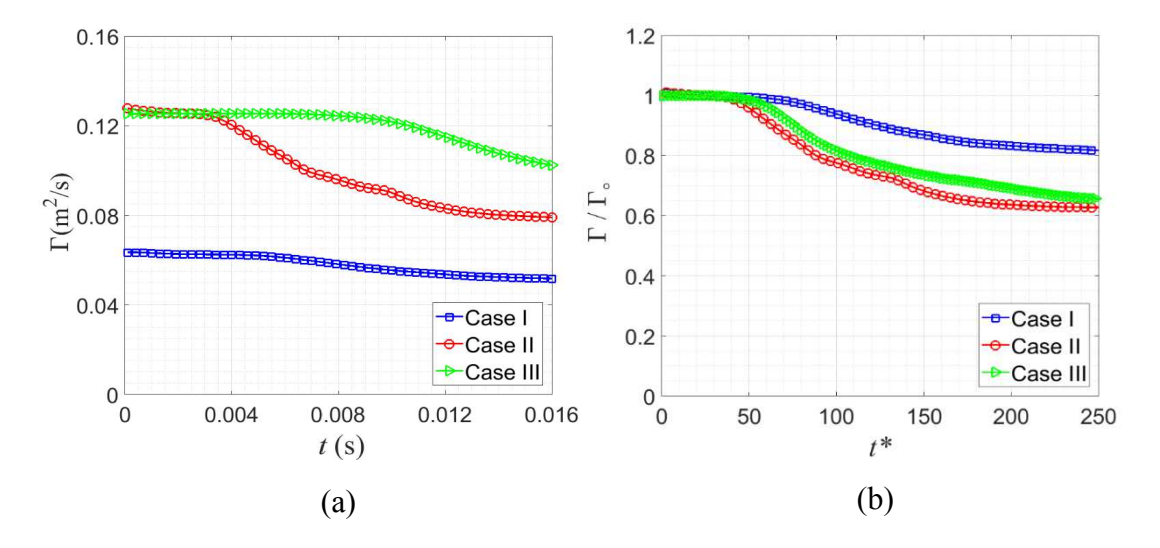


Figure 3.8 Comparison of the temporal evolution of the total circulation associated with the primary vorticity for the one- and the two- vortex rings interacting with a heated wall: a) dimensional; and b) non-dimensional plot.

Figure 3.9 shows the time evolution of the radial locations of the $Nu_{r,max}$, the PV core center, the maximum wall friction coefficient, and the minimum TBL thickness $(\delta_{th,min})$ for all cases. For Case II, initially there are two curves representing the radial loci of the inner and the outer vortices $(R_{PV,i})$ and $R_{PV,o}$ respectively), until the two vortices fully merge into a single vortex and only a single vorticity peak can be detected in the core (starting from approximately $t^* = 150$). A magenta line depicts the average of these two loci. For all cases, Figure (3.9) reveals that

the $Nu_{r,max}$ is always located at a smaller radial location than that of the PV core center (i.e. inboard, or to the left of the PV, where a downwash flow towards the wall is present). In addition, the radial location of the maximum C_f generally falls between the radial location of the PV core and that of the $Nu_{r,max}$ (although at certain times the two locations might approximately coincide). Significantly, $Nu_{r,max}$ is practically collocated with the location of the thinnest TBL.

The main difference between the single-vortex and the two-vortex radial core-center trajectories is that for the latter, the inner and the outer rings undergo some leap-frogging before merging into a single vortex. Referring to Figure 3.9b, initially, the radial location of the inner vortex is smaller than that of the outer. The two vortices then exhibit four leap-frogging actions, in which the inner moves twice ahead of, then back behind the outer vortex in the radial direction. This type of mutual interaction is reflected in the "out-of-phase sinusoidal" modulation of the radial location of the cores of these vortices before merging. Interestingly, these sinusoidal modulations of the vortices radial trajectory are not seen in either the radial location of the maximum C_f or the peak Nu_r . In fact, the trajectory of the maximum wall friction coefficient and $Nu_{r,max}$ are very similar in shape to the average trajectory of the inner and outer vortices (shown in magenta in Figure 3.9b). Moreover, all of these trajectories are qualitatively similar to those for Cases I and III.

Notable is that, in non-dimensional terms, Case III evolves faster than the other two cases, so that over the same *non-dimensional* time duration, the qualitative behavior seen for Cases I and II is repeated twice in Case III. This is also evident in Figure 3.7b, where two cycles of $Nu_{r,max}$ oscillation are captured within the same t^* window for Case III, in comparison to only one cycle for Cases I and II. This behavior is associated with the occurrence of two PV rebound cycles in

Case III, in comparison to a single cycle in Cases I and II. The first rebound cycle is associated with the interaction with the SV, and the second with the formation of a tertiary vortex. Qualitatively, the behavior of the PV associated with the tertiary and higher-order vortices is similar to that resulting from interaction with the SV. Therefore, the flow behavior is analyzed through the first rebound cycle only.

The correlation between the magnitude of the maximum local Nu and the wall-normal location of the PV core center (Z_{PV}) is examined with the aid of Figures 3.10 for all cases. In Figure 3.10a (Case I), it is evident that some correlation exists between the proximity of the PV to the wall and $Nu_{r,max}$: down and up movement of the PV are followed by increase and decrease, respectively, of $Nu_{r,max}$; i.e. the closer the PV is to the wall, the stronger the peak heat transfer rate. However, a delay Δt is observed between the change in Z_{PV} and the corresponding change in $Nu_{r,max}$. The same type of correlation between Z_{PV} and $Nu_{r,max}$ is seen for Cases II and III in Figures 3.10b and 3.10c respectively.

The time delay Δt implies the presence of some inherent dynamics in the response of the temperature field to variation in the velocity field. These dynamics are hypothesized to lead to the inability of the temperature field, and hence $Nu_{r,max}$, to respond immediately to variation in the PV vortex location (this point is explored further in Chapter 4 with the aid of a simple analytical problem). Interestingly, the faster modulation of the inner- and outer-vortex core-center location due to leap frogging in Case II do not appear in the $Nu_{r,max}$ evolution. As was the case for the radial trajectory of the PV for Case II (Figure 3.9b), variation in $Nu_{r,max}$ seems to correspond better to variation in the *average* wall-normal trajectory of the inner and outer vortices.

Another interesting observation from Figure 3.10 is regarding the difference between the single- (Cases I and III) and the two-vortex (Case II) situations. Because of the interaction/merging process of the inner and outer vortices, the inner vortex reaches closer to the wall in Case II relative to Cases I and III (reaching 50% and 80% of the minimum height of the PV in these two cases respectively). This may be the primary factor leading to the substantially larger $Nu_{r,max}$ in the two-vortex-ring case Figure 3.7. The plots in Figure 3.10 also include the history of the minimum TBL thickness (magnified five times). Consistent with the earlier observations, the TBL thickness variation is "180 degrees" out of phase with $Nu_{r,max}$. Specifically, peaks in the latter coincide with minima of the former and vice versa.

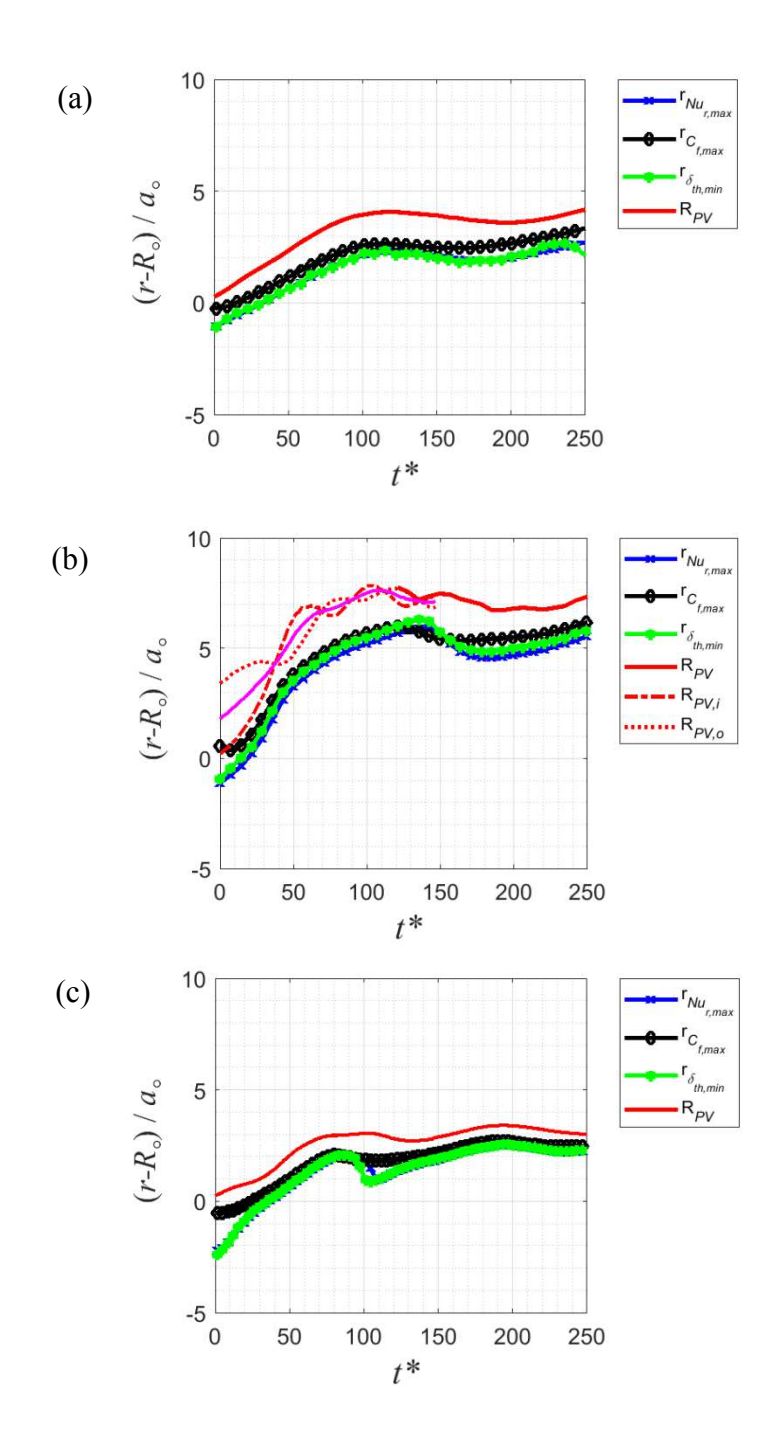


Figure 3.9 Temporal evolution of the radial locations of the maximum local Nusselt number, the maximum wall friction coefficient, the minimum TBL thickness, and the core center of the primary vortex: a) Case I; b) Case II; c) Case III. The magenta line in (b) displays the average of the radial loci of the inner and the outer vortex cores.

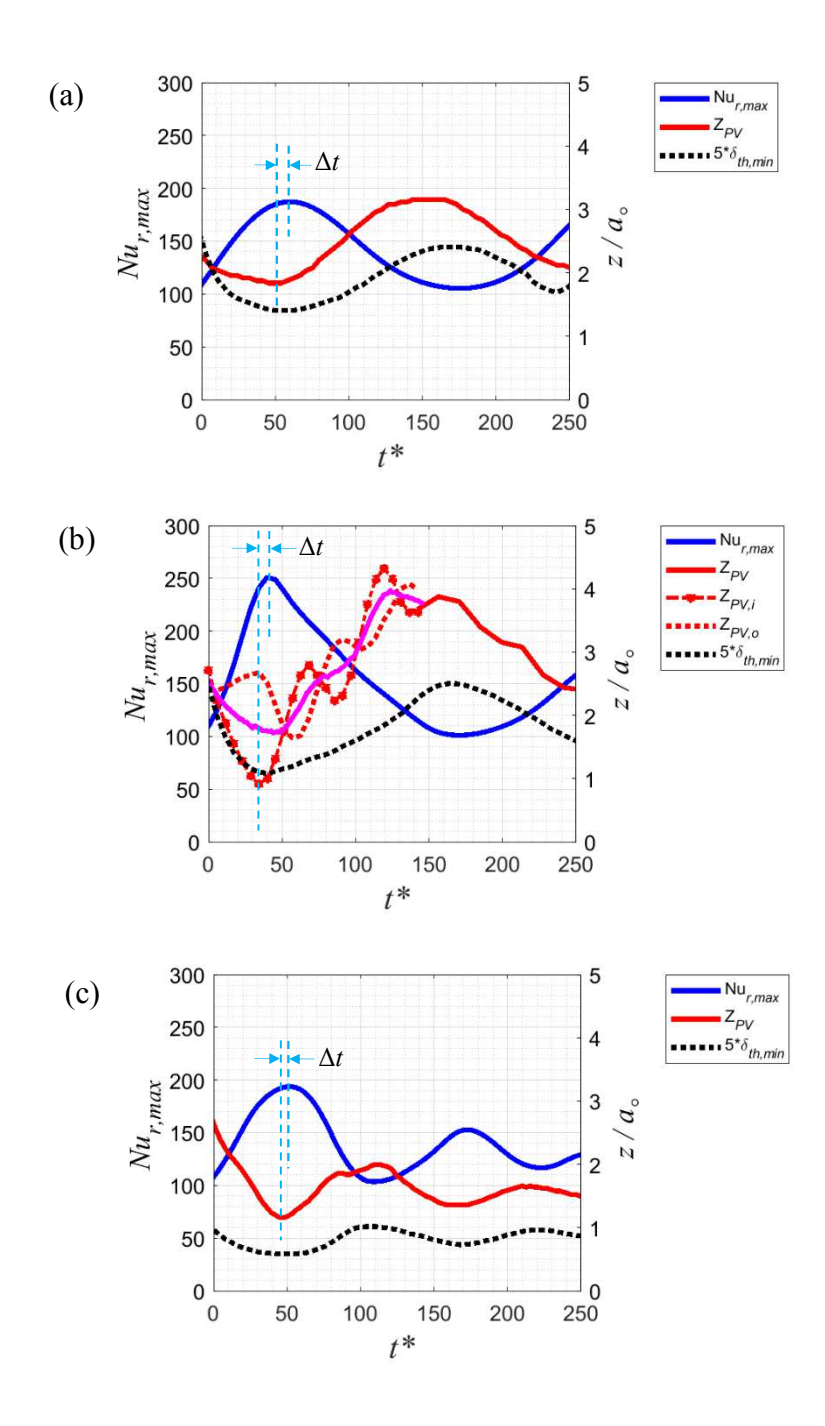


Figure 3.10 Temporal evolution of the maximum local Nusselt number, the minimum TBL thickness, and the wall-normal location of the core center of the primary vortex: a) Case I; b) Case II; c) Case III. The magenta line in (b) displays the average of the radial loci of the inner and the outer vortex cores.

3.4. Heat Transfer Deterioration: Minimum Nur

The evolution of the minimum local Nu ($Nu_{r,min}$) for all cases is plotted in Figure 3.11a versus t to compare with the unsteady diffusion. Figure 3.11b depicts the same results versus t^* . An immediate observation is that the smallest Nu_r produced in vortex-wall interaction is significantly smaller than even that associated with unsteady diffusion. Though not perfectly collapsing in non-dimensional form, the results in all cases seem to lead to a practically similar $Nu_{r,min}$ history, both qualitatively and quantitatively.

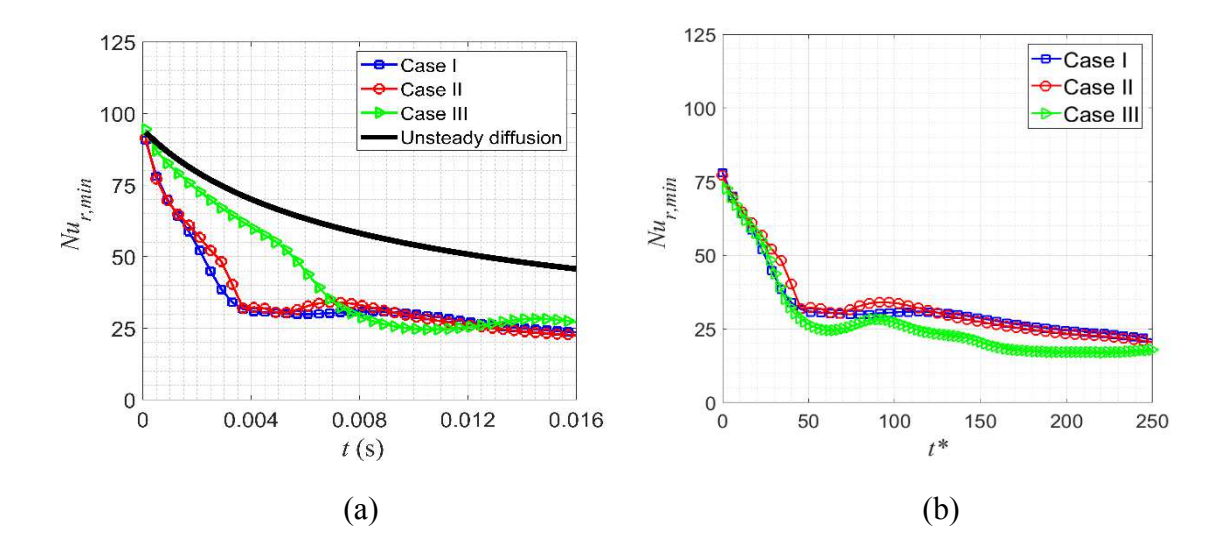


Figure 3.11 Comparison of the minimum Nusselt number evolution with time for the one- and the two- vortex rings interacting with a heated wall: a) dimensional; and b) non-dimensional time. The semi-infinite transient-diffusion solution (based on Equation 2.9) is included for reference in (a).

Figure 3.12 depicts the temporal evolution of the radial locations of $Nu_{r,min}$, the PV core center, and the boundary layer separation location (r_{PS}) . As mentioned earlier, because a secondary separation zone forms beneath the SV when the latter is sufficiently close to the wall, only the primary separation location closest to the PV is considered in order to focus on the PV-driven separation process. As seen from Figure 3.12, the $Nu_{r,min}$ for each case stays in the vicinity of the

separation point, beneath or outboard (on the "upwash" side) of the PV, which is an indication of the connection between the deterioration of Nu and the thickening and unsteady separation of the boundary layer (this point will be investigated in more details in Chapter 4). The "jumps" seen at certain times in the primary separation point location occur at time periods where a secondary separation zone is present and identifying the separation point using the wall shear stress is difficult. As discussed earlier, during such times, a local minimum in the wall friction coefficient (see Figure 3.3) seems to work better in identifying the primary separation point than $C_f = 0$. However, even this different criterion is imperfect, which leads to the observed jumps in the separation location.

Figure 3.13 depicts variation in $Nu_{r,min}$ and the concurrent change in the z location of the PV core center (Z_{PV}). Overall, the magnitude of the $Nu_{r,min}$ does not seem to be closely correlated with the proximity of the PV to the wall as is the case for $Nu_{r,max}$ (Figure 3.10). More specifically, while Z_{PV} exhibits sinusoidal-like down/up change, $Nu_{r,min}$ initially decreases monotonically then reaches an apparent plateau. Careful inspection of videos, from which the snapshots in Figures 3.4 through 3.6 are taken, reveals that the initial decrease in $Nu_{r,max}$ is accompanied by thickening of the boundary layer and early development of the separation zone, within which $Nu_{r,max}$ occurs. Subsequently, once the SV is sufficiently removed from the wall, the flow very near the wall within the separation zone seems to reach a state that is approximately steady and predominantly unaffected by further evolution of the primary and higher-order vortices. In this late stage of evolution, the rate of decay of $Nu_{r,min}$ looks comparable to that of unsteady diffusion (see Figure 3.11).

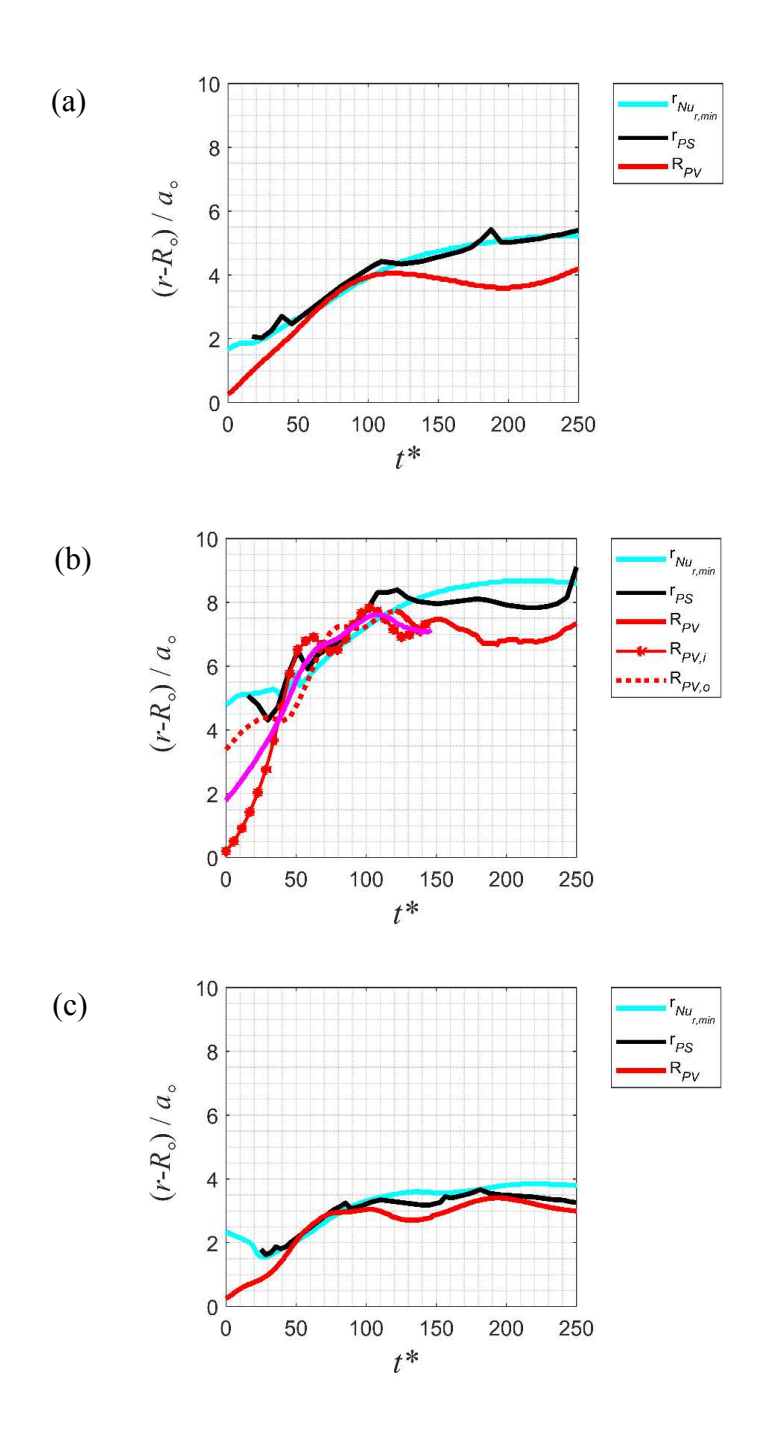


Figure 3.12 Temporal evolution of the radial locations of the $Nu_{r,min}$, the primary separation point and the core center of the primary vortex: a) Case I; b) Case II; c) Case III. The magenta line in (b) displays the average of the radial loci of the inner and the outer vortex cores.

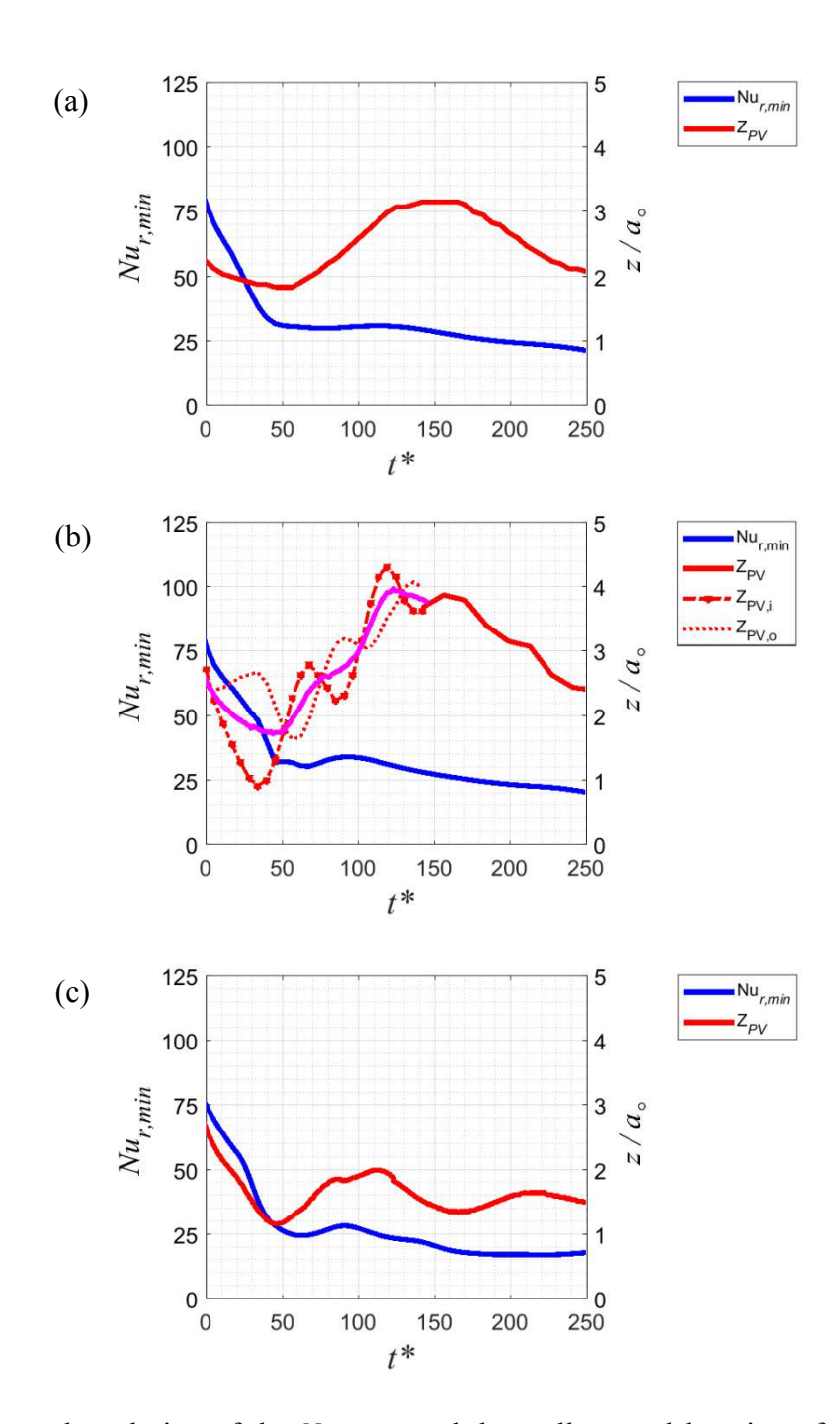


Figure 3.13 Temporal evolution of the $Nu_{r,min}$ and the wall-normal location of the core of the primary vortex: a) Case I; b) Case II; c) Case III. The magenta line in (b) displays the average of the radial loci of the inner and outer vortex cores.

3.5. Overall Effect: Average Nu_r

The results from Sections 3.3 and 3.4 demonstrate that at a given time instant, vortex interactions with the wall have both positive and negative influences on the enhancement of the wall heat flux. To examine the net effect of the interactions, the radial distribution of Nusselt number is averaged over the radial domain influenced by vortex-wall interaction. Defining a domain of influence is necessary in order to only take into account the radial region that is affected by the interaction of the vortices with the wall; enabling a fair comparison among the cases. The domain of influence in this case is defined, somewhat arbitrarily yet consistently, as that extending from the axis of symmetry to the maximum radial coordinate of the secondary vortex core center. Another criterion was also applied based on the fact that sufficiently far away from the axis of symmetry, Nu_r reaches a plateau corresponding to the unsteady diffusion value. In this criterion, the domain of influence is defined as that extending from r = 0 to where Nu_r asymptotes to within 10% of unsteady diffusion. Figure 3.14 visually demonstrates both criteria for Case I for the time step where the center of the SV core reaches its maximum radial location. Both criteria give similar results.

Because of the axisymmetry of the present problem, the radially-averaged Nusselt number is computed using an area-weighted average; specifically:

$$Nu_{r,avg} = \frac{\int\limits_{\theta=0}^{\theta=2\pi} \int\limits_{r=0}^{r=r_{SV,max}} Nu_r r dr d\theta}{\pi r_{SV,max}^2}$$
(3.11)

where, $r_{SV,max}$ is the maximum radial location of the domain of influence.

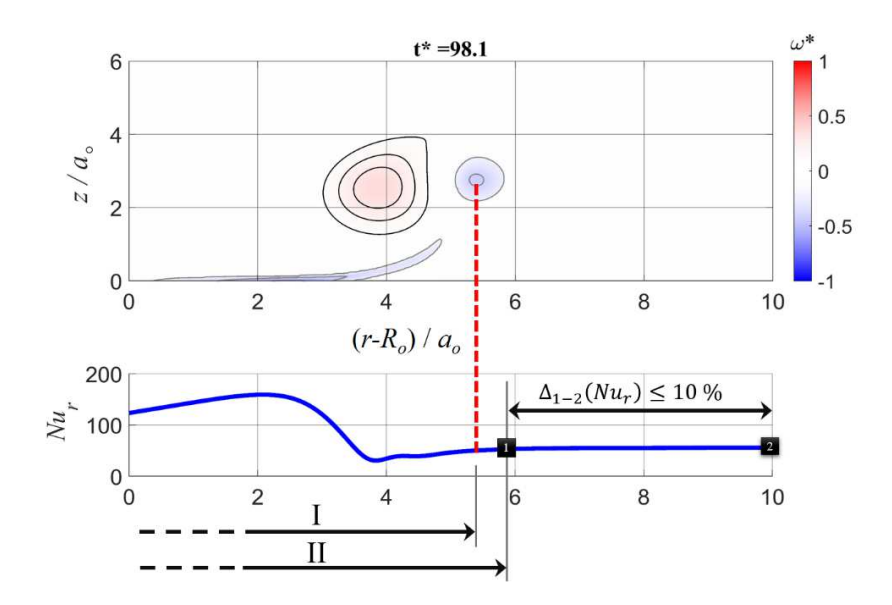


Figure 3.14 A snapshot of the evolution of vortex-wall interaction for Case I, demonstrating the two criteria used to define the radial domain boundary for calculation of the radially-averaged $Nu_r(t)$: vorticity field (top) and concurrent radial distribution of the Nusselt number (bottom). The figure shows the SV at its maximum radial location. (I) and (II) in the figure represent, respectively, the maximum radial location of the SV, and the radial location where Nu_r deviates by 10% from the unsteady diffusion value.

Figure 3.15 displays the temporal evolution of $Nu_{r,avg}$ for all three cases (with time shown in both dimensional and non-dimensional form). As before, the dimensional-time plot (Figure 3.15a) enables comparison with the unsteady diffusion solution. Furthermore, this plot demonstrates the difference in the initial time period t_o before the PV affects the average heat transfer for the different cases. Comparing Figure 3.15b to Figure 3.7b (where $Nu_{r,max}$ evolution is depicted), it is clear that the magnitude of the radially-averaged Nusselt number is substantially less than $Nu_{r,max}$ for all three cases. The maximum in the average Nusselt number is approximately half of the peak value of $Nu_{r,max}$, but generally $Nu_{r,avg}$ remains significantly

higher than unsteady diffusion. Thus, notwithstanding the presence of positive and negative influences of vortex-wall interaction on the heat transfer, overall the interaction improves the heat transfer rate. Moreover, similar to $Nu_{r,max}$ results, when the two vortices pair while interacting with the wall (Case II) they result in the highest heat transfer enhancement. The pre-pairing and post-pairing, single-vortex scenarios (Cases I and III respectively) produce lower, but comparatively similar average Nusselt number.

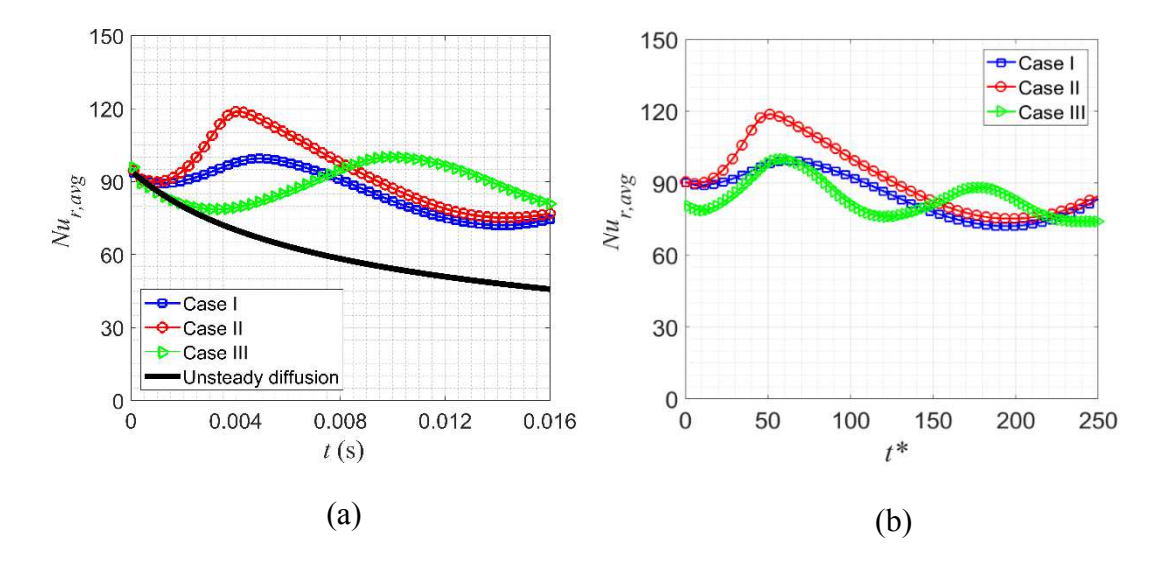


Figure 3.15 Comparison of the radially-averaged Nusselt number evolution with time for the oneand the two-vortex rings interacting with a heated wall: a) dimensional; and b) non-dimensional time. The semi-infinite transient-diffusion solution (based on Equation 2.9) is included for reference in (a).

Though Case II leads to better heat transfer rate than Case I for an isolated vortex ring/pair interaction with a heated wall, this may not necessarily produce a net *time average* enhancement in an impinging jet. In particular, in the latter case, the jet's vortex rings interact periodically with the wall. Before pairing (Case I), the frequency of the interactions will be twice that occurring during pairing (Case II). Consequently, even though a single interaction before pairing results in

less cooling of the wall than during pairing (per Figure 3.15), the number of interactions per unit time in the former case is twice the latter. Thus, in order for Case II to provide a *net* improvement in cooling relative to Case I, Case II must produce more than twice the cooling effect of Case I per interaction. The results in Figure 3.15 do not demonstrate such a strong effect. However, as will be discussed in the following paragraph, one of the main factors in limiting the cooling effectiveness of vortex-wall interaction, is boundary layer separation and formation of the secondary vortex, which is particularly strong for Case II. It is possible that with proper control of separation and the SV that the Nusselt number enhancement in Case II would be sufficiently strong to be more advantageous than Case I. This point is outside the scope of the present research.

Another noteworthy point is that in Case II, the swing between the peak and the valley of both $Nu_{r,max}$ and $Nu_{r,avg}$ (see Figures 3.7 and 3.15 respectively) is larger than in Cases I and III. That is, in Case II, once $Nu_{r,max}$ reaches its first peak, it exhibits a stronger relative deterioration during vortex-wall interaction in comparison to the other two cases. Based on the analysis in Section 3.3, this deterioration is predominantly correlated with the primary vortex rebound (i.e. moving away from the surface after reaching the initial minimum height). It is well known from the literature that this rebound is connected to the induced velocity by the SV on the PV after the formation of the former. To compare the strength of the secondary vortex among the three cases, the SV circulation is computed using the Q criterion. By integrating the vorticity within this area of SV, the vortex circulation is obtained. The use of the Q criterion to define the core area instead of integrating all negative vorticity enables exclusion of the boundary layer vorticity in calculating the circulation.

Figure 3.16 shows the history of the circulation of SV for all three cases. As seen from the figure, the SV circulation is almost twice as strong (i.e. having about twice the initial PV circulation) in Case II, in comparison to Case I and Case III. This is believed to be in part due to a stronger vortex-wall interaction brought about by the influence of vortex-vortex interaction in Case II during pairing, which causes the inner vortex to be driven to a closer distance to the wall than in Cases I and III. This can be seen in Figure 3.17, where the trajectory of the PV for all three cases is shown (for Case II, only the inner vortex trajectory is shown since the SV results from the interaction of the inner vortex with the wall).

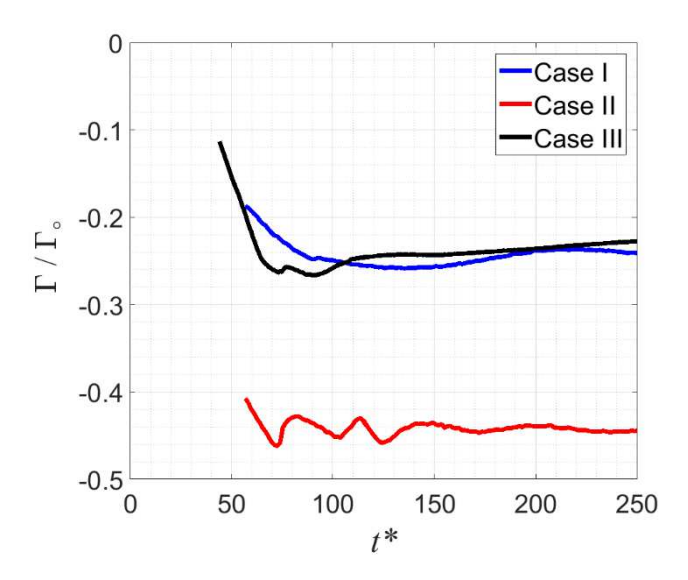


Figure 3.16 Temporal evolution of the SV circulation for all three cases.

For Cases I and III, Figure 3.17 also implicitly demonstrates the known connection between the PV rebound and the SV. Specifically, as indicated on the plot, in both of these cases, the PV starts its movement away from the wall immediately after the formation of the SV. Interestingly, for Case II, the initial phase of the rebound occurs prior to the formation of the SV. It is not difficult to see that the induced velocity by the *outer* PV drives the early phase of the rebound of the *inner* vortex. Thus, while the outer PV has a strong positive effect on the maximum Nusselt number, it

also has an adverse effect in aiding in the subsequent decay of $Nu_{r,max}$ associated with the PV rebound. However, the particular strength of the SV in Case II seems to be the primary driver of the overall strong PV rebound and $Nu_{r,max}$ decay in Case II. This may be seen by comparing the wall-normal trajectory of all three cases in Figure 3.10. In Case II, the *average* (i.e. collective) trajectory of the inner and the outer PV undergoes the largest excursion from the nearest to the highest location above the wall with the ratio of the two locations being 2.4. The corresponding ratio for Case I is 1.7 and Case II is 1.6. This highlights the stronger influence of the SV in Case II in reducing the maximum achievable Nu_r .

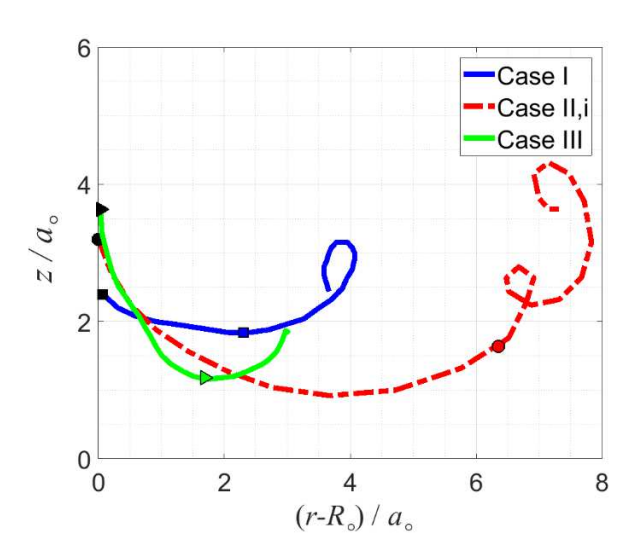


Figure 3.17 Trajectory of the core center of the PV (for Cases I and III), and the inner vortex (for Case II). The black markers on each trajectory show the initial position of the PV, while the similar-shaped colored markers on the same line indicate the initial time of formation of SV.

The above discussion implies that the primary benefit of pairing taking place while the vortices interact with the wall (Case II) is that the vortex-vortex interaction leads to deeper penetration of the inner vortex towards the wall and subsequent stronger interaction and maximum, as well as average, *Nu* (Figures 3.7 and 3.15 respectively) relative to Cases I and III. However, a

drawback of this stronger interaction is the formation of a stronger SV, which causes a larger rebound of the pairing vortices after the initial interaction and greater decay in Nu. This deterioration could offset the initial benefit of the stronger interaction with the wall. However, it is not clear if this deterioration would necessarily be important for impinging jets. As discussed earlier, secondary vortex detachment and orbiting around the PV is not generally observed in impinging jets due to the advection by the mean jet flow. Therefore, in impinging jets, scenario II may remain advantageous in comparison to scenarios I and III in terms of heat transfer enhancement.

CHAPTER 4

BOUNDARY-LAYER-RESOLVED ANALYSIS OF NUSSELT NUMBER BEHAVIOR

The results discussed in the previous chapter show that the maximum Nu_r occurs on the downwash side of the PV while the $Nu_{r,max}$ magnitude is out of phase with the wallnormal location of the PV. On the other hand, the minimum Nu_r is found in close proximity of the primary separation point with the magnitude of the former initially correlated with the wall-normal PV location. After this initial period, Nurmin magnitude is not affected significantly by further modulation in the PV's wall-normal location. In order to better understand the physics underlying these observations, a more detailed analysis is carried out in this chapter of the behavior of the thermal boundary layer and the associated near-wall flow. The analysis focuses on the area in the vicinity of the maximum and the minimum Nu_r , and is augmented with two special cases. The first case involves the computation of a zerothermal-diffusivity ($\alpha = 0$) problem, which aids in understanding the physics of heat transfer enhancement. In the second case, the boundary layer separation is eliminated by setting a zero wall shear stress ($\tau = 0$) at the heated wall as a boundary condition to help understand the physics of heat transfer deterioration. All results are described in an Eulerian frame of reference with its origin fixed to the core center of the primary vortex in the radial direction only.

The aforementioned Eulerian analysis is complemented with a Lagrangian exploration. The main point of the latter is to evaluate a recently published hypothesis ("surface renewal model") concerning the mechanisms of enhancement and deterioration of the Nusselt number due to vortex-wall interaction (Hubble *et al.* [22]). This hypothesis is based on a phenomenological

description of fluid particle trajectories near the wall during the interaction. Hubble *et al.* [22] did not have access to the near-wall boundary-layer-resolved information in formulating and supporting their hypothesis. Given that such information is available from the present study, one of the present objectives is to evaluate the basis of the renewal hypothesis.

4.1. Eulerian Analysis

4.1.1. Maximum Nu_r : Case I and Case $\alpha = 0$ Comparison

To examine the essential differences regarding the heat transfer physics for the two cases considered, specific time steps are chosen. In Figure 4.1, the evolution of $Nu_{r,max}$ for both cases are plotted, and the vertical broken lines mark the selected time steps. The first time Step is selected at $(t^* = 0)$, while the second time step $(t^* = 10)$ is selected as the $Nu_{r,max}$ for Case $\alpha = 0$ starts to diverge from the $Nu_{r,max}$ of Case I. Because there is no special characteristic in the way Nu_r of Case $\alpha = 0$ evolves (it simply monotonically increases with time), the other time steps are chosen depending on the heat transfer and the flow characteristics of Case I. Specifically, the third and the sixth time step are chosen when $Nu_{r,max}$ reaches its peak and valley $(t^* = 59.7$ and $t^* = 174.9$, respectively). The fourth time step $(t^* = 98.1)$ is selected when the SV reaches its maximum radial location, and the fifth time step $(t^* = 156.4)$ when the SV core center is aligned vertically on top of that of PV during the SV orbiting of the PV.

Figure 4.2 shows snapshots at the selected time steps of different quantities in the PV frame of reference in the radial direction only; i.e. the origin of the radial coordinate coincides with the PV core center, while the origin of the wall-normal direction remains at the wall. Each snapshot consists of three subplots, the velocity vector field superposed onto the vorticity field (top), the near-wall temperature field $\theta = (T - T_w)/(T_\infty - T_w)$ (middle) and the radial distribution of the

local Nusselt number Nu_r (bottom). Snapshots for each time step from both cases are displayed side by side to facilitate comparison as time progresses.

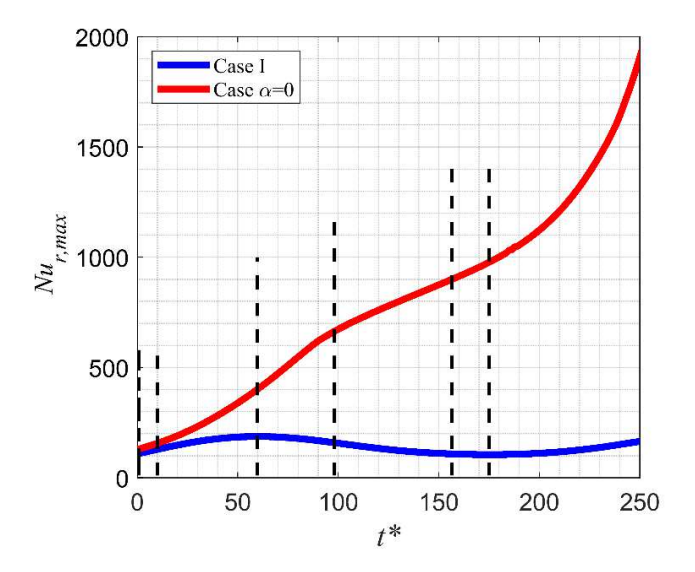


Figure 4.1 Evolution of $Nu_{r,max}$ with time for Case I and Case $\alpha = 0$. The vertical black broken lines represent the selected time steps that are used for comparison between the two cases.

The flow field evolution for both cases should be identical to that described in Section 3.2 for Case I. For both cases, Figure 4.2a and 4.2b show that as the TBL starts to deform, the $Nu_{r,max}$ is seen on the "downwash" side of the vortex. From Chapter 3, it is already established that the TBL is thinnest at the location of $Nu_{r,max}$. Interestingly, this is not the case for Case $\alpha=0$, where $Nu_{r,max}$ is found at a larger radial offset from the PV core center than that of the minimum TBL. This radial offset between the minimum TBL thickness and $Nu_{r,max}$ when $\alpha=0$ is seen more clearly at later time instants (Figure 4.2c through 4.2d). These time instants occur as the BL separates leading to the formation of the SV, and the SV and the PV mutually interact, causing the "rebound" of the PV. Figure 4.3 demonstrates quantitatively the difference in the radial location of $Nu_{r,max}$ with and without thermal diffusivity. As seen from the figure, the radial location of the

Case $\alpha = 0$ is shifted farther away from the PV core center in comparison with Case I for the entire history of evolution.

Figure 4.2c through 4.2f show that the TBL thickness (δ_{th}) on the "downwash" side for Case $\alpha = 0$ keeps thinning, increasing the wall-normal temperature gradient, even after the PV moves away from the wall. This monotonic thinning with time produces a significantly higher $Nu_{r,max}$ when $\alpha=0$ in comparison to Case I. This is distinctly different from Case I, where the presence of thermal diffusivity clearly prohibits such excessive thinning of the TBL. These observations imply that thermal diffusivity plays an important role in balancing the intensification of the temperature gradient (and hence limiting the heat transfer enhancement) due to downward advection by the induced velocity of the PV. This also implies that for a vortex with the same core radius; a higher Prandtl-Reynolds number product (expressing the relative importance of flow convective to thermal diffusion effects: $Pr \times Re = \frac{v}{\alpha} \frac{\Gamma_o}{v} = \frac{\Gamma_o}{\alpha}$) should produce higher $Nu_{r,max}$. This statement can be generalized by using the induced axial velocity u_z instead of Γ_o (i.e. $r \times$ $Re \propto \frac{u_z}{\alpha}$). A 1D heated-plate model problem with wall-normal velocity perturbation will be discussed (in Section 4.1.3) to examine the interplay between the downward velocity component and thermal diffusion, and how this interplay affects the unsteady behavior of the temperature field and the wall-normal temperature gradient.

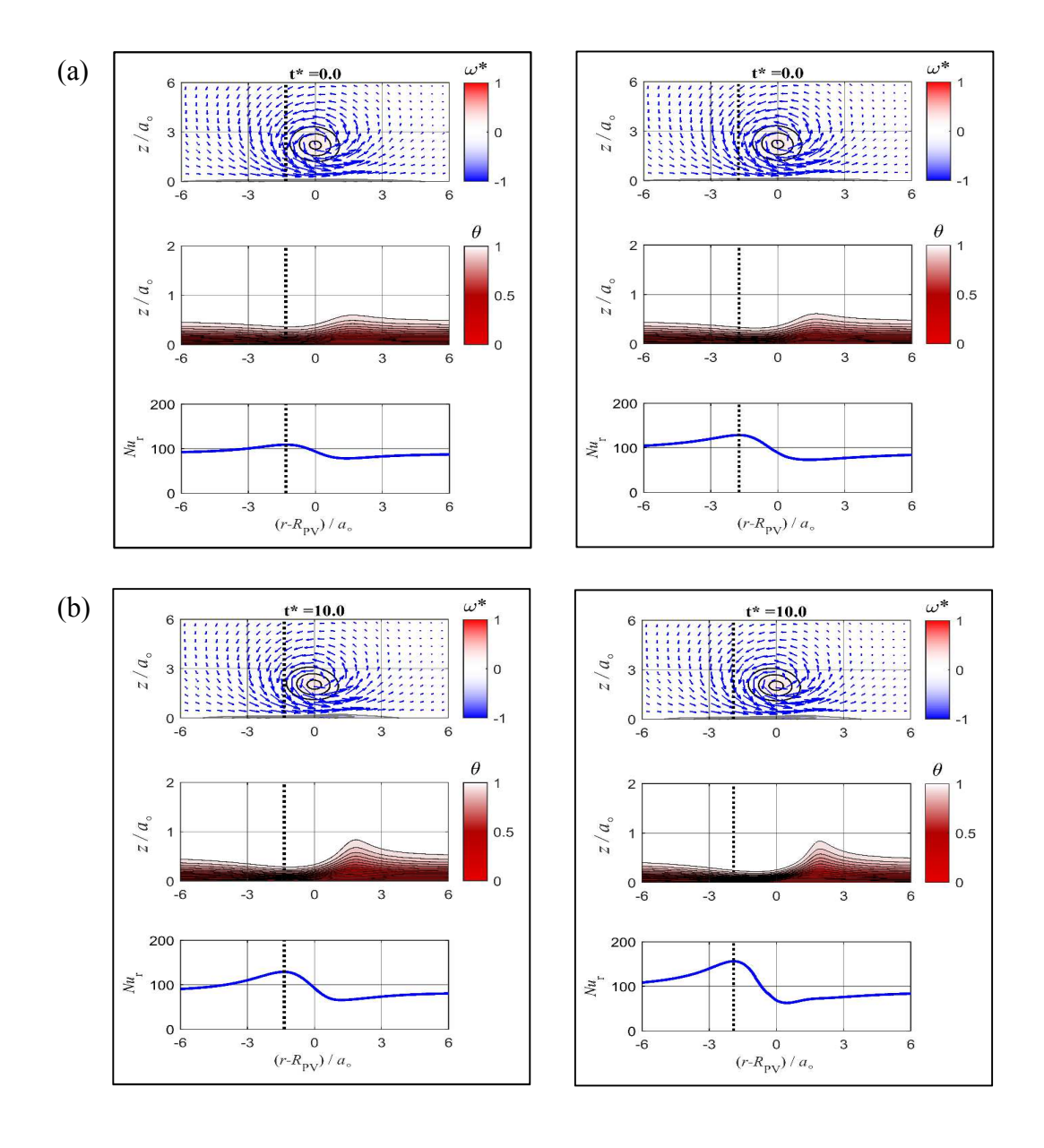


Figure 4.2 Time evolution of the initially-Gaussian-core vortex ring as it interacts with a heated wall: left (Case I) and right (Case $\alpha = 0$). Shown at each time instant: the azimuthal-vorticity field and velocity-field vectors (top), the near-wall temperature field (middle) and a line plot (bottom) of Nusselt number (Nu_r). The broken black line depicts the location of the maximum Nu_r . In snapshots c through f, $Nu_{r,max}$ for $\alpha = 0$ (right column) is scaled before plotting to fit in a similar plot window as shown in the left column. The scaling factor is included in the axis label.

Figure 4.2 (cont'd)

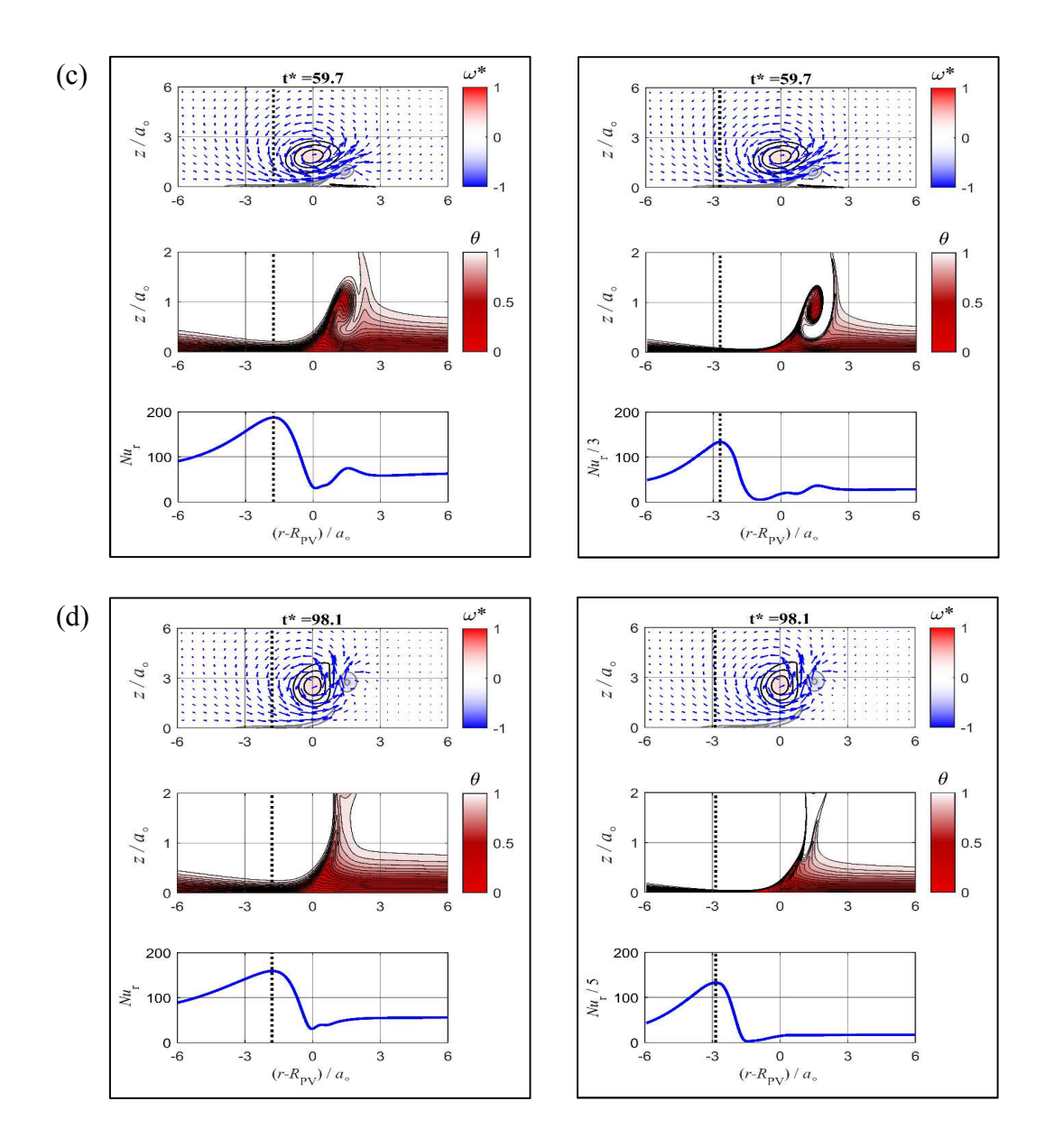
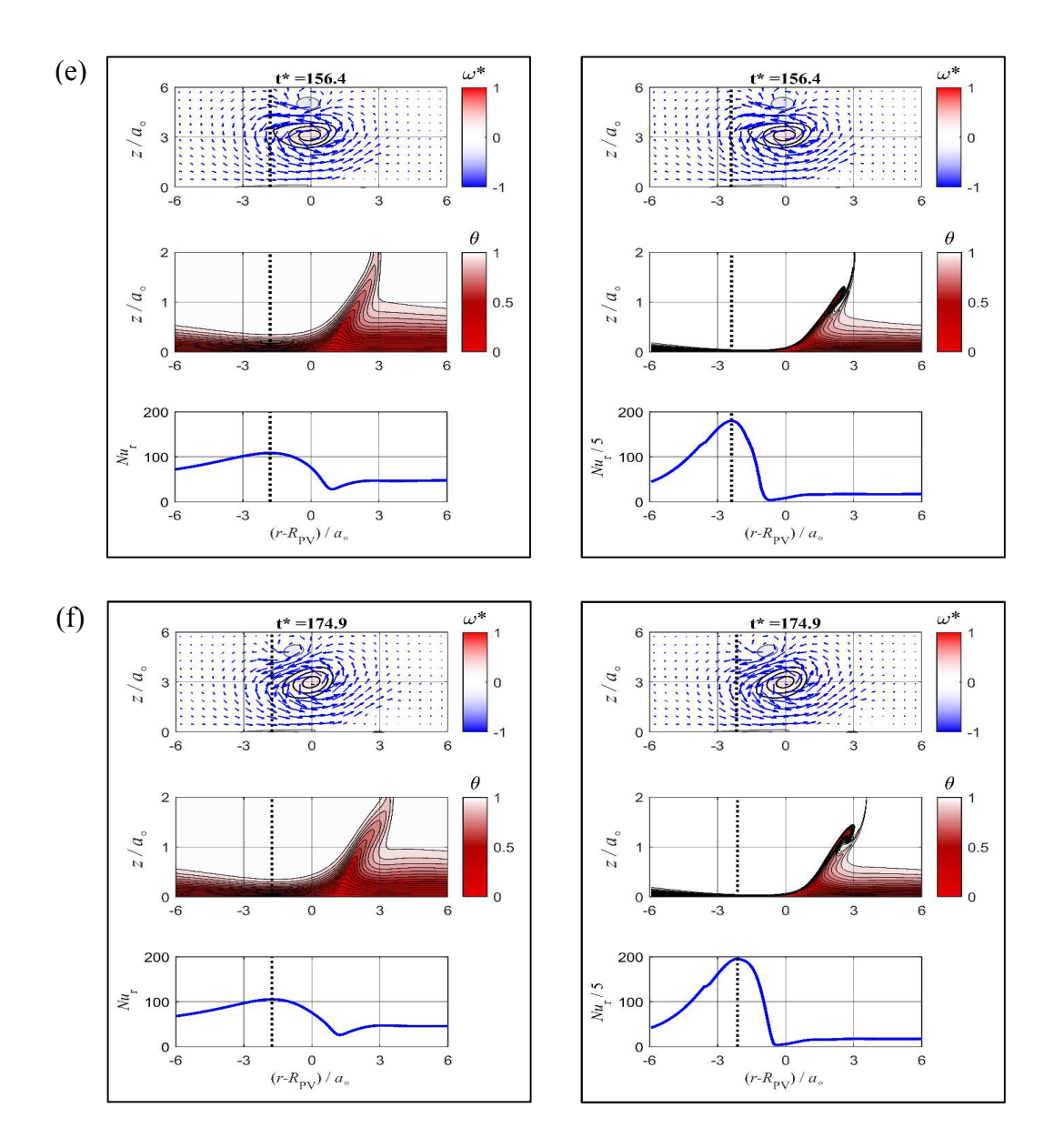


Figure 4.2 (cont'd)



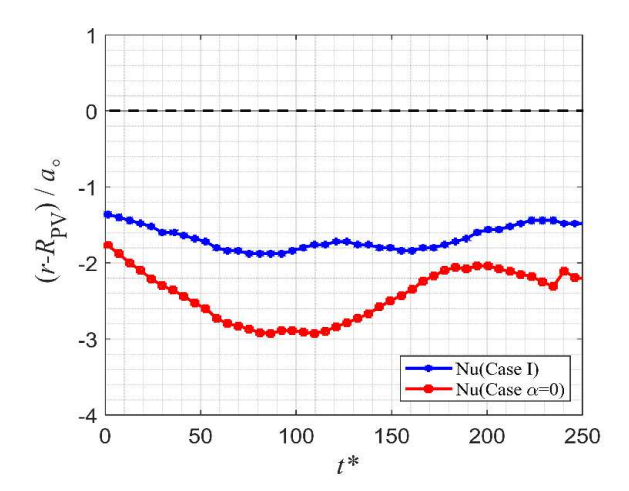


Figure 4.3 Temporal evolution of the radial location of the maximum local Nusselt number for Case I and Case α =0.

Figure 4.4a shows the correlation between the magnitude of $Nu_{r,max}$ for Case I and Case $\alpha=0$, on one hand, and the *wall-normal* location of the PV core center (Z_{PV}) , on the other. Unlike Case I, which shows some correlation between the proximity of the PV to the wall and $Nu_{r,max}$, Case $\alpha=0$ shows initially a correlation between the PV and $Nu_{r,max}$ (with the latter increasing as the PV approaches the wall, similar to Case I), but as time progresses $Nu_{r,max}$ keeps increasing irrespective of the height of the PV above the wall (because of the continued thinning of the TBL seen in Figure 4.2). For Case I, the correlation between Z_{PV} and the Nusselt number is hypothesized to be as follows: when the PV approaches the wall between $t^*=0$ and 50, the downwash velocity (u_z) becomes stronger, causing the TBL to be thinner and the Nusselt number to increase. The opposite occurs as the PV moves away from the wall, and subsequent modulation in the PV height results in modulation of u_z and a corresponding modulation in $Nu_{r,max}$. The lack of similar modulation of $Nu_{r,max}$ when $\alpha=0$ is surprising because, in the absence of thermal diffusivity, the temperature field can only evolve via advection, which, on the downwash side, is

connected directly to the evolution of the PV. However, upon closer inspection, it is found that a correlation does indeed exist between Z_{PV} and the time rate of change of $Nu_{r,max}$ when $\alpha=0$. This can be seen in Figure 4.4b, where the slope of the Case $\alpha=0$ plot in Figure 4.4a is shown together with the PV height evolution. As seen from the figure, modulation in Z_{PV} does indeed produce a corresponding modulation in the $d(Nu_{r,max})/dt^*$. The underlying physics causing the correlation of the vortex height (and hence, by hypothesis, downwash velocity) with the Nusselt number, when $\alpha \neq 0$, and with its rate of change, when $\alpha=0$, will be clarified using a simple analytical problem in Section 4.1.3.

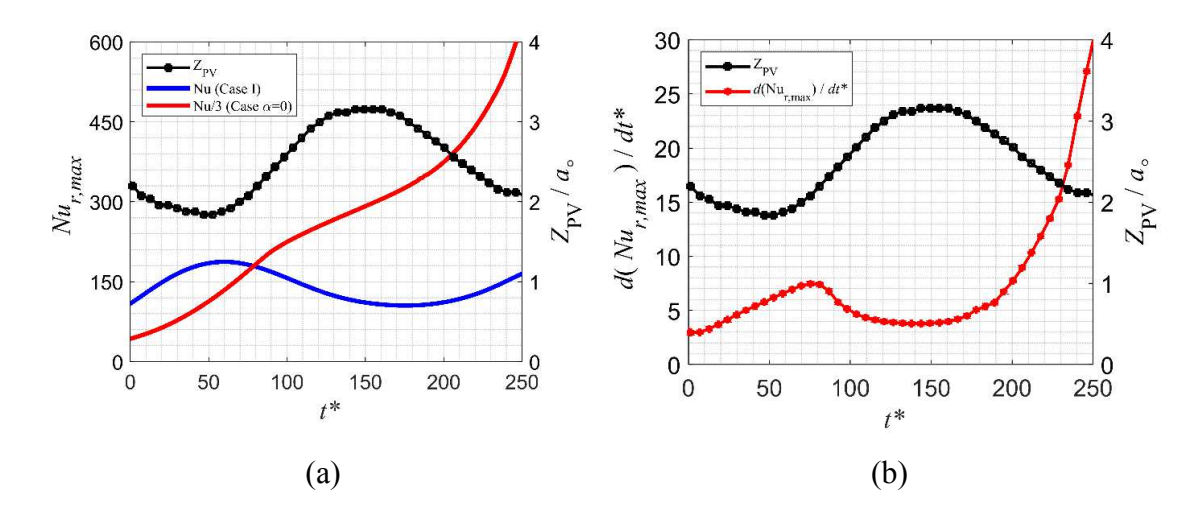


Figure 4.4 a) Temporal evolution of $Nu_{r,max}$, for Case I and Case $\alpha = 0$, and the wall-normal location of the core center of the PV. For Case $\alpha = 0$, $Nu_{r,max}$ is divided by a factor of 3 to fit on the same plot with Case I. b) The temporal evolution of the rate of change of $Nu_{r,max}$ for Case $\alpha = 0$, and the wall-normal location of the core center of the PV.

4.1.2. Thermal Boundary Layer Profiles and Nusselt Number Based on TBL Thickness

Based on the above discussion, for Case I, the enhancement of Nusselt number as exemplified by $Nu_{r,max}$ is a direct consequence of thermal boundary layer thinning via the axial

downwash velocity, and the modulation of $Nu_{r,max}$ is caused by changes in the TBL thickness (δ_{th}) , produced by the interplay of the time-varying axial downwash velocity and thermal diffusion. The correlation between the enhancement of heat transfer and local thinning of TBL is further investigated by examining the TBL temperature profile and using δ_{th} as a length scale. These profiles are shown in Figure 4.5 for the time steps identified in Figure 4.1, and at the radial location of $Nu_{r,max}$. Figure 4.5a and 4.5b show the results for Case I and Case $\alpha=0$ respectively, along with the unsteady diffusion solution, used to initialize the temperature field, for reference.

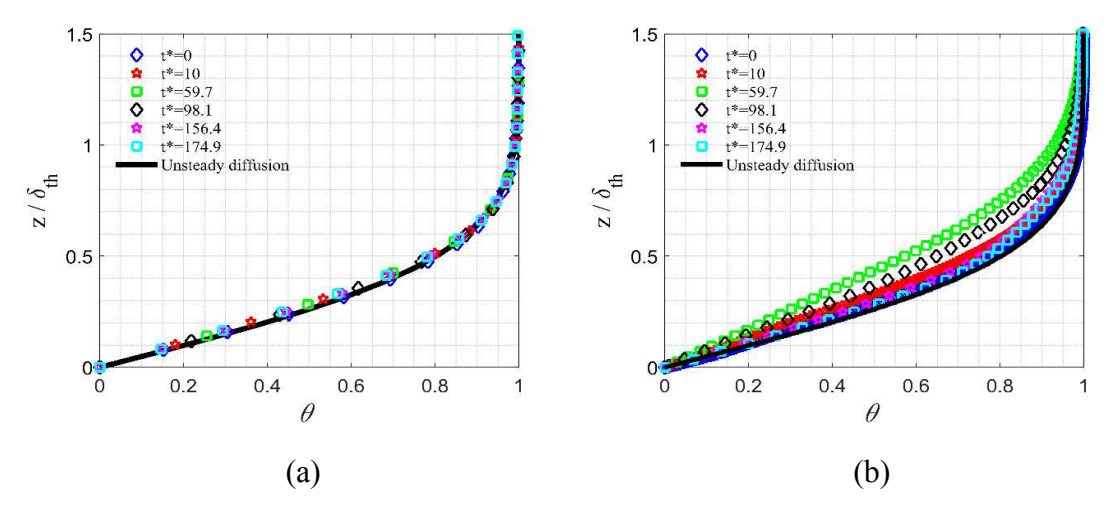


Figure 4.5 Normalized temperature profiles versus the axial coordinate scaled with δ_{th} : a) Case I, and; b) Case $\alpha = 0$. The solid black curve represents the unsteady diffusion solution normalized in the same manner as the other profiles. The temperature profiles chosen at the radial location of $Nu_{r,max}$ for different time steps.

Considering Figure 4.5a, the temperature profiles at the different time instants collapse on one another as well as on the unsteady diffusion solution, as if the temperature field evolution is self-similar. The implication of this collapse is that the TBL temperature profile shape remains invariant from its initial unsteady-diffusion form. Consequently, the net influence of the PV on the TBL is to modulate its thickness, which implies that the variation in $Nu_{r,max}$ is indeed a

consequence of boundary layer thinning as hypothesized in the literature. This connection can be made explicit in the present case as outlined below.

Based on the collapse in Figure 4.5a, it is concluded that the non-dimensional temperature gradient at the wall remains invariant at the location of the maximum Nusselt number; i.e.

$$\left. \frac{\partial \theta}{\partial (\frac{z}{\delta th})} \right|_{z=0} \approx C \tag{4.1}$$

where C is a constant. Since the Nusselt number is essentially the non-dimensional temperature gradient at the wall, Equation 4.1 shows that if the TBL thickness is used as the length scale in calculating the $Nu_{r,max}$, then the value of the latter will remain constant during the PV evolution. This can be seen by plotting the evolution of $Nu_{r,max}$ when scaled with δ_{th} . Figure 4.6 shows this plot for both Case I and Case $\alpha=0$, in comparison with the theoretical value obtained from the semi-infinite unsteady diffusion solution (Equation 2.9). The latter is found by setting $\frac{T(t,z)-T_w}{T_{\infty}-T_w}=0.99$ in Equation 2.9 to find $\delta_{th}/2\sqrt{\alpha t}=1.825$. Substituting for $2\sqrt{\alpha t}$ from the last equation in Equation 2.9, yields,

$$\theta = \frac{T(t,z) - T_w}{T_{\infty} - T_W} = erf \ (1.825 \ \eta) \tag{4.2}$$

$$\frac{d\theta}{d(\frac{z}{\delta_{th}})} = \frac{2}{\sqrt{\pi}} \times 1.825 \, e^{-1.825\eta^2} \tag{4.3}$$

where $\eta = \frac{z}{\delta_{th}}$. Taking the derivative of Equation 4.2 with respect to η and evaluating at the wall $(\eta = 0)$,

$$\left. \frac{d\theta}{d(\frac{z}{\delta_{th}})} \right|_{\eta=0} = 2.05 \tag{4.4}$$

Figure 4.6 shows that for Case I, the Nusselt number is practically constant when normalized by the TBL thickness, and it has a value that is close to that of the initial TBL. This approximate scaling of the Nusselt number with δ_{th} implies that the *wall-normal* temperature gradient is inversely proportional to the local δ_{th} , and the latter is the only significant parameter affecting the heat transfer enhancement. Specifically,

$$Nu_{r,max}^* = \delta t h \frac{\partial \theta}{\partial z} \Big|_{z=0} \approx C$$
 (4.5)

where $Nu_{r,max}^*$ is the maximum Nusselt number scaled with δ_{th} . Equation 4.5 leads to

$$\left. \frac{\partial \theta}{\partial z} \right|_{z=0} \propto \frac{1}{\delta th}$$
 (4.6)

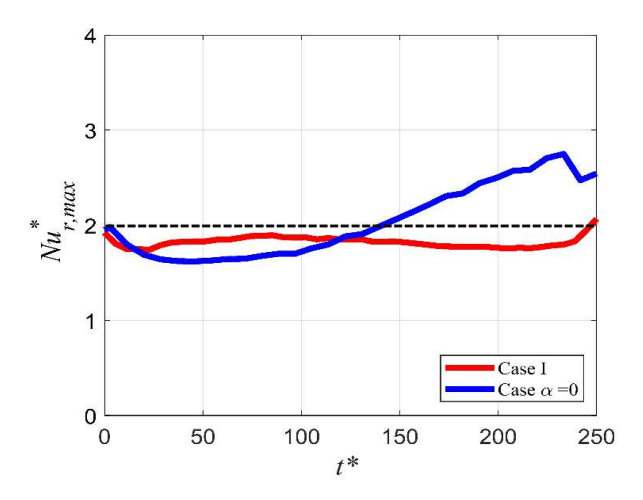


Figure 4.6 Evolution of $Nu_{r,max}$, scaled with δ_{th} , for Case I and Case $\alpha = 0$. The broken black line represents the unsteady-diffusion theoretical value obtained from Equation 4.4.

Therefore, by plotting $Nu_{r,max}$ (scaled with constant length scale L_o ; see Equation 3.3) as it evolves with time, together with the $\delta_{th,min}$ evolution (Figure 4.7a) for Case I, $Nu_{r,max}$ is observed to be "180 degree" out of phase with $\delta_{th,min}$.

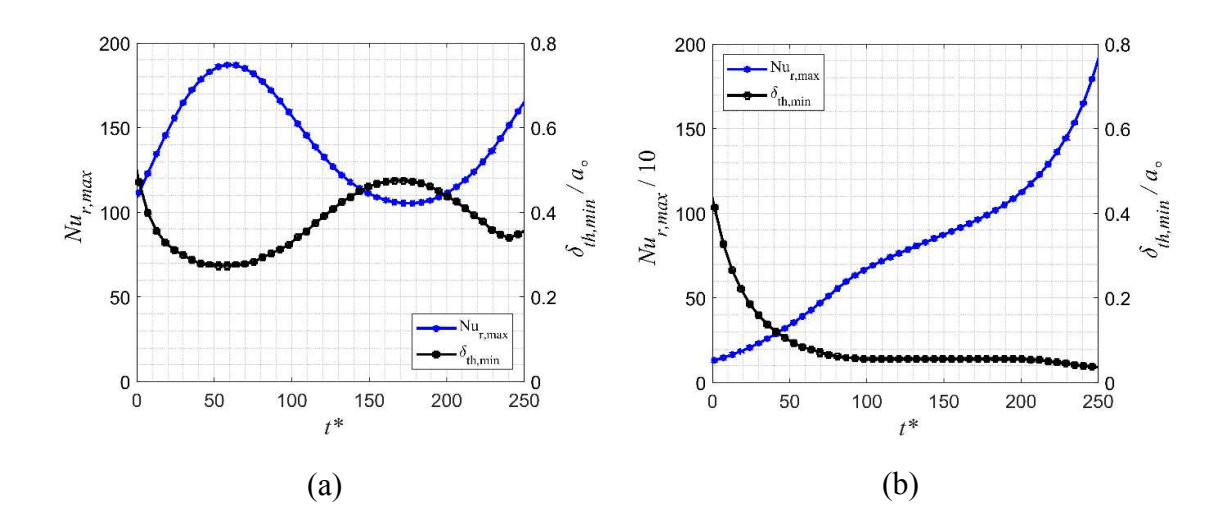


Figure 4.7 Evolution of $Nu_{r,max}$ and minimum thickness of TBL ($\delta_{th,min}$); a) Case I; and b) Case α =0.

For Case $\alpha=0$, Figure 4.5b shows that the TBL temperature profiles do not collapse at all times. Thus, it is not possible to conclude that the $Nu_{r,max}$ variation is only due to variation in the overall thickness of the TBL. This is consistent with the observations made earlier from Figure 4.2, where the radial location of $Nu_{r,max}$ did not coincide with that of the minimum δ_{th} . Moreover, an inspection of the evolution of the $Nu_{r,max}$ and δ_{th} in Figure 4.7b shows that although there is a correlation at the start and end of the evolution, where the $Nu_{r,max}$ increases as the minimum δ_{th} decreases, between $t^*=100$ and 200, the minimum δ_{th} reaches a plateau, yet the $Nu_{r,max}$ continues to increase. This implies that in the absence of thermal diffusivity, the variation in the heat transfer enhancement is not a simple direct effect of the change in the TBL thickness as in Case I. This idea is also reflected in Figure 4.6b, where the Nusselt number based on δ_{th} exhibits

significant variation with time for Case $\alpha = 0$, in comparison to Case I. A better understanding of the differences between these two cases is sought using a simple analytical model in the following section.

4.1.3. Analytical Model

A suitable model problem that represents the downwash-side heat transfer during the vortex-wall interaction should exhibit competition between advection effects of the wall-normal velocity and thermal diffusion in establishing the thermal boundary layer. It is also necessary to impose unsteadiness on this problem via time variation in order to understand how the speed of variation influences the "dynamic response" of the temperature field and the wall heat transfer. The problem should also be simple, ideally having an analytical solution that can be used for examining the unsteady thermal boundary layer behavior.

A model problem that incorporates the above elements was formulated. Figure 4.8 shows a sketch of this problem, where the fluid is sucked through a constant-temperature heated wall with uniform but unsteady wall-normal suction velocity $-v_o(t)$.

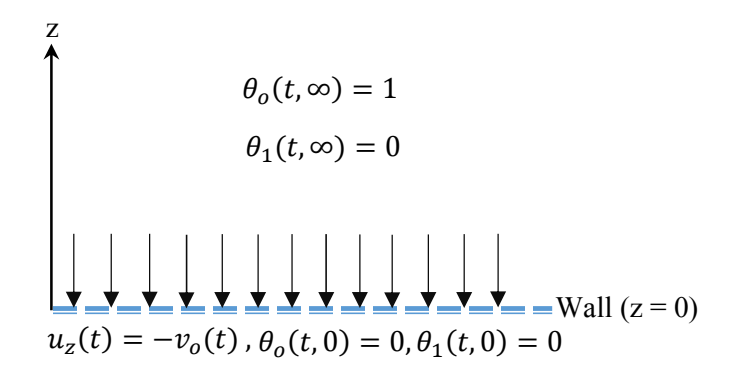


Figure 4.8 Sketch of the problem of one-dimensional thermal boundary layer with uniform suction.

To solve this problem, we first consider the case of constant (steady) suction. The energy equation for this steady, one-dimensional temperature field is given by:

$$-v_o \frac{d\theta_o}{dz} = \alpha \frac{d^2\theta_o}{dz^2} \tag{4.7}$$

where $\theta_o(z) = \frac{T(z) - T_W}{T_\infty - T_W}$, v_o is the magnitude of the axial suction velocity, subscript (o) denotes steady quantities, and α is the thermal diffusivity. Equation 4.7 is subject to the boundary conditions: $(z = 0, \theta_o = 0)$ and $(z \to \infty, \theta_o \to 1)$. This problem formulation is exactly analogous to the asymptotic hydrodynamic boundary layer with constant suction velocity (Schlichting [34]), where the streamwise velocity is the analog of θ_o . The solution is straightforward and is given by,

$$\theta_o = 1 - e^{\frac{-v_o}{\alpha}z} \tag{4.8}$$

Based on Equation 4.8, one can deduce that the steady response of the temperature field depends on the balance between the downward velocity magnitude (advection) and the upward diffusive heat transfer. Specifically, the 99% TBL thickness is calculated by setting $\theta_o = 0.99$ in Equation 4.8, leading to $\delta_{tho} = 4.6052 \frac{\alpha}{v_o}$. Increasing α results in a thicker TBL, while increasing v_o does the opposite. The length scale $(l_o = \frac{\alpha}{v_o})$ is proportional to the boundary layer thickness and will be used later for non-dimensionalization of quantities.

Moving to the unsteady version of the above problem, the unsteady form of Equation 4.8 is:

$$\frac{\partial \theta}{\partial t} + u_z(t) \frac{\partial \theta}{\partial z} = \alpha \frac{\partial^2 \theta}{\partial z^2} \tag{4.9}$$

To solve Equation 4.9, we use the method of asymptotic expansion, exemplified in Schlichting [34] in solving the unsteady boundary layer problem beneath a freestream with small harmonic perturbation (which had been studied extensively by Lighthill [35], Stuart [36] and Watson [37]). Specifically, the unsteadiness is produced by superposing a complex harmonic perturbation on the steady velocity field, resulting in the form:

$$u_z(t) = -v_o(1 + \varepsilon e^{i\omega t}) \tag{4.10}$$

where (ε) denotes a very small number and (ω) and (t) are the angular frequency and time respectively. Equation 4.10 is the result of truncating an infinite power series of the perturbation parameter (ε) to only include the first order term. As such, the solution obtained here is only applicable for small-amplitude variation in u_z . It follows that the solution of Equation 4.9 is assumed to have the form,

$$\theta(z,t) = \theta_o(z) + \varepsilon \,\theta_1(z) \,e^{i\omega t} \tag{4.11}$$

The solution of Equations 4.9 through 4.11 is given in Appendix C. The unsteady part of the temperature solution is given by:

$$\Theta_1(\widehat{\omega}, z^*, t^*) = R\{\theta_1(\widehat{\omega}, z^*)e^{i\widehat{\omega}t^*}\}$$
(4.12)

where, R denotes the real part of the bracketed quantity, and $(\widehat{\omega} = \frac{4\omega l_0^2}{\alpha})$ and $(t^* = \frac{\alpha t}{4l_0^2})$ are the normalized angular frequency and time respectively. The final solution becomes:

$$\Theta_1 = \mathcal{A}(\widehat{\omega}, z^*) \cos(\widehat{\omega}t^* - \Phi(\widehat{\omega}, z^*))$$
 (4.13)

where $(z^* = \frac{z}{4l_o})$ is the normalized axial coordinate, and $\mathcal{A}(\widehat{\omega}, z^*)$ and $\Phi(\widehat{\omega}, z^*)$ are the amplitude and the phase delay of the temperature field respectively, which are given by:

$$\mathcal{A}(\widehat{\omega}, z^*) = \sqrt{A(\widehat{\omega}, z^*)^2 + B(\widehat{\omega}, z^*)^2}$$
(4.14)

$$\Phi(\widehat{\omega}, z^*) = tan^{-1} \left(\frac{A(\widehat{\omega}, z^*)}{B(\widehat{\omega}, z^*)} \right)$$
 (4.15)

$$A(\widehat{\omega}, z^*) = \frac{4}{\widehat{\omega}} \left[e^{-4z^*} - e^{-2(\Omega^* + 1)z^*} \cos\left(\frac{\widehat{\omega}}{\Omega^*} z^*\right) \right]$$
(4.16)

$$B(\widehat{\omega}, z^*) = \frac{4}{\widehat{\omega}} e^{-2(\Omega^* + 1)z^*} \sin\left(\frac{\widehat{\omega}}{\Omega^*} z^*\right)$$
(4.17)

and (
$$\Omega^* = \sqrt{\frac{1+\sqrt{1+(\widehat{\omega})^2}}{2}}$$
).

The temperature gradient at the wall for the unsteady part is obtained by taking the derivative of Equation 4.13 with respect to z^* , setting $z^* = 0$. The result can be again in terms of cosine function of time, as given below:

$$\frac{d\theta_1}{dz^*}\Big|_{z^*=0} = \tilde{\mathcal{A}}(\widehat{\omega})\cos\left(\widehat{\omega}t^* - \tilde{\Phi}(\widehat{\omega})\right) \tag{4.18}$$

where,

$$\tilde{\mathcal{A}}(\widehat{\omega}) = \sqrt{C(\widehat{\omega})^2 + D(\widehat{\omega})^2} \tag{4.19}$$

$$\widetilde{\Phi}(\widehat{\omega}) = tan^{-1} \left(\frac{C(\widehat{\omega})}{D(\widehat{\omega})} \right) \tag{4.20}$$

$$C(\widehat{\omega}) = \left[\frac{-16}{\widehat{\omega}} + \frac{8(\Omega^* + 1)}{\widehat{\omega}} \right] \tag{4.21}$$

$$D(\widehat{\omega}) = \frac{4}{\Omega^*} \tag{4.22}$$

where $\tilde{\mathcal{A}}(\hat{\omega})$ and $\tilde{\Phi}(\hat{\omega})$ are the amplitude and the phase delay of $\frac{d\theta_1}{dz^*}\Big|_{z^*=0}$ respectively.

Plots of the amplitude and the phase response of the wall temperature gradient are shown in Figure 4.9. The results show increasing attenuation and phase delay of the unsteady wall heat with increasing frequency. This implies that at low normalized frequency, the response of the temperature gradient is in phase with the suction velocity, and the problem will become quasisteady heat transfer with suction. Specifically, using the steady state solution, Equation 4.8, when the unsteady suction velocity is maximum in the oscillation cycle, the boundary layer thickness will be thinnest and the temperature gradient at the wall will be highest, and vice versa. At the opposite end of the spectrum, as $\hat{\omega}$ tends to infinity, the temperature-gradient's lag *w.r.t.* the suction velocity asymptotes to 45° .

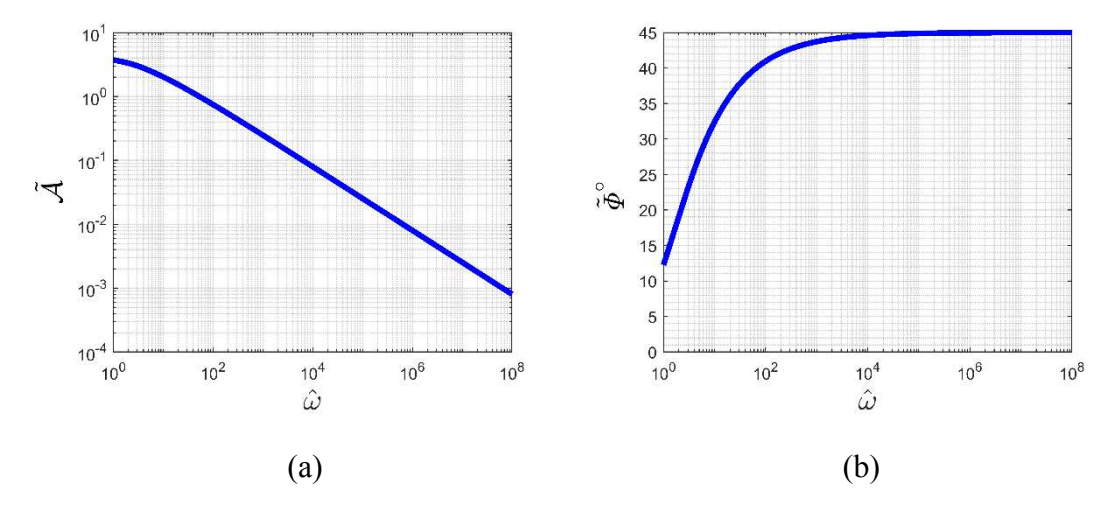


Figure 4.9 a) Amplitude, and b) phase shift response of the unsteady temperature gradient at the wall due to harmonic variation in the suction velocity in the form $-v_o\cos(\hat{\omega}t^*)$.

The above behavior is qualitatively consistent with known diffusion physics. Specifically, at very small $\widehat{\omega}=4\omega l_o^2/\alpha$, the oscillation period is sufficiently long and/or the diffusivity is sufficiently high that a change in the temperature field due to flow variation can diffuse over a domain size $\sqrt{\frac{\alpha}{4\omega}}$, that is much larger than the characteristic length of the temperature field l_o . Accordingly, the temperature field adapts to the changing suction velocity as if the field is steady and subjected to a suction velocity having a magnitude equal to the instantaneous value of $u_z(t)$; i.e. quasi-steady response. As the frequency increases, the cycle time decreases, and the diffusion length becomes shorter and the adaptation to $u_z(t)$ lags behind and becomes attenuated. Based on this, ω^* is effectively the square of the ratio of a characteristic length of the TBL to the diffusion length. Thicker TBL leads to larger $\widehat{\omega}$, and slower TBL response and vice versa.

The results from the simple, linearized model problem are intended to help grasp the leading-order physics affecting the interplay of wall-normal advection and thermal diffusion. This

understanding is now used in interpreting observations related to Nusselt number enhancement in vortex-wall interaction at a *fixed* radial location. In Figure 4.10, the normalized radial location $((r - R_o)/a_o \approx 1)$ of the maximum of $Nu_{r,max}$ of Case I (which occurs at $t^* = 59.7$; see Figure 3.4c and Figure 4.1, noting that R_o is a the initial core radius of PV and not the instantaneous) was chosen to follow the history of Nu and the wall-normal velocity of the first node above the wall. The same is done for Case $\alpha = 0$, but in order to get a fair comparison for both Case I and Case $\alpha = 0$, the same radial location is used for both cases to ensure that the wall-normal velocity history is the same. The history $u_z^*(t)$ is plotted after multiplying by -1, which makes it easier to visualize the correlation between Nu_r and the wall-normal velocity.

In analyzing Figure 4.10, we focus on the period where the wall-normal velocity is towards the wall $(-u_z^* > 0)$, so it is acting in opposition to thermal diffusion as in the model problem. As seen from the figure, the velocity is initially away from the wall then it switches sign at approximately $t^* = 40$, and stays towards the wall for the remainder of the time. For $t^* > 40$, the shape of $-u_z^*(t)$ is very similar to Nu(t), supporting the idea that the wall-normal velocity is directly impacting the change in Nu. Early in the time window $t^* > 40$, when Nu increases to a peak then decreases, $-u_z^*(t)$ and Nu(t) appear in phase with both of them reaching their peak simultaneously. Later in time, as both quantities reach an approximate plateau, the small modulation in Nu(t) lags the corresponding modulation in $-u_z^*(t)$.

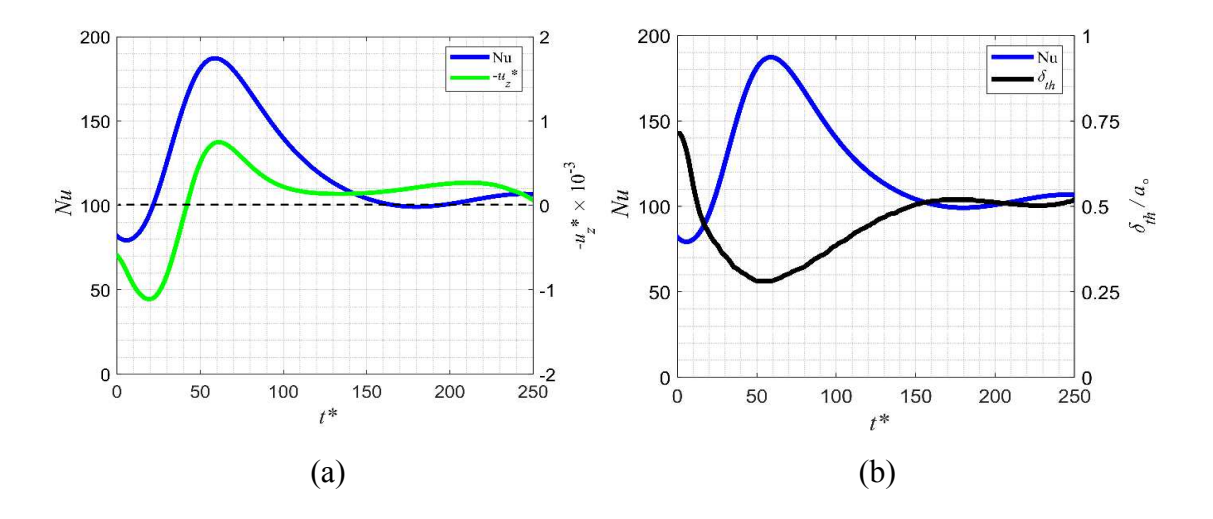


Figure 4.10 a) Evolution of Nu and the normalized axial velocity of the first node above the wall, and; b) Evolution of Nu and the TBL thickness, at $(r - R_o)/a_o \approx 1$, where the maximum of $Nu_{r,max}$ of Case I occurs. The black broken line in (a) shows the zero value of u_z^* .

Per the 1D model physics, the observations in Figure 4.10, indicate fast temperature field response initially (i.e. quasi-steady or corresponding to low $\widehat{\omega}$, which become progressively slower (corresponding to high $\widehat{\omega}$). This idea would be consistent with a smaller characteristic length l_o early in the $t^* > 40$ period, and a larger one towards the end. Indeed, as seen from Figure 4.10b, the TBL thickness is initially one half that at the end of the period. In fact, the shape of the TBL thickness history is "mirror image" of that of Nu(t), showing the correlation between TBL thinning and Nu enhancement. This direct correlation is further emphasized with the collapse of the normalized temperature profiles at the radial location considered in Figure 4.11 when using the TBL thickness to normalize z.

Thus, in summary, the shape similarity of $-u_z^*(t)$ and Nu(t), and the dynamic behavior of both quantities in a manner that is qualitatively consistent with the findings of the 1D model indicate that the downwash velocity is probably the most significant factor affecting the temporal evolution of Nu on the downwash side of the PV. The effect is directly related to the change in the TBL thickness in response to variation in the downwash velocity of the PV as it interacts with the wall.

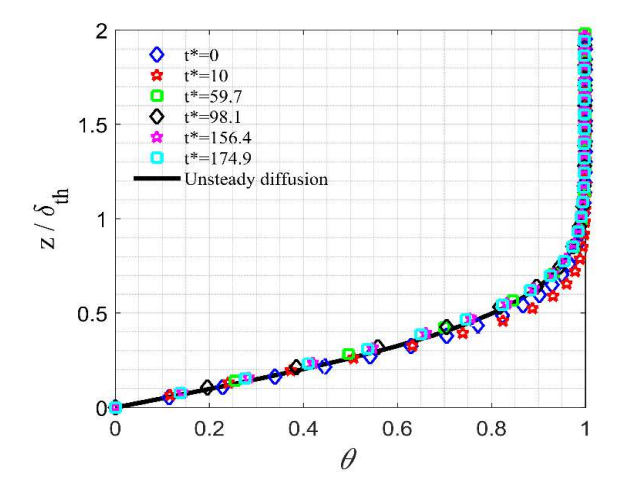


Figure 4.11 Normalized temperature profiles versus the axial coordinate scaled with δ_{th} at $(r - R_o)/a_o \approx 1$, the same radial location considered in Figure 4.10, for Case I. The solid black curve represents the unsteady diffusion solution normalized in the same manner as the other profiles.

An interesting aspect of the result in Figure 4.10 for the time period when the wall-normal velocity is away from the wall (i.e. for $t^* < 40$) is that even though the $u_z^*(t) > 0$, the boundary layer is thinning and the Nu is increasing. In this case, it is evident that the boundary layer thinning is not caused by the wall normal velocity, which if anything should make the TBL thicker. The switch in the sign of $u_z^*(t)$ in Figure 4.10 indicates that the point of observation is initially located on the upwash side of the PV then it switches to the downwash side at $t^* \approx 40$. Inspection of the temporal evolution of the flow and temperature fields shows that this switch occurs when the PV

advects radially outwards past the given position at the wall. As the PV does so, the thinned TBL on the downwash side of the PV is advected past the fixed point on the wall, causing TBL thinning, and *Nu* enhancement, while the point remains on the upwash side of the vortex. This "special case" of enhancement is associated with radial rather than wall-normal advection. Illustrative flow and temperature field snapshots for the case considered in Figure 4.10 are shown in Figure 4.12 to demonstrate the behavior just described. Note that the plots shown on top represent time instants when the radial location of concern is on the upwash side, the bottom left plot when beneath the center of the PV, and the bottom right plot when on the downwash side.

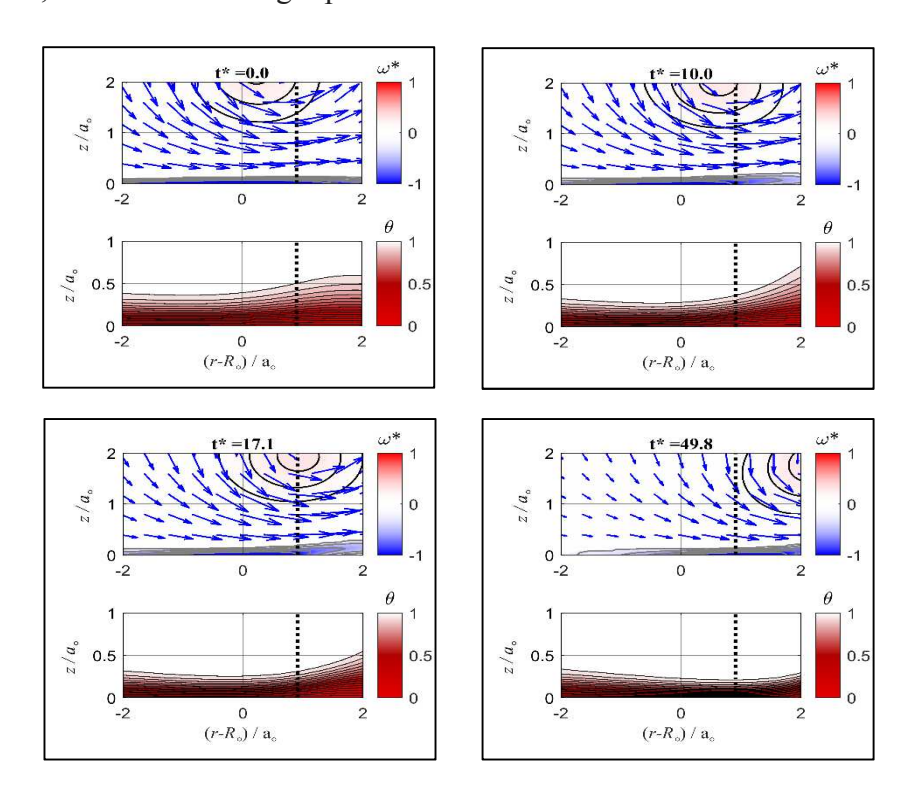


Figure 4.12 Time evolution of the initially-Gaussian-core vortex ring as it interacts with a heated wall (Case I) in the original Eulerian frame of reference (as in Chapter 3). Shown at each time instant: the azimuthal-vorticity field and velocity-field vectors (top) and the near-wall temperature field (bottom). The broken black line depicts the location of the maximum of $Nu_{r,max}$ at $((r - R_o)/a_o \approx 1)$.

Considering the same analysis of Figure 4.10 in Case $\alpha=0$, Figure 4.13a displays the temporal variation of $-u_z^*(t)$ and Nu at the same radial location considered in Figure 4.10 (i.e. where the $u_z^*(t)$ history at the first node above the wall is identical to its counterpart for Case I). As was the case in Figure 4.4a, where no correlation between the PV height above the wall with $Nu_{r,max}$ was obvious when $\alpha=0$, Figure 4.13a also shows no obvious similarity in the shape of $-u_z^*(t)$ and Nu at $((r-R_o)/a_o\approx 1)$ (as for example is the case in Figure 4.10a. This implies that the physical connection between $u_z^*(t)$ and Nu is different in Case $\alpha=0$, in comparison to Case I.

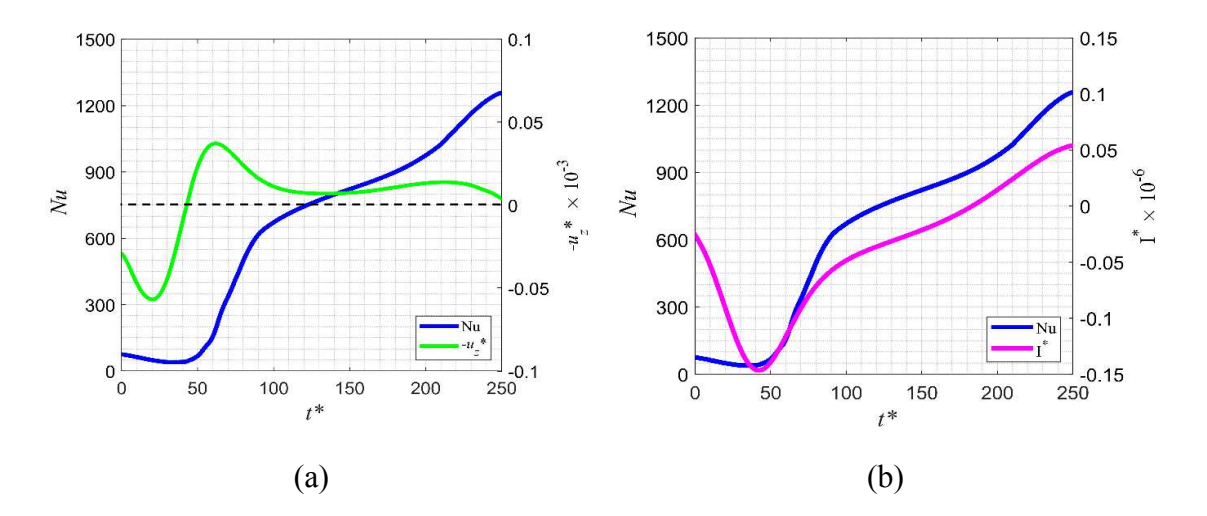


Figure 4.13 a) the evolution of Nu and the normalized axial velocity of the first node above the wall, and b) the evolution of Nu and $I^* = \int_0^t -u_z^*(t)dt$, at $((r - R_o)/a_o \approx 1)$ for Case $\alpha = 0$.

To explore the wall-normal-velocity connection with the Nusselt number in the absence of thermal diffusivity, we set $\alpha = 0$ in Equation 4.9, leading to:

$$\frac{\partial \theta}{\partial t} + u_z(t) \frac{\partial \theta}{\partial z} = 0 \tag{4.23}$$

If we assume a separation of variable type solution of Equation (4.23); i.e. $\theta = Z(z)T(t)$, it can be shown that the solution has the form:

$$\theta(z,t) = \theta(z,0)e^{\int_0^t -\frac{u_z(t)dt}{\delta_o}}$$
(4.24)

where, $\theta(z,0)$ is the initial temperature field, and δ_o is a characteristic length scale of the initial temperature field (e.g. TBL thickness). Assuming $\int_0^t u_z(t)dt \ll \delta_o$, and linearizing the exponential term of Equation 4.24 via truncation of Taylor's series:

$$\theta(z,t) = \theta(z,0)[1 + \int_{0}^{t} \left[-\frac{u_{z}(t)}{\delta_{o}} \right] dt]$$
(4.25)

and the unsteady temperature field can be written as,

$$\theta'(z,t) = \theta(z,t) - \theta(z,0) = \theta(z,0) \int_0^t \left[-\frac{u_z(t)}{\delta_o} \right] dt$$
 (4.26)

Taking the derivative of Equation 4.26 w.r.t. z, and setting z=0 at the wall, then the *fluctuating* temperature gradient at the wall is given by

$$\left. \frac{d\theta'}{dz} \right|_{z=0} (t) = \frac{d\theta}{dz} \Big|_{z=0} (0) \int_0^t \left[-\frac{u_z(t)}{\delta_o} \right] dt \tag{4.27}$$

Equation 4.27 shows that in the absence of thermal diffusivity, the wall temperature gradient, and hence Nu, is influenced by the entire history of $u_z(t)$, rather than being a damped/delayed response to the instantaneous u_z value when $\alpha \neq 0$. This reasoning is because the left hand side of Equation 4.23 represents the material derivative of the temperature of the fluid

particles. Hence, the equation indicates that the fluid particles travel with constant temperature as they approach the wall, leading to increasing the temperature gradient at the wall over time. With this insight from the simple 1D model, we reexamine, the results of Figure 4.13a but instead of comparing Nu with $-u_z^*(t)$, we compare Nu to $I^* = \int_0^t -u_z^*(t)dt$. The result of this comparison is shown in Figure 4.13b, where the similarity between the latter two quantities is evident. Equation 4.27 also implies that the time rate of change of the wall temperature gradient and Nu, should be proportional to the wall-normal velocity. This is consistent with the correlation identified earlier in Figure 4.4b between $dNu_{r,max}/dt$ and the PV height (which is correlated with the wall-normal velocity) when $\alpha = 0$. Furthermore, given the dependence of Nu at a given point on the entire history of $u_z^*(t)$ for Case $\alpha = 0$, in comparison to the instantaneous value of $u_z^*(t)$ under quasisteady conditions for Case I, it is not surprising that maximum Nu_r is not collocated with the instantaneous minimum δ_{th} for the former case (found from the inspection of Figure 4.2), as it is for the latter.

4.1.4. Minimum Nu_r : Case I and Case $\tau = 0$ Comparison

The time instants for the investigation of $Nu_{r,min}$ are set depending on the evolution of the location of $Nu_{r,min}$, shown in Figure 4.14a. The three regions in Figure 4.14a, which are marked I, II and III, represent the pre-separation (region I) and the post-separation (regions II and III) flow. The latter region is subdivided further into two periods: where the minimum Nusselt number is located on the upwash side (region II), versus when it lies directly beneath the PV core center (region III). The beginning of region III also approximately coincides with the formation of the SV. The time period beyond region III is not considered in this analysis because it corresponds to the formation of the tertiary vortex, and the same scenario of events will be repeated.

The three identified regions exhibit distinctly different normalized temperature profiles within the instantaneous TBL at the radial location of $Nu_{r,min}$. Figure 4.14b shows these profiles for two selected instances of time for each of the three regions. The figure also includes the unsteady semi-infinite diffusion profile for reference. As time progress, the profiles change in shape from that of unsteady diffusion, which does not have an inflection point (pre-separation; $t^* = 0$ and $t^* = 7.1$) to a profile with an inflection point (post-separation; $t^* = 21.3$, $t^* = 28.4$, $t^* = 64$ and $t^* = 78.2$). The change in profiles shape is such that within region I, they behave as if the TBL is self-similar, and they reach this apparent self-similarity again, but with a different shape in region III. The change from the initial to the final state occurs in region II. As discussed before, whenever the normalized temperature profiles collapse on one another, the Nu_r variation is inversely proportional to the TBL thickness. Based on Figure 4.14b, $Nu_{r,min}$ exhibits this proportionality within regions I and III. However, for region II and as the flow progresses from one region to the next, changes in the shape of the profile also affect the variation in the minimum Nusselt number. Each region and profile shape will be discussed in detail in the following paragraphs.

The largest fundamental difference in physics between the $Nu_{r,max}$ and the $Nu_{r,min}$ is the presence of the separation of the boundary layer in the vicinity of $Nu_{r,min}$, and the formation of the SV. Accordingly, the present analysis is undertaken to compare Case I against a case with zero wall-shear-stress, which allows slip at the wall, eliminating separation in order to understand its effect on $Nu_{r,min}$ (i.e. on heat transfer deterioration).

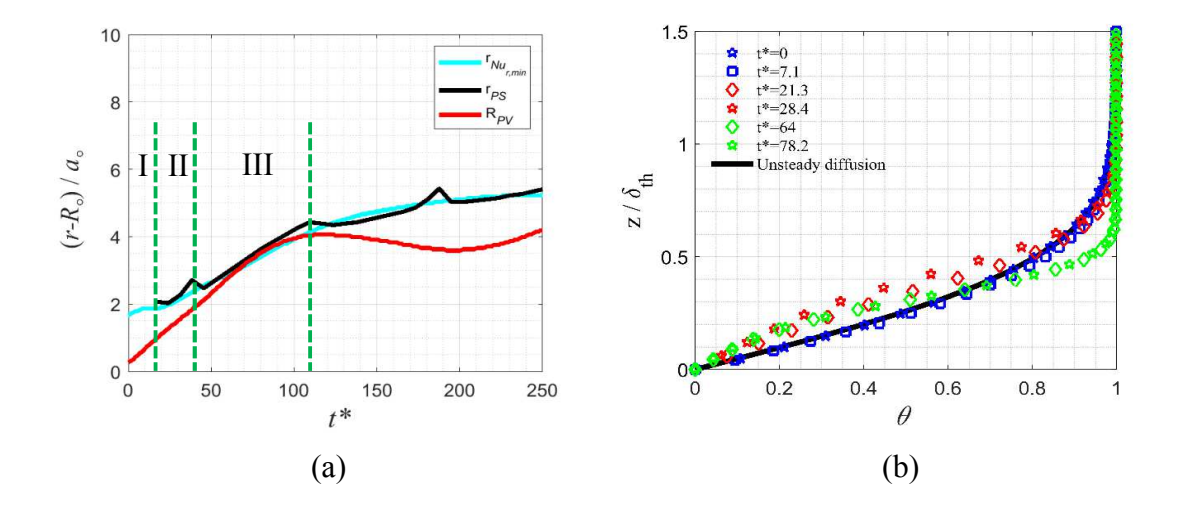


Figure 4.14 a) Normalized radial location of $Nu_{r,min}$ and the primary separation point illustrates the three regions of study; b) TBL normalized temperature profiles at the selected time instants. The semi-infinite unsteady diffusion temperature profile is added for reference.

Figure 4.15a shows the $Nu_{r,min}$ evolution for Case I and Case $\tau=0$. While both cases show the same overall trend of fast initial decay, which slows down with time and reaches a plateau. For Case $\tau=0$, $Nu_{r,min}$ reaches a smaller asymptotic value in the absence of separation. However, it is also worth noting that this decrease in $Nu_{r,min}$ is accompanied by an increase in $Nu_{r,max}$ on the downwash side of PV (Figure 4.15b). Since there is no separation, the PV keeps approaching the wall while moving radially outwards, resulting in increasing $Nu_{r,max}$ with time until the effect of the right wall starts to influence the PV ($t^*\approx 152$); specifically, making the PV move away from the bottom wall, and leading to a decrease in $Nu_{r,max}$.

To ascertain if the overall effect of eliminating separation results in better or worse heat transfer, the average Nu "beneath" the vortex is computed.

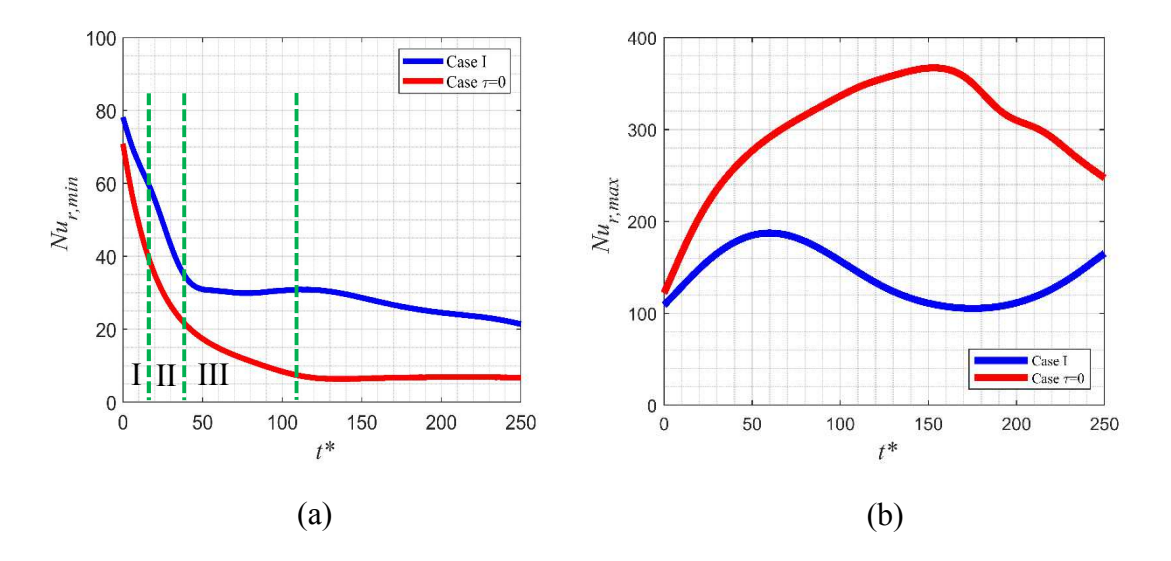


Figure 4.15 a) Temporal evolution of $Nu_{r,min}$; b) Temporal evolution of $Nu_{r,max}$ for Case I and Case $\tau = 0$.

Examination of the radially-averaged Nusselt number $(Nu_{r,avg})$ beneath the vortex shows an important improvement in the heat transfer during the vortex-wall interaction for Case $\tau=0$ (Figure 4.16). The average Nusselt number is calculated as discussed for Case I in Section 3.5, but considering only the heat transfer between the two radial locations of $Nu_{r,max}$ and $Nu_{r,min}$ (i.e. as shown in the equation below).

$$Nu_{r,avg} = \frac{\int\limits_{\theta=0}^{\theta=2\pi} \int\limits_{r=r_{Nu,rmax}}^{r=r_{Nu,rmin}} Nu_r r dr d\theta}{\pi (r_{Nu,rmax}^2 - r_{Nu,rmin}^2)}$$
(4.28)

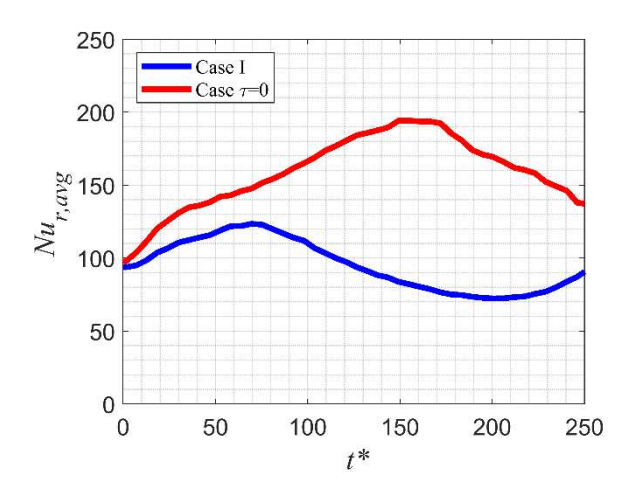


Figure 4.16 Temporal evolution of $Nu_{r,avq}$ (see Equation 4.28) for Case I and Case $\tau = 0$.

The results in Figure 4.15a are rather surprising in that they show that in the absence of boundary layer separation, the heat transfer deterioration due to vortex-wall interaction is significantly worse than if separation occurs. Yet, since the overall spatial average of the Nusselt number shows a significant improvement, the Nu enhancement on the downwash side without separation must be significantly larger than with separation. To understand the difference in physics between these two problems, snapshots of the vorticity and the thermal boundary layer are explored below at the selected time steps for Case I and Case τ =0. As depicted in Figure 4.17, each snapshot consists of three subplots arranged in the same format as that of Figure 4.2.

In Figure 4.17, plots (a) and (b) are in region I, (c) and (d) in region II, and (e) and (f) in region III. In regions I and II, before the thermal boundary layer is distorted significantly by the influences of the PV and SV, it is possible to identify the location of the thickest boundary layer. In region III, the TBL is highly distorted and at certain radial locations, δ_{th} may be multi-valued. In regions, I and II, the TBL is thickest at the top of a "ridge" in the temperature field, representing the upwelling (lift up) of heated TBL fluid due to the influence of the PV's upwash. Because this

ridge represents the largest upward displacement of heated fluid at a given z location, if it is tracked from the edge of the TBL all the way to where it intersects the wall, the intersection point should correspond to the minimum wall temperature gradient and Nusselt number. Tracking this ridge in the snapshots in Figure 4.17, where the ridge is marked with a broken white line, we see that in region I, for Case $\tau = 0$, the minimum Nu is located at the same location as the maximum TBL thickness; essentially exhibiting the mirror-image behavior found in Section 4.1.2 for the maximum Nu_r on the downwash side of the PV. In comparison, very early in the evolution (Figure 4.17a), Case I exhibits approximately the same behavior, but later in time, even before separation (Figure 4.17b), the $Nu_{r,min}$ location moves to the left of the location of the thickest TBL.

The distinct difference in the flow field between Case I and Case $\tau=0$ at $t^*=7.1$ (Figure 4.17b) is the presence of negative-vorticity boundary layer in Case I, which does not form when $\tau=0$ due to the absence of the no-slip condition. The development of this boundary layer appears to displace the "freestream" flow of the PV, causing the near-wall upwash velocity to shift towards the PV core center. This radially-inward shift of the upwash velocity profile, in Case I relative to Case $\tau=0$, can be seen in Figure 4.21, where radial profiles of u_z^* are plotted in red at the six time instants of interest for Case I (Figure 4.21a) and Case $\tau=0$ (Figure 4.21b). Inspecting this figure, which will be discussed later in more detail, and focusing on the two plots at $t^*=7.1$ clearly demonstrates the shift in the peak positive u_z^* close to the PV core center in Case I relative to Case $\tau=0$.

In region II (Figure 4.17 c and d), as the heated fluid upwelling in Case $\tau = 0$ bends along the expected flow trajectory around the PV, the thickest TBL is displaced leaving the minimum Nu_r located slightly to the right of the maximum δ_{th} . During the same time in Case I, separation of the boundary layer is associated with further significant movement of the minimum Nu_r

location to the left of the maximum δ_{th} . This causes the ridge to become highly distorted and even to break into two parts: one associated with the boundary layer edge growth of the thickest TBL and the other is related to the near-wall interaction of the PV with the separated flow. As argued for the pre-separation period, this interaction seems to take the form of the separation zone causing a blockage to the near-wall flow of the PV, displacing it upwards ahead of the separation point, at a much closer location to the PV core center than when $\tau = 0$. These results demonstrate that the occurrence of separation *decouples* the thickening of the TBL from the maximum deterioration of Nu_r . Post-separation, the near-wall features of the separation zone and its interaction with the PV are the most significant in affecting the minimum Nu_r .

The decoupling of TBL thickening and the largest Nu_r deterioration in Case I continues in region III, after the formation of the SV (Figure 4.17 e and f). In region III, the minimum Nu_r continues to displace radially inward with the displacement of the separation point. The hot uplifted fluid feeds the SV, and the near-wall ridge follows the path of this fluid. This is completely different from Case $\tau = 0$, where the ridge of uplifted fluid continues to connect the location of $Nu_{r,min}$ with the hot fluid orbiting the PV.

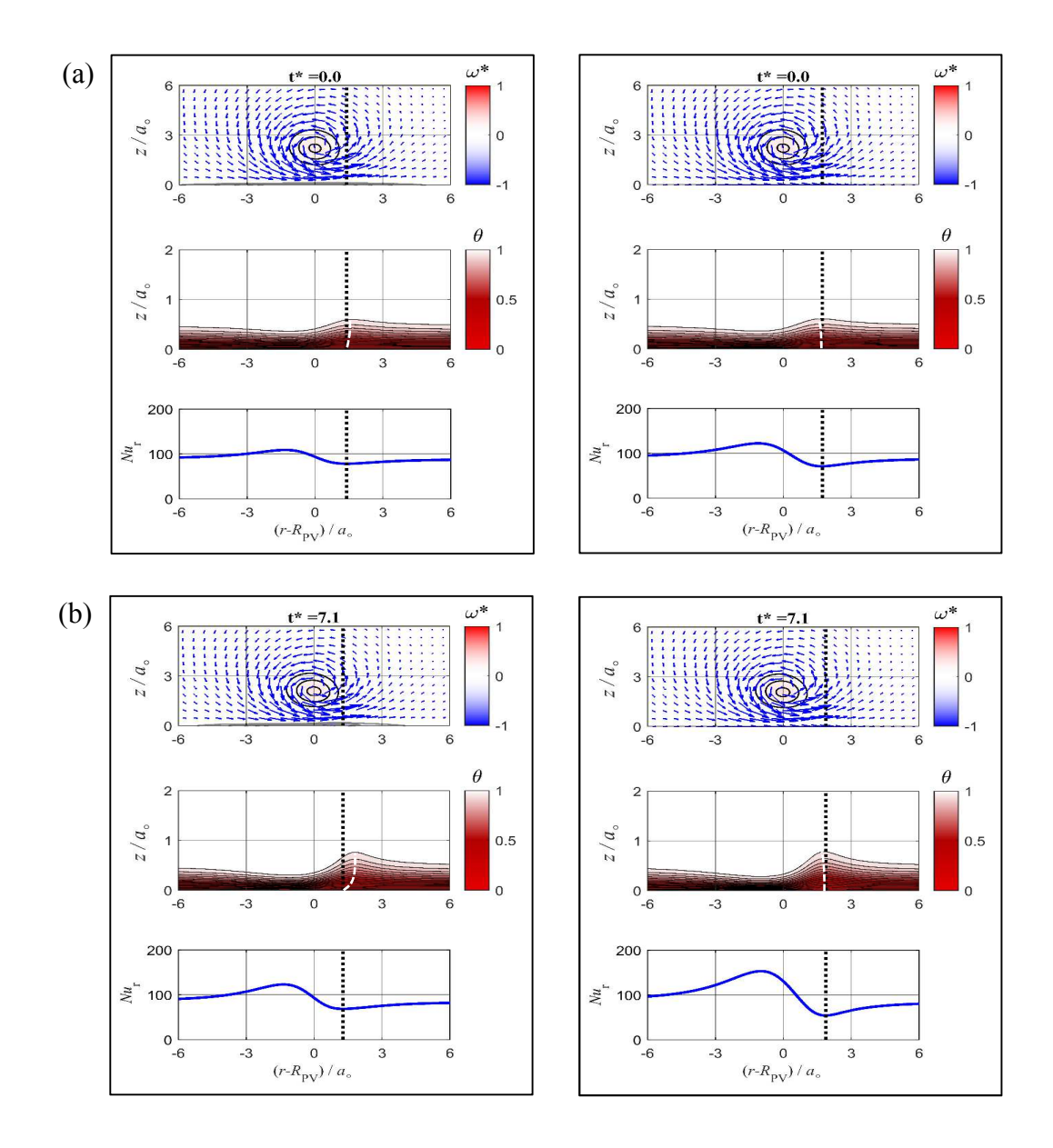


Figure 4.17 Time evolution of the initially-Gaussian-core vortex rings as they interact with a heated wall: Case I (left) and Case $\tau = 0$ (right). Shown at each time instant: the azimuthal-vorticity field and the velocity field vectors (top), the near-wall temperature field (middle) and line plots (bottom) of Nusselt number (Nu_r). The broken black line depicts the location of the $Nu_{r,min}$ while the broken white line depicts the ridge of thickest TBL.

Figure 4.17 (cont'd)

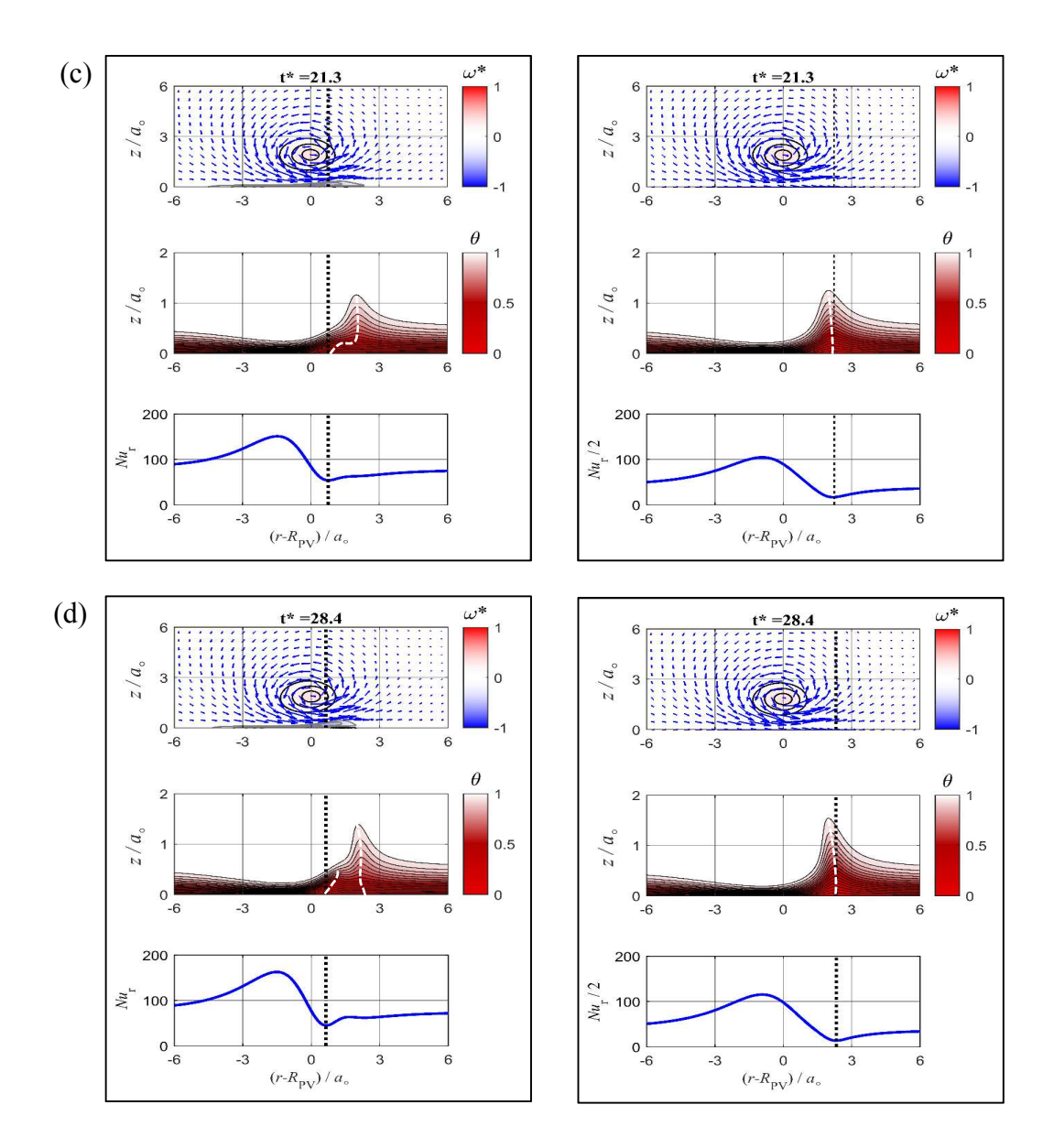
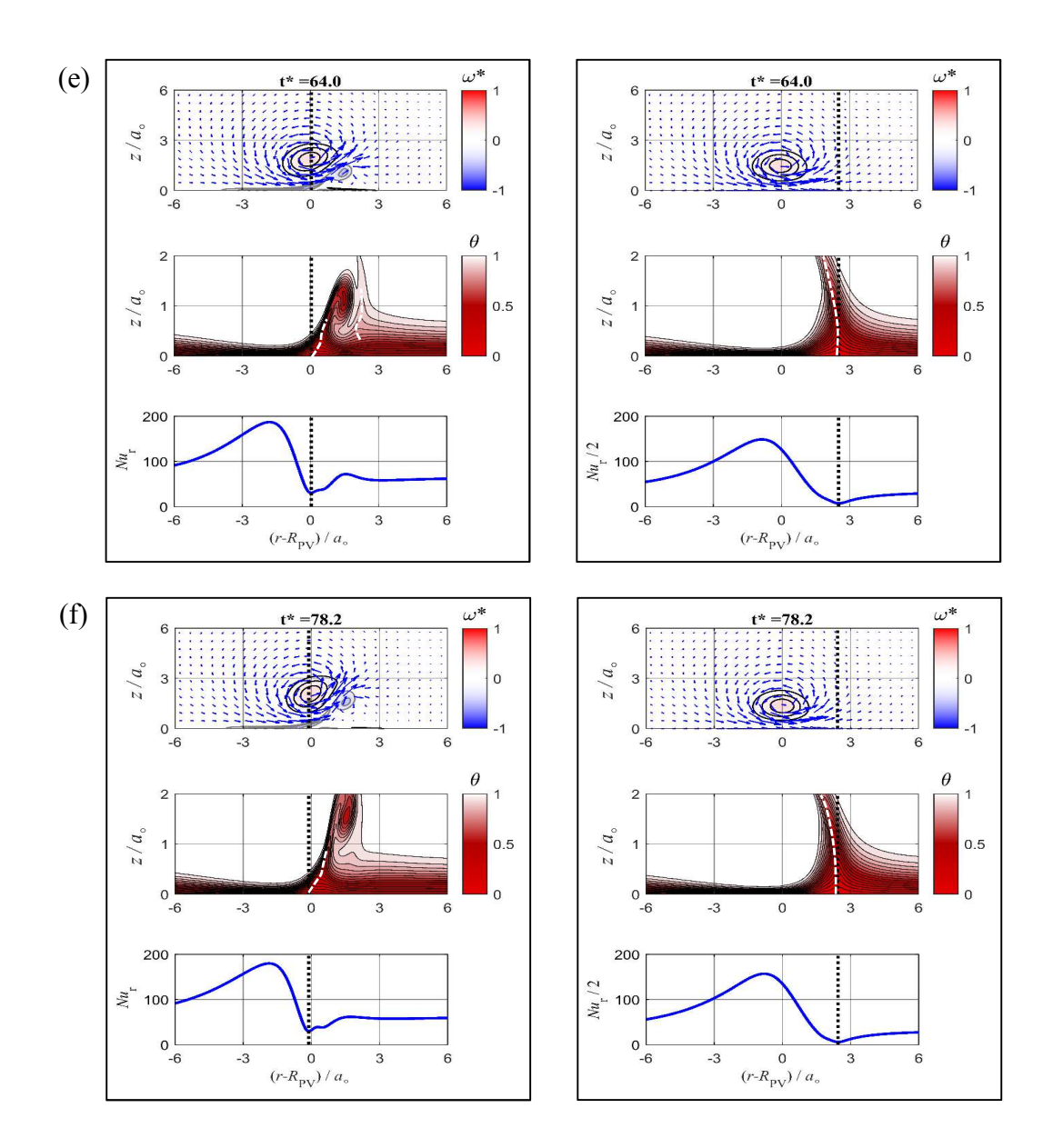


Figure 4.17 (cont'd)



The decoupling of the thickening of the TBL and the reduction in the Nusselt number implies that the TBL is not only getting thicker with time but also that the shape of the TBL temperature profile is changing; i.e. an apparent self-similarity does not exist. To examine this point further, the TBL temperature profiles at the location of $Nu_{r,min}$ are shown in Figure 4.18 for the six selected time instants in regions I, II and III for both cases (Cases I and Case $\tau = 0$). Across from the temperature profile plots, the wall-normal velocity profiles are shown at the same radial location. Inspecting Figure 4.18, for Case I, it is interesting to note that as time progresses and the boundary layer thickens, the temperature profile's shape changes. This is unlike the TBL profiles at the location of $Nu_{r,max}$, examined in the previous section, where the shape remains essentially the same as that of the semi-infinite unsteady diffusion (Figure 4.5). As noted previously, the most obvious change in the profiles shape at the location of $Nu_{r,min}$ is the development of an inflection point in the profile, seen first at $t^* = 21.4$ in the plot in Figure 4.18 after boundary layer separation occurs (the effect is subtle at $t^* = 21.4$, but it may be seen more easily in the plot normalized by δ_{th} in Figure 4.14b). Considering the corresponding u_z^* profiles, an interesting observation is noted of a possible correlation between the positive peak in the u_z^* profile and the development of the inflection point in the temperature profile. Specifically, it appears that when a peak in the velocity profile is inside the TBL, the temperature profile possesses an inflection point. Such an inflection point might be produced by fluid particles at the location of the peak moving away from the wall faster than particles near the wall, on one hand, and those at the edge of the boundary layer, on the other. This would "stretch" the TBL at z locations beneath the peak and "compress" it at locations above the peak, consistent with the presence of an inflection profile.

The development of a peak upwash velocity inside the TBL is attributed to the near-wall blockage by the separated flow, which displaces the radially outward flow beneath the PV in Case

I. This reasoning is based on two observations. First, this non-monotonic u_z^* profile is established after the separation occurs. Second, inspecting the velocity profiles at $t^* = 64$ and $t^* = 78.2$, far away from the wall the velocity is negative, indicating a *downwash*, rather than an *upwash*, influence from the PV. This is the case since at these time instants, the $Nu_{r,min}$ location is slightly to the left of the PV core center radial location. Thus, after separation, the near-wall upwash causing the largest deterioration in the Nu_r is a creature of a *local upwash* associated with near-wall separation and the PV flow blockage. This local upwash causes *local* thickening of a *near-wall sub-layer*, independent of the *global* thickening of the TBL, which is connected with the upwash of the PV alone. Since the temperature gradient *at the wall* dictates the wall heat transfer, the near-wall *local* TBL thickening is the relevant mechanism for Nu deterioration in Case I.

Contrasting the observations made above regarding Case I to the results of Case $\tau=0$ in Figure 4.18, it is interesting to see that even in the absence of separation, the TBL profiles also develop an inflection point, and hence a decoupling between global and local thickening of the TBL. Unlike Case I, this decoupling is obviously connected directly with the PV. Comparing the temperature and the velocity profiles for Case $\tau=0$, we see again that the inflection temperature profile develops when the peak in the u_z^* profile becomes embedded within the TBL. This does not take place until the last two time instants after the TBL has sufficiently thickened and the PV has descended sufficiently towards the wall for its peak upwash velocity to fall within the TBL.

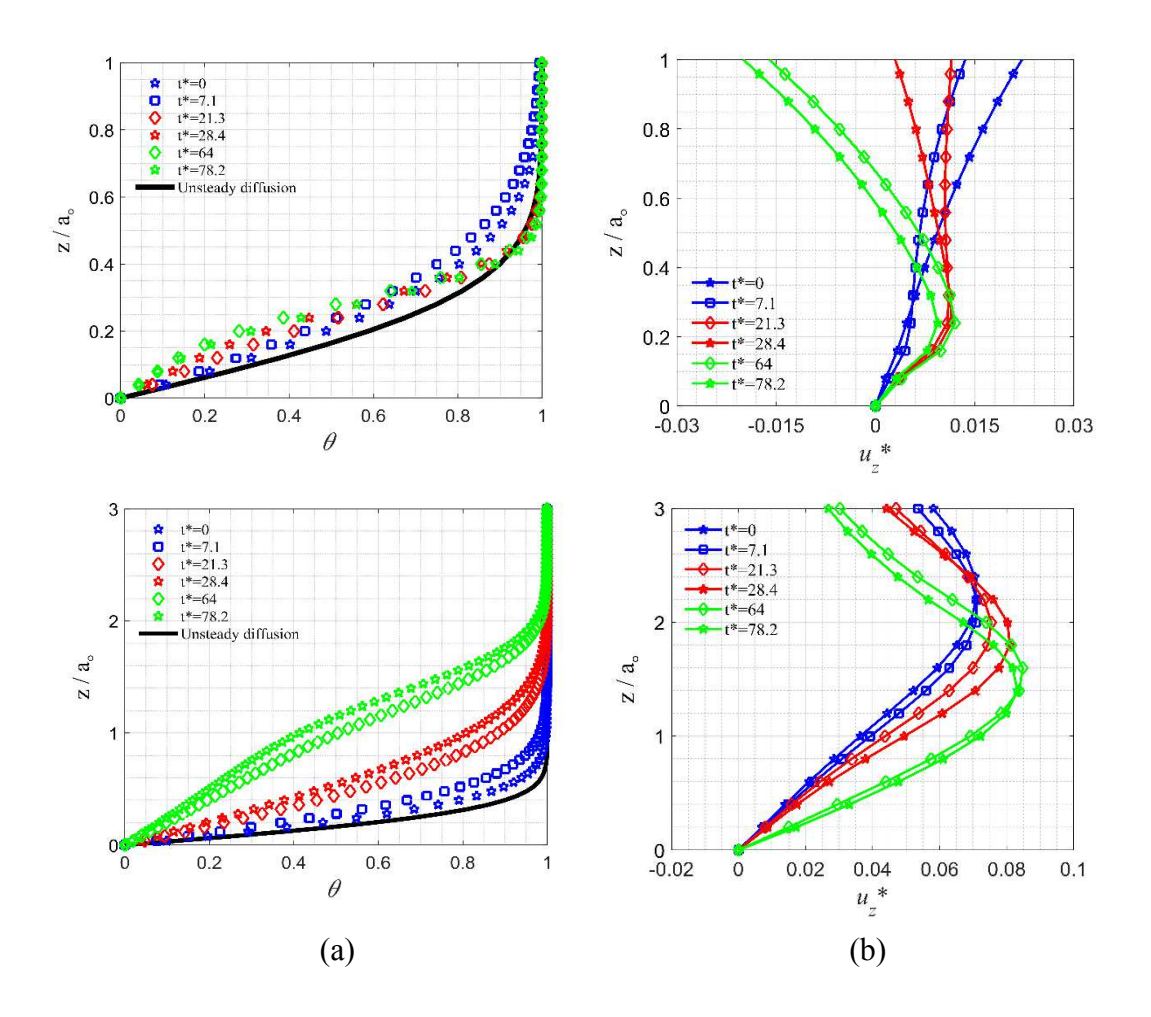


Figure 4.18 a) Temperature profiles normalized by the core radius of the PV and; b) normalized wall-normal velocity profiles, for the six selected time steps: Case I (top) and Case $\tau = 0$ (bottom).

It is important to note that the PV is able to approach the wall so closely when separation does not occur due to the absence of the SV. As discussed earlier in this thesis, the SV is known to cause PV rebound which arrests the descent and outward movement of the PV. Without the SV, the PV continues to approach the wall and move radially outwards, such that Z_{PV} becomes significantly smaller in Case $\tau = 0$, in comparison to Case I. This can be seen in Figure 4.19, where Z_{PV} for both cases is plotted using red color. While Z_{PV} is modulated via the PV-SV mutual

interaction in Case I, and has a minimum near $2a_o$ (Figure 4.19a), in Case $\tau = 0$, Z_{PV} continuously approach the wall with an asymptotic value just under a_o (Figure 4.19b).

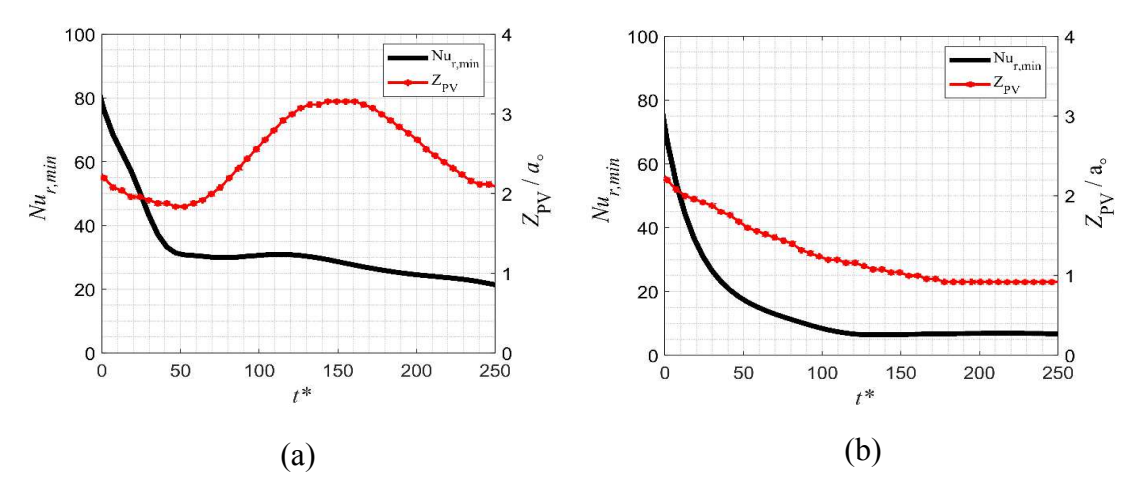


Figure 4.19 Temporal evolution of the $Nu_{r,min}$ and the wall-normal location of the core of the PV. a) Case I; b) Case τ =0.

It is important to note that the distinction between local and global thickening of the TBL is only useful when the temperature profiles do not assume an apparent self-similar state when scaled with the TBL thickness. If the profiles scale with δ_{th} , then global thickening will produce a proportional local thickening and changes in Nu may be attributed to changes in the global length scale of the TBL and/or a local thermal sub-layer scale. For both Case I (Figure 4.14b) and Case $\tau = 0$ (Figure 4.20), the temperature profiles seem to start from an apparent self-similar state and reach or approach an apparent self-similar state. The distinction between local and global TBL thickening is thus relevant to the period of change between the initial and final state. These results are, however, specific to the present problem parameters, initial condition, evolution time window, etc., and we do not know of theoretical basis for the existence of such a self-similar state. As such, we refer to cases where the temperature profiles collapse as attaining *apparent* self-similarity.

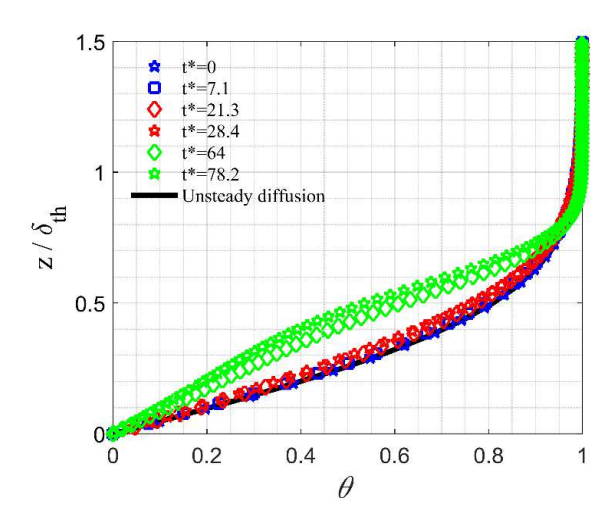


Figure 4.20 Temperature profiles normalized by the TBL thickness at the six selected time steps for Case $\tau = 0$. The profiles are the same as in the bottom of Figure 4.18a but with different normalization of z.

The profiles in Figure 4.18 also provide a clue to the rather surprising earlier observation in Figure 4.15 that in the absence of separation, the Nu deterioration is significantly larger than when separation is present. The velocity profiles in Figure 4.18 show that the upwash velocity in the absence of separation is significantly larger than that without separation. In the former case, the upwash velocity continuously increases (presumably due to continued stretching of the PV in the absence of rebound via the SV) and the TBL becomes significantly thicker, and the wall temperature gradient significantly lower, than in Case I. This implies that though the upwash effect due to near-wall blockage effects of the separated flow is undesirable, it is relatively benign compared to an unconstrained PV strengthening and approaching of the wall. However, as noted earlier, these latter effects also cause significant enhancement in the Nu on the downwash side such that the radially averaged Nu largely enhanced comparable in value between Cases I and Case $\tau = 0$ (Figure 4.16). These findings suggest that controlling separation and SV formation may lead to improvement in the wall heat transfer, as suggested in the previous chapter. Although,

this may be the case for isolated vortex-wall interaction, it is not clear if this would also be true for an impinging jet. For example, it seems likely that in an impinging jet, the trajectory of the jet vortices and how close they approach the wall would be more heavily influenced by advection by the mean jet flow rather than by the vortex dynamics of the vortex rings, which dominate the vortex evolution in isolated vortex-wall interaction.

Additional insight into the connection between the upwash velocity and $Nu_{r,min}$ is explored in Figure 4.21. This figure contains six snapshots for each of Cases I and Case $\tau=0$, with each snapshot containing the radial distribution of Nu_r and the concurrent wall-normal velocity at one node above the wall. A broken green line marks the radial location of the peak upwash (positive) velocity nearest to the PV. The radial location of this velocity is always found upstream of the location of $Nu_{r,min}$. This point is demonstrated in Figure 4.22 for both Case I and Case $\tau=0$, over the full evolution history considered. Also notable in Figure 4.21 is that the same fact that the wall-normal velocity is located upstream of $Nu_{r,min}$ applies to $Nu_{r,max}$ on the downwash side.

This relationship between the radial location of u_z^* peak magnitude and the Nusselt number peak/valley is sensible. Specifically, the velocity and Nu_r peak locations are expected to coincide only if the response of the TBL is instantaneous or quasi-steady and fluid particles advect in the wall-normal direction only (as in the 1D model problem). In the vortex-wall-interaction problem, as a fluid particle translates away/towards the wall with the maximum velocity, it will also move radially outwards (or inwards if within the separation zone) before the particle undergoes a perceptual wall-normal translation. Thus, it is reasonable to expect the peak/valley of u_z^* to be upstream of the minimum and maximum Nu locations. This is true in Figure 4.21 for both Cases I and Case $\tau = 0$, on the downwash and upwash side, and for all times.

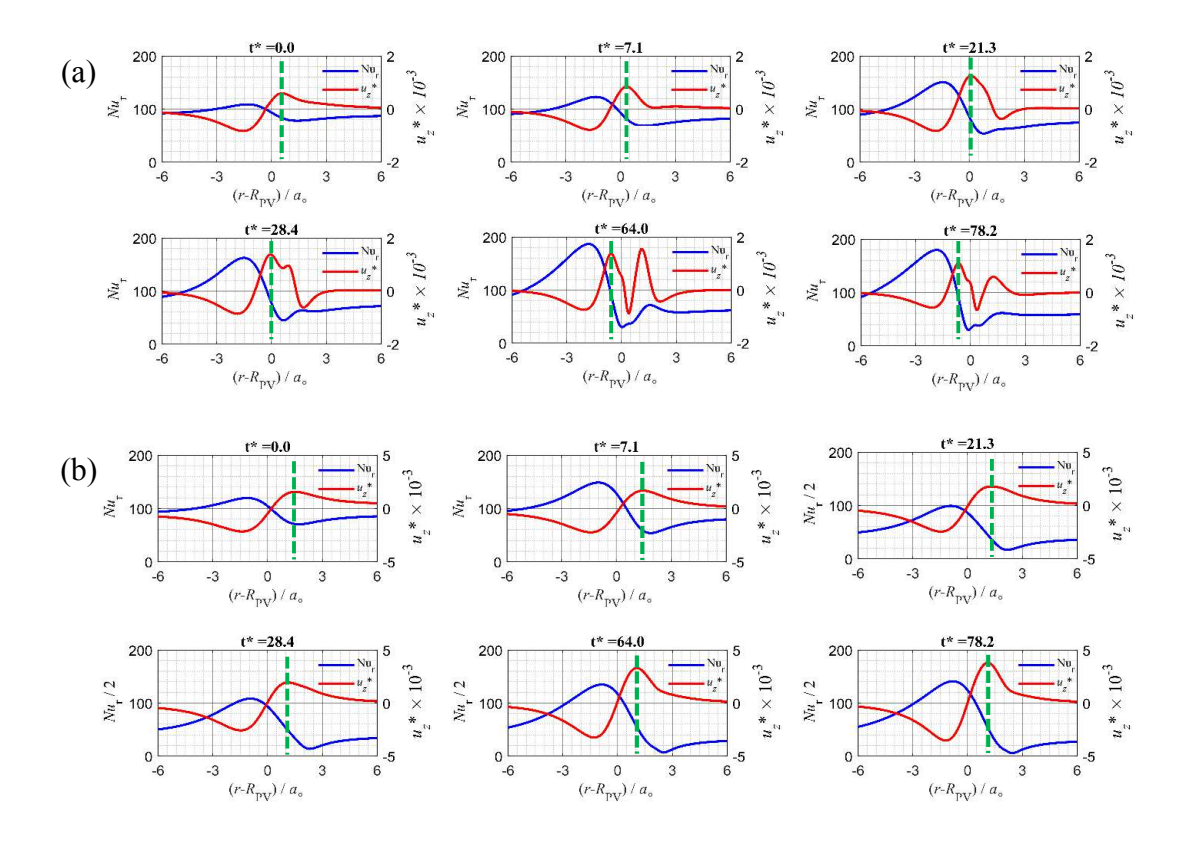


Figure 4.21 Radial distribution of u_z^* at the first grid point above the wall concurrently with the radial distribution of Nu_r at the six selected time steps. a) Case I; b) Case $\tau = 0$. In (b) Nu_r is divided by a factor of 2 for $t^* \ge 21.3$ to fit the results on the same scale as at other times.

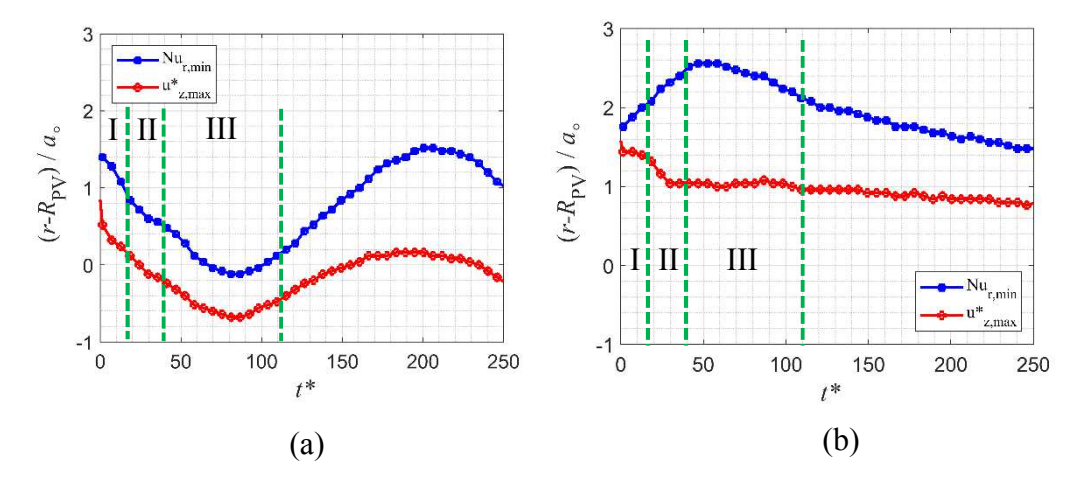


Figure 4.22 The temporal evolution of the normalized radial location of $u_{z,max}^*$ and $Nu_{r,min}$. a) Case I; b) Case $\tau = 0$.

Further comparison between Case I and Case $\tau = 0$ is made in Figure 4.23a and 4.23b. Figure 4.23a shows the radial trajectories of PV and $Nu_{r,min}$. In Case I, the $Nu_{r,min}$ location moves from the upwash side towards the PV until it is coincident with the radial location of the PV center ($t^* = 60$), then it crosses over slightly to the downwash side, before it moves back towards the upwash side again ($t^* = 110$). The return towards the upwash side happens as the SV moves away from the wall and the PV starts to rebound due to the mutual interaction with the SV. When there is no separation Case $\tau=0$, initially the $Nu_{r,min}$ location moves away from the PV then it returns and stays at almost fixed location relative to the PV center, but always on the upwash side. The location of $Nu_{r,min}$ relative to the PV center can be seen more clearly in Figure 4.23b, which shows the normalized offset plot $(r_{Nu_{r,min}} - R_{PV})/a_o$ versus time. It can be seen from the figure that in Case I the offset approximately starts at $1.5a_o$, then reaching a small negative value (coincident with the primary separation point), and then back to approximately the same original offset value. A closer look at this variation in the offset helps one connect it with the separation, the formation of the SV and the rebound of the PV. For Case $\tau = 0$, the variation in the offset value is smaller than that in Case I with an average value (shown by the black broken line) of approximately one PV diameter.

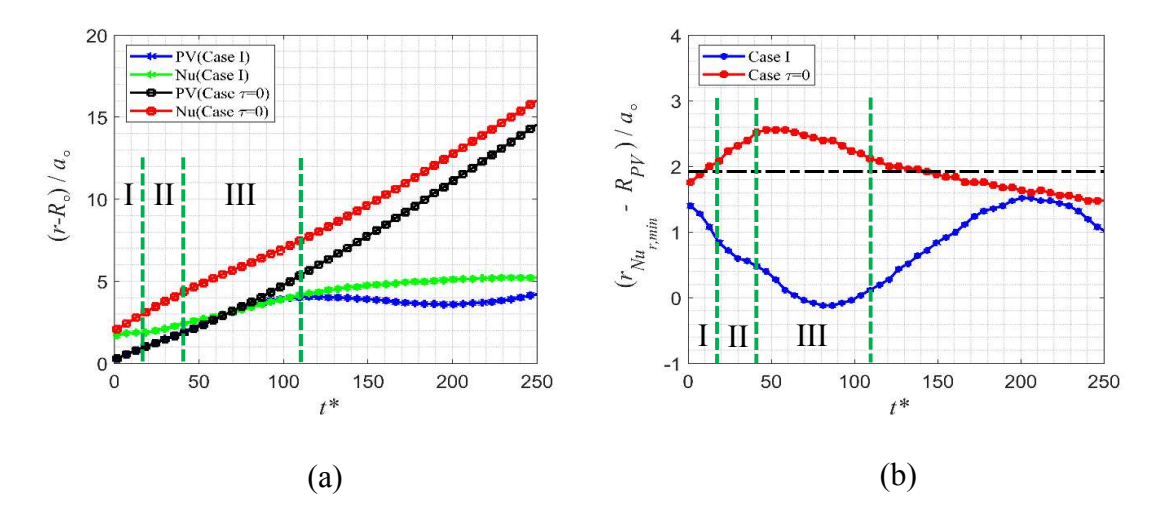


Figure 4.23 a) Temporal evolution of the radial location of $Nu_{r,min}$ and the PV core center for Case I and Case $\tau = 0$; b) Normalized offset from the PV core center $(r_{Nu_{r,min}} - R_{PV})$ for Case I and Case $\tau = 0$. The black broken line in (b) represents the average of the offset for (Case $\tau = 0$).

4.2. Lagrangian Analysis

This part of the study is carried out to examine the validity of a recent study (Hubble *et al.* [22]) that introduced a new theoretical model to explain the Nusselt number enhancement and deterioration mechanisms during vortex-wall interaction. This model, which is called "surface renewal model", was developed from an earlier edition introduced by Nix *et al.* [38] which hypothesizes that the penetration of the flow structures through the TBL and their interaction with the surface is responsible for the enhancement of the heat transfer. The Nix *et al.*'s model is purely conductive and assumes that heat is transferred by 1D unsteady diffusion into the flow structures during their "contact" with the wall. By further assuming that the structures represent a semi-infinite domain, and defining a "contact" time scale as the ratio of the mean streamwise integral length scale to the streamwise r.m.s. fluctuating velocity, the study demonstrates an agreement between the predicted and the experimental increase in the time-averaged heat transfer coefficient.

4.2.1. Description of the Surface Renewal Model

Hubble *et al.* [22] used an extension to the surface renewal model in order to capture the time-dependent thermofluidic physics of vortex-wall interaction. As illustrated in Figure 4.24, their study proposes a concept of individual particles of the fluid moving toward the wall due to the induced velocity field associated with the presence of the vortex. The figure depicts the overall configuration of the problem together with the corresponding qualitative change in the convective heat transfer coefficient beneath the vortex. Two specific wall locations are considered, one falling on the downwash side (A) and the other on the upwash side (C) with the depicted corresponding enhancement in the convective coefficient being significantly larger at A compared to C.

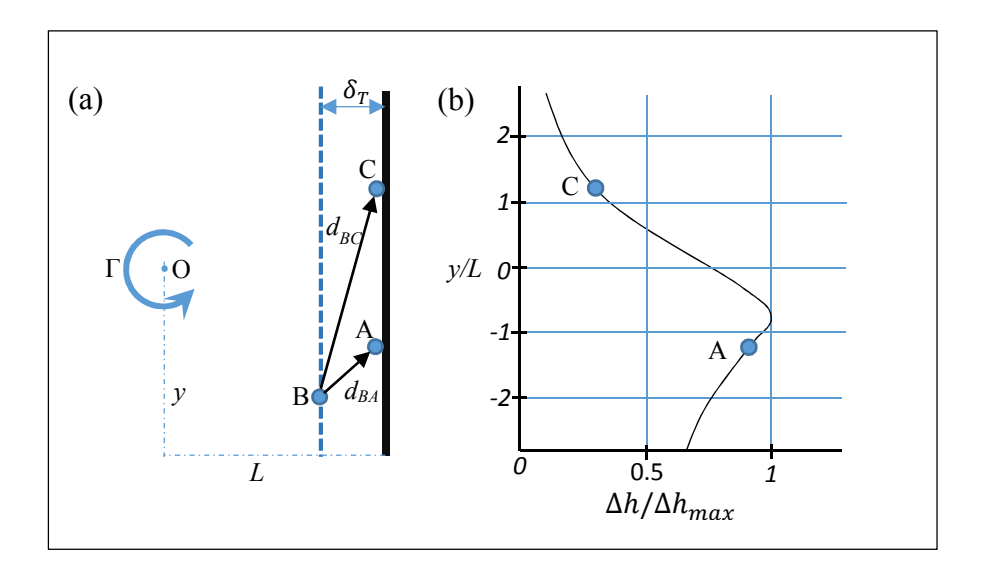


Figure 4.24 a) Schematic used in "surface-renewal" model development; b) qualitative illustration of the convective-heat transfer augmentation prediction (Equation (4.32)) as a function of non-dimensional location y/L from the vortex core center. The figure is reproduced from a sketch in Hubble *et al.* [22].

In the surface renewal model, the fluid particle starts at the outer fluid temperature and moves through the TBL. Once it reaches the TBL, the particle will exchange thermal energy with

the warmer fluid inside the TBL, and this process will cause the temperature of the fluid element to increase. The longer time the fluid particle stays inside the TBL, the higher is the temperature reached by the fluid particle, reducing the particle's capacity for exchanging thermal energy when it reaches the heated wall. The characteristic time scale of the particle heating is proposed as the time it takes for the fluid particle to travel through the TBL. This time, in turn, depends on two factors: the distance that the fluid element travels within the thermal boundary layer to reach the wall, and the average induced velocity during this travel. The values of these factors are estimated from the induced velocity field of the vortex with a specified strength and location above the wall.

The Hubble *et al.* [22] study also proposed an approximation of the average induced velocity by assuming a linear drop in the particle velocity to zero at the wall. Therefore, referring to Figure 4.24, the velocity estimated for a particle originating from point B and traveling to point A is one-half of the induced velocity at the edge of the TBL (point B). The induced velocity V_{IND} is calculated by the Biot–Savart law, giving the following expression for the average particle velocity:

$$\bar{V}(t) = \frac{1}{2} V_{IND}(t) = \frac{1}{2} \frac{\Gamma(t)}{2\pi d_{OB}(t)}$$
(4.29)

where d_{OB} is the distance from the center of vortex core to the point (B) at the edge of the TBL and Γ is the circulation of the vortex. The characteristic time for point A is

$$\tau(t) = \frac{d_{BA}(t)}{\bar{V}(t)} \tag{4.30}$$

where d_{BA} is the distance from point A at the wall to point B at the edge of the TBL, and it is equal to the distance that the fluid particle travels within the thermal boundary layer.

If the vortex strength and/or location above the wall changes, the induced velocity will change, and hence $\overline{V}(t)$ as well. The effect of this change will be felt at the wall after some delay to account for the particle travel time through the TBL. This delayed effect was accounted for using the shortest distance that a fluid particle would travel across the TBL; i.e. the TBL thickness. Hence, the time delay is given by,

$$\tau_{Delay}(t) = \frac{\delta_T}{\bar{V}(t)} \tag{4.31}$$

Hubble et al. [22] finally account for the heat transfer coefficient augmentation at point A as follows,

$$\Delta h \left(t + \tau_{Delay}(t) \right) = \frac{k}{2\sqrt{\pi\alpha\tau(t)}} \tag{4.32}$$

By adding Equation 4.31 to the heat transfer coefficient of the undisturbed boundary layer, using the square root of the squares, the total heat transfer coefficient is given by:

$$h(t + \tau_{Delay}(t)) = \sqrt{h_o^2 + \Delta h(t + \tau_{Delay}(t))^2}$$
 (4.33)

In Figure (4.24), points A and C are at the same distance from the vortex core center O, yet the augmentation in the convective heat transfer coefficient (depicted in the figure as well) is significantly less at C compared to A. As seen from the above model and Figure 4.24, while point

A and C are at equal distance from the vortex center, point A will experience much more enhancement in heat transfer than point C because of $d_{BA} < d_{BC}$.

Hubble *et al.* [22] compare their model prediction of the time-dependent heat transfer coefficient with measurements obtained in an experiment involving a vortex ring interacting with a heated flat surface. Time-resolved PIV measurements were used to capture the vortex ring evolution concurrently with heat flux sensor data of the convective heat transfer coefficient at five different locations on the wall. By calculating the vortex circulation versus time, it was possible to calculate the induced velocity above the location of one of the sensors, from which the average particle velocity, characteristic time and time delay are calculated using Equations 4.28, 4.29 and 4.30, respectively. In Equation 4.30, the authors use the steady state, undisturbed boundary layer thickness, prior to the interaction of the vortex with the wall. Once the aforementioned quantities are found from the experimental data, the corresponding time-dependent convective heat transfer coefficient is found using Equations 4.31 and 4.32.

Though the comparison between the model prediction and the data in the Hubble *et al.* [22] is positive, the Lagrangian phenomenological description upon which the model is based has not been evaluated. Specifically, such an evaluation requires boundary-layer-resolved spatio-temporal information of the velocity and the temperature field, to which the authors did not have access. Furthermore, there are some fundamental concerns regarding some of the assumptions used in the model, and the details of how it was implemented to predict the convective heat transfer coefficient for the Hubble *et al.* experiment. These concerns include:

 Using a constant thermal boundary layer thickness in the model, whereas the TBL thickness is unsteady, and according to the present study, can change significantly with time;

- 2. Using an induced velocity form that is applicable to a line rather than a ring vortex, and not taking into account the presence of the wall (effect of the image vortex);
- 3. The surface renewal model does not take into account the unsteady boundary layer separation and the SV formation (which implicitly assumes the insignificance of these phenomena to the heat transfer process);
- 4. The authors do not provide sufficient details to understand how they compute the particle travel distance d_{BA} , which is a critical factor in computing the characteristic time, and hence the overall prediction of the model. Specifically, it is not clear if this distance was used as a "fit parameter" to get the best agreement between the model and the data, or was it computed directly from the data. The latter does not seem to be an easy task, requiring knowledge the TBL thickness and the trajectory of particles within the TBL before reaching the wall;

4.2.2 Evaluation of the Surface Renewal Model

Given that the present study has access to boundary-layer resolved information of the vortex-wall-interaction problem, one of the current research goals is to evaluate the hypotheses upon which the Hubble *et al.*'s model is based. To this end, a Langragian analysis was done by tracking fluid particles that are "in contact" with the wall at times selected to correspond to certain features on the evolution curves of both the maximum and the minimum Nu_r ; as shown in Figure 4.25a for $Nu_{r,max}$, and 4.25b for $Nu_{r,min}$. "In contact" is taken to mean that the particle resides at the first grid point above the wall at the radial location where $Nu_{r,max}$ or $Nu_{r,min}$ is observed at the time of interest. Since the first grid point is within the linear zone of variation of the TBL temperature profile, and the wall temperature is constant, then the particle temperature at the instant of observation sets the wall temperature gradient and the Nusselt number. Specifically,

cooler particles produce higher Nu_r and vice versa. With this point clear, what remains to evaluate the assumptions of the renewal hypothesis is to track the history of the particle trajectory, temperature, and energy exchange. The points on the $Nu_{r,max}$ curve (as it evolves with time in Figure 4.25a) are chosen to be at the maximum, the minimum and an arbitrary in-between point. On the other hand, for the $Nu_{r,min}$ curve, the first two points are chosen during early evolution where $Nu_{r,min}$ is decreasing as time progresses, and the last point is chosen where the curve reaches a plateau.

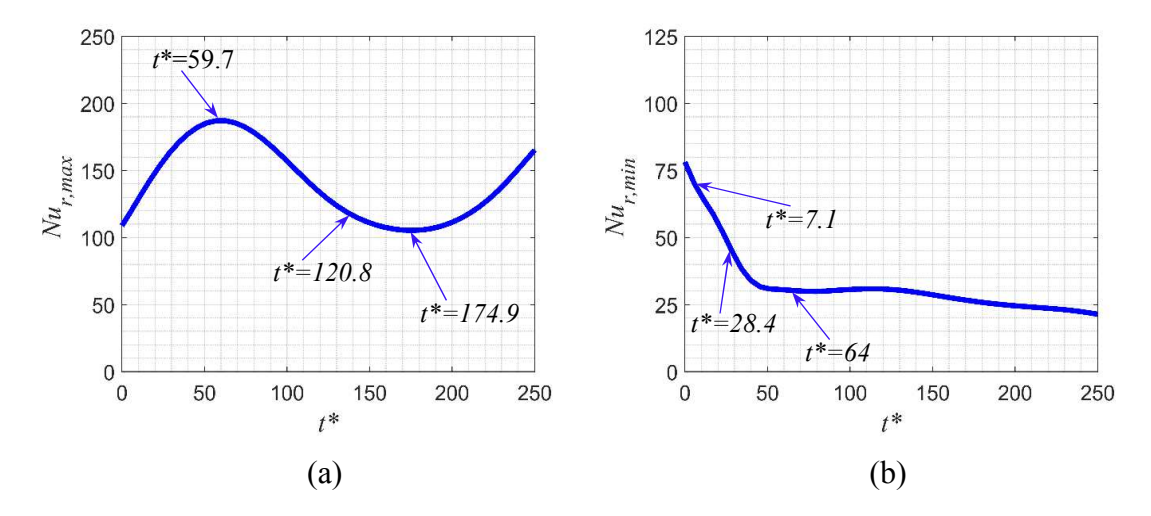


Figure 4.25 Temporal evolution of; a) $Nu_{r,max}$; and b) $Nu_{r,min}$, showing the selected time instants at which particles are identified and tracked backward in time.

To track a fluid particle, 2D linear interpolation of the velocity field is applied to refine the original CFD grid by a factor of 32. The resulting grid spacing is $0.00125a_o$, which is so small such that the velocity is almost uniform over a single grid cell. Using, the finer grid, the trajectories of the particles are tracked backwards in time using first-order finite difference to calculate the particle's location one time step Δt earlier. Specifically, the radial and the wall-normal particle locations at time step i-1 can be computed from the particle velocity and location at time step i, as follows:

$$r_{p,i-1} \approx r_{p,i} + u_{r,i} \times (-\Delta t) \tag{4.34}$$

$$z_{p,i-1} \approx z_{p,i} + u_{z,i} \times (-\Delta t) \tag{4.35}$$

Where Δt is the same as the time step of the CFD. Equations 4.34 and 4.35 are applied recursively, starting from the selected initial time and particle location. Aside from the initial time, the particle location generally does not coincide exactly with a grid point. However, given the very fine interpolated grid employed for particle tracking, velocity information at the current time is taken as that at the grid point closest to the current particle location. The same technique of grid refinement is also used for the temperature field to approximate the temperature, temperature gradient and Laplacian of the temperature field at the location of the particle at every time step.

The results for all particles are plotted in the reference frame of the PV for both $Nu_{r,max}$ and $Nu_{r,min}$, as shown in Figure 4.26a and 4.26b respectively, for the purpose of comparison (noting that the scale of the normalized axial location in Figure 4.26a is *ten times* larger than the one in 4.26b). Different particles are represented using different symbol shape and the time instant at which the particle is at the radial location of $Nu_{r,max}$ or $Nu_{r,min}$ (depending on the case) is identified by giving the symbol a black color while the starting points of the particles at the time (t^* =0) are pointed out by the colored arrows that match the color of each particle.

Focusing first on $Nu_{r,max}$ results (Figure 4.26a), as known from earlier analysis, all three particles that are associated with the $Nu_{r,max}$ at the selected time instants are on the downwash side and they all reside at the same radial location of $(r - R_{PV})/a_o \approx -1.8$ from the center of PV at the instant when the associated $Nu_{r,max}$ occurs (i.e. when the plot symbols are black). Interestingly, the initial location of the particle that produces the largest $Nu_{r,max}$ over the entire

history of $Nu_{r,max}$ evolution (at $t^* = 59.7$) is deeper inside the TBL, and the particle's initial temperature is higher than the initial temperature of the two other selected particles. The latter can be seen from the temperature history in Figure 4.27a. This suggests that the two other, initially cooler particles must have exhibited more energy exchange with the hotter fluid before reaching the wall, causing their temperature to be higher "at the wall" than the particle reaching the wall at $t^* = 59.7$. This is confirmed in Figure 4.28a, where the history of the diffusive heat flux term in the energy equation is shown for each of the particles. The higher heat flux together with the longer time to reach the wall cause the two particles arriving later at the wall to be hotter and produce lower $Nu_{r,max}$ than the first particle.

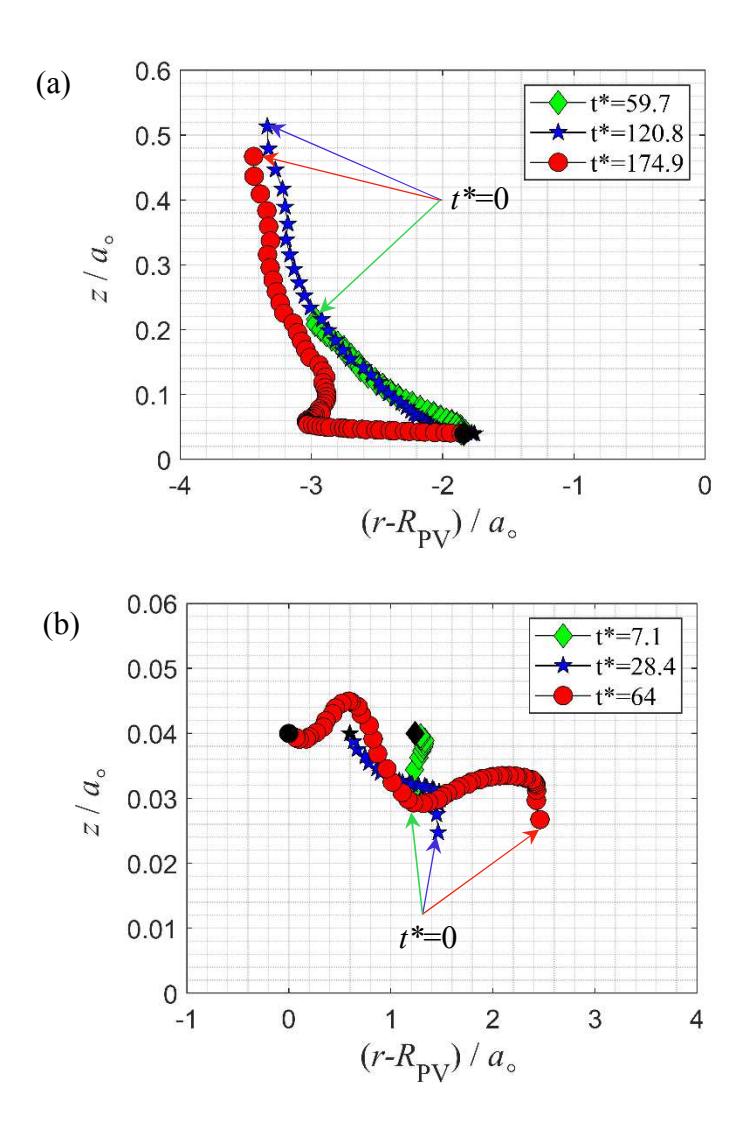


Figure 4.26 The trajectories of the selected particles: a) $Nu_{r,max}$; b) $Nu_{r,min}$. The black markers on each plot indicate the starting time of backward integration (shown in the legend) to calculate the particle trajectory history and the arrows indicating the initial position of the particles.

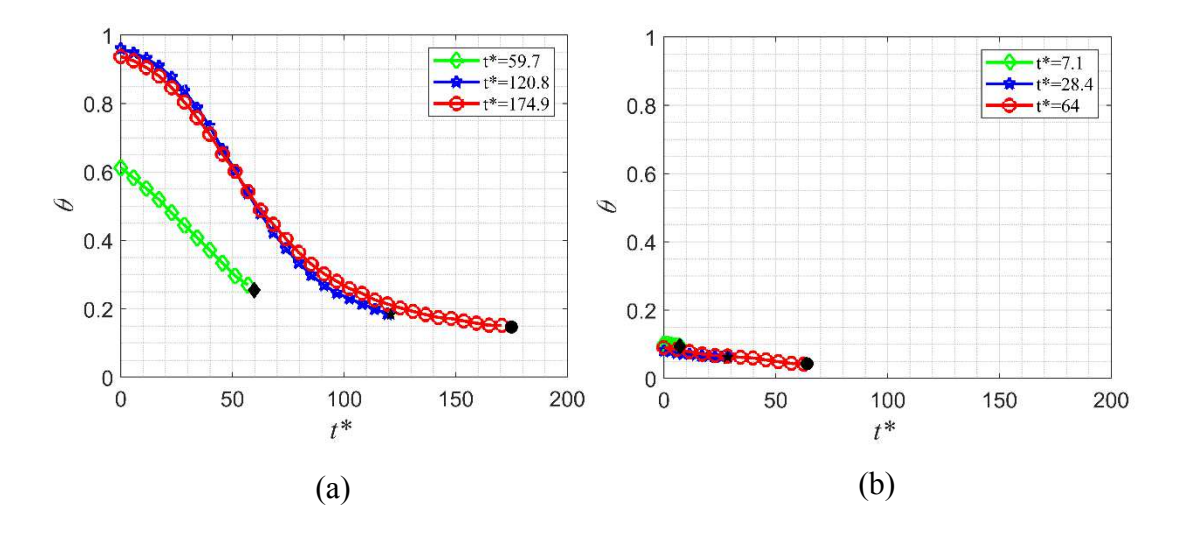


Figure 4.27 Evolution of the temperature of the selected particles: a) $Nu_{r,max}$; b) $Nu_{r,min}$. The black markers on each plot indicate the starting time of backward integration (shown in the legend) to calculate the particle trajectory and temperature history before reaching the wall. Noting that $(\theta = 0)$ corresponding to the higher temperature.

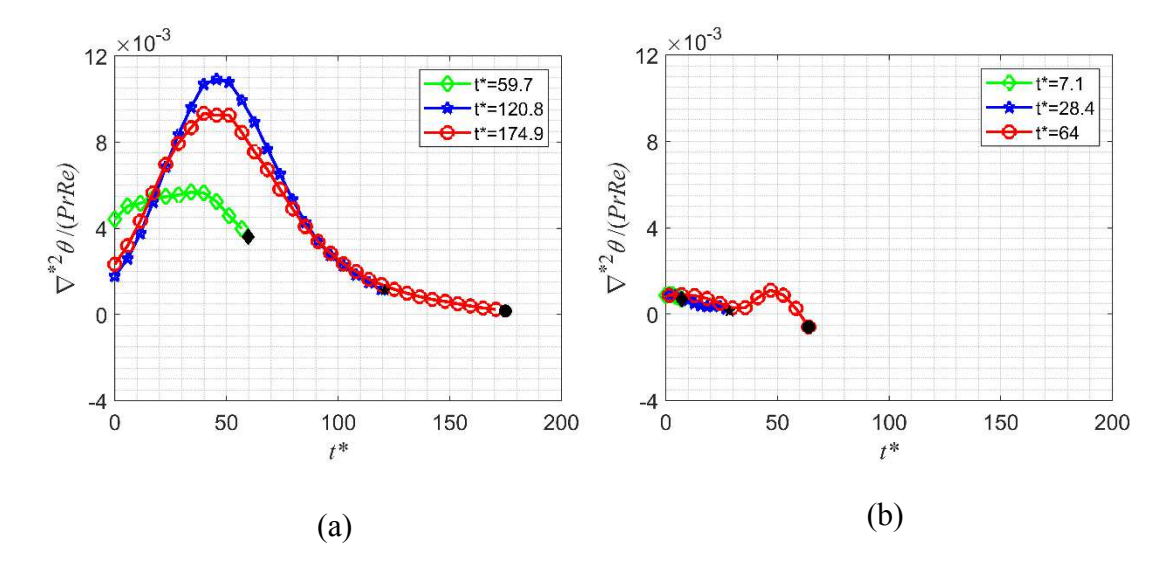


Figure 4.28 History of the rate of temperature rise of the selected particles: a) $Nu_{r,max}$; b) $Nu_{r,min}$. The black markers on each plot indicate the starting time of backward integration (shown in the legend) to calculate the particle trajectory and temperature history before reaching the wall.

The above observations show that most of the elements of Hubble et al.'s hypothesis are consistent with the flow and the temperature field behavior on the downwash side of the model. Specifically, particles move across the boundary layer while their temperature increases by thermal exchange of energy with their surroundings, and ultimately particles that arrive with the lowest temperature at the wall produce the highest cooling. However, there are two aspects that are overlooked in the hypothesis. First, Hubble et al. [22] assume that the coldest particles reaching the wall are ones that take the shortest time to reach the wall. Their argument does not take into account the specific energy exchange history. For example, a particle might take less time to reach the wall, yet it could be exposed to higher heating rate, causing its temperature to be higher at the wall. Though not shown here, these would be particles associated with $Nu_{r,max}$ at times preceding the occurrence of the first peak in $Nu_{r,max}$; i.e. $t^* < 59.7$. Second, Hubble et al.'s hypothesis assumes that the maximum Nu_r is produced by cold particles originating from outside the TBL. All particles tracked here originate from inside the TBL (as seen from their initial temperature that is hotter than T_{∞}), with the particle providing the largest cooling originating from the bottom half of the TBL.

On the other hand, particles that contribute to $Nu_{r,min}$ (Figure 4.26b) come originally from the upwash side and they move almost horizontally (i.e. parallel to the wall) toward the center of the PV, with their temperature becoming slightly hotter (Figure 4.27b), as time progresses. As seen from earlier results in Section 4.1.4, the radial location of $Nu_{r,min}$ relative to the PV core center changes significantly with time, rather than remaining roughly the same as in the case of $Nu_{r,max}$, because of the movement of the unsteady separation. Also, the associated low rate of heating of the $Nu_{r,min}$ particles can be seen in Figure 4.28b.

Significant in the above results is that, prior to arrival at the radial location of $Nu_{r,min}$, the particles stay on the upwash side of the PV. These results show an essential difference from the statements of the surface renewal model, which assumes that the heat transfer on the upwash side is caused by particles that move from the downwash to the upwash side. As explained before, Hubble et al. [22] then presume that the longer time spent by the particle to get across the vortex, causes more heating of the particle, and hence lower Nu on the upwash compared to the downwash side. The present results clearly show that the Hubble et al. [22] model is inappropriate for the upwash side heat transfer.

In summary, the present analysis demonstrates that Hubble *et al.* [22] surface renewal model reasonably represents the downwash-side heat transfer, though it does not account for the particle heating history and for particles originating from inside the TBL. On the other hand, the model is based on the wrong physics when it comes to the upwash-side heat transfer.

CHAPTER 5

CONCLUSIONS AND RECOMMENDATIONS

A CFD study is carried out in two stages. First, employing three flow configurations of axisymmetric vortex rings interacting with a constant-temperature heated flat wall. These configurations constitute simplified model problems representing vortex-wall interaction scenarios that occur in impinging jets when the jet vortices interact with the wall prior to (Case I), during (Case II) and after (Case III) vortex pairing. The second stage is aimed at developing a deep insight into the detailed physics of how the vortex-wall interaction affects wall heat transfer. A second goal of this stage is to evaluate a recently published model by Hubble *et al.* [22] (based on what is known as the "surface renewal hypothesis") of the mechanisms responsible for the enhancement and deterioration in wall heat transfer due to this interaction. Conclusions concerning the two stages of the study are summarized in sections 5.1 and 5.2 respectively.

5.1. Vortex Rings-Wall Interaction and Heat Transfer

General observations of the vorticity field, temperature field, wall friction coefficient and Nusselt number (Nu) provide insight into the association of local maxima and minima in the radial distribution of Nu with the different flow features. In comparison to unsteady heat diffusion, the results show that there is an enhancement of heat transfer on one side of the primary vortex PV (the one with the smaller ring diameter in the case of a vortex pair) where a downwash towards the wall and thinning of the thermal boundary layer are present. On the opposite side of the vortex, a decrease in the heat transfer is observed, where boundary layer thickening and unsteady separation, and formation of secondary and higher order vortices take place. These observations are generally consistent with the literature on single vortex interacting with a heated wall.

The enhancement/deterioration in wall heat transfer is associated with an instantaneous radial distribution of the Nusselt number that is characterized with a peak and a valley. A strong correlation is found between the proximity of the primary vortex to the wall and the maximum local Nu, while a similar correlation is identified only during early evolution of the PV for the minimum local Nu. The correlation with the maximum local Nusselt number is such that the closer the vortex to the wall, the higher the maximum Nusselt number. However, the Nu response seems to lag variation in the wall-normal position of the primary vortex core center, suggesting the presence of inherent thermal response dynamics. On the other hand, the evolution of the minimum Nu seems to be tied to the development of the unsteady boundary layer, its subsequent separation and the formation of the secondary vortex SV. Once separation occurs, the minimum Nu is always found in the immediate vicinity of the separation point of the boundary layer, on the upwash side or beneath the primary vortex. These observations are examined in detail in the second stage of the study (see section 5.2 for related conclusions).

Notwithstanding the mixed positive and negative influences of vortex-wall interaction on the wall heat transfer, calculation of the radially-averaged Nusselt number shows that, overall, the interaction leads to significant improvement in comparison to unsteady diffusion. Moreover, the results also demonstrate that when vortex-wall interaction occurs during pairing, this improvement in the heat transfer is substantially better in comparison to single vortex-wall interaction. The better enhancement results from the concurrent vortex-vortex and vortex-wall interactions, where the former strengthens the latter.

While this study demonstrates the benefit of having vortex-wall interaction take place during the pairing of vortices, it is not obvious that this benefit would persist in impinging jets where the interactions are periodic rather than isolated as examined in the present work. In impinging jets, single-vortex pre-pairing interactions occur at twice the frequency of dual-vortex during-pairing ones. As such for the latter to produce better wall cooling than the former, in the time average sense, the interactions need to be twice as strong. The study of isolated vortex interactions does not show such a strong enhancement during vortex pairing. However, other factors (summarized below) also influence the strength and the persistence of the enhancement, which makes it difficult to conclude based on this study alone whether pre- or during-pairing vortex interactions would ultimately be more beneficial for wall cooling in impinging jets.

On the flip side, the strong vortex-vortex interaction in Case II also leads to the formation of a particularly strong SV, which in turn leads to a relatively large decay in the enhancement of heat transfer by causing a substantial rebound of the PV away from the wall. However, the rebound and the SV characteristics observed in the isolated vorticity-wall interaction are not likely to be as strong in impinging jets. Thus, the deterioration in the maximum Nusselt number in Case II may be less problematic in impinging jets. More importantly, the study demonstrates that to capitalize on the potential of strong *Nu* enhancement during near-wall vortex pairing, it is recommended that flow control strategies of impinging jets should couple control of the jet at its exit with separation control on the impingement wall in order to mitigate the effect of the secondary vortex. This might lead to a sufficiently strong improvement in wall cooling to offset the reduction in the frequency of vortex-wall interactions associated with vortex pairing in comparison to the pre-pairing single-vortex scenario. If not, jet control efforts should target the delay of vortex pairing such that it does not occur ahead of, or as the vortices advect past the impingement wall.

5.2. Heat Transfer Mechanism

In this stage of the study, analyses are carried out by comparing Case I from the first stage with CFD of two additional hypothetical cases. One of the latter cases is the same as Case I, but

with the thermal diffusivity set to zero ($\alpha=0$) to investigate the effect of the thermal diffusion on the heat transfer enhancement on the downwash side of the vortex ring. This investigation also makes use of a simple analytical calculation of a model problem of one-dimensional heat transfer in the presence of uniform unsteady wall-normal suction velocity. The second CFD hypothetical case is also identical to Case I, except for employing a wall boundary condition of zero wall shear stress ($\tau=0$) to eliminate the separation of the boundary layer on the upwash side of the primary vortex. This enables investigating the effect of separation on the deterioration in the heat transfer. The analyses and comparison between Case I and Case $\alpha=0$ is focused on the location of $Nu_{r,max}$; while contrasting Case I and Case $\tau=0$ is focused on the location of $Nu_{r,min}$. In addition to these two comparisons, further investigation is conducted using Lagrangian analysis of Case I in order to evaluate the "renewal hypothesis" model introduced by Hubble *et al.* [22] regarding the mechanism of heat transfer during vortex-wall interaction.

The analyses of Case I and Case $\alpha=0$ regarding the heat transfer enhancement focused on the temperature profiles at the radial locations of $Nu_{r,max}$ for selected time steps. Results show that these profiles collapse when scaled with the thermal boundary layer (TBL) thickness, and that the maximum Nu is effectively constant when normalized with the TBL thickness ($Nu_{r,max}^*$). These observations reveal that the heat transfer enhancement is inversely proportional to the boundary layer thickness and that the Nusselt number enhancement on the downwash side of the PV is a consequence of TBL thinning relative to unsteady diffusion TBL. It is hypothesized that the most influential factors affecting the TBL thickness is the wall-normal velocity, which thins the TBL on the downwash side, and thermal diffusion which thickens the TBL.

A simple 1D model is used to examine the balance between the downwash velocity and thermal diffusion in the presence of sinusoidal oscillation of the velocity. The results show that in

the limit of small normalized frequency (ω^*), the Nusselt number varies quasi-steadily with the velocity. However, as ω^* increases, the change in Nu lags behind the downwash velocity and the Nu amplitude is attenuated, with the lag and attenuation increasing monotonically with frequency. These first-order physics of the simple model problem are found to be consistent with the nearwall downwash velocity and Nusselt number variation in Case I of the vortex-wall interaction.

In Case $\alpha=0$, it is found that the wall-normal velocity is the only mechanism altering the TBL thickness in the absence of thermal diffusion. In this case (which is the opposite limit of quasi-steady, or $\alpha\to\infty$), at any time instant the TBL thickness at a given location depends on the entire integrated history of the wall-normal velocity (in comparison to the instantaneous value of the velocity in the quasi-steady limit). For locations that always remain on the downwash side of the PV, the TBL thickness decreases monotonically with time (in the absence of the thickening mechanism of thermal diffusion), causing the Nusselt number to reach values that are significantly higher than those found in Case I.

The heat transfer deterioration analyses are focused on the radial location of $Nu_{r,min}$. It is found that the deterioration is driven by boundary layer thickening and wall temperature gradient weakening due to the upwash velocity. This finding is only true early in time, where the TBL temperature profiles at different times collapse when normalized with the TBL thickness. However, later in time, the TBL temperature profile changes, developing an inflection point. During this change, the near-wall thickening of the TBL occurs at a rate that is different than that of the TBL thickness, and hence the heat transfer deterioration can not be interpreted directly in terms of global thickening of the TBL. The strong correlation between the upwash velocity and Nusselt number deterioration is supported by strong correlation between the radial location of the near-wall upwash velocity and that of the minimum Nu.

For both Case I and Case $\tau=0$, the development of an inflection point in the TBL temperature profile seems to take place when a peak in the wall-normal velocity is established inside the thermal TBL. For Case I, such a peak develops due to separation and formation of the SV. For Case $\tau=0$, the peak develops due to the ability of the PV to get very close to the wall (due to the lack of PV rebound via the SV effect), coupled with continuous thickening of the TBL on the upwash side of the PV. The difference in the flow dynamics on the upwash side near the wall between the two cases leads to a different mechanism for the development of TBL thickening. For Case I, the development of a near-wall TBL thickening mechanism is different than that of the global thickening of TBL, is connected to separation of the boundary layer and the formation of the SV. While in the absence of separation (Case $\tau=0$) boundary layer thickening is found to be connected to the maximum upwash velocity of PV.

The above findings are further examined by tracking the radial location of $Nu_{r,min}$. As the PV interacts with the separated layer and the SV, the maximum upwash velocity near the wall moves with the separation point, and the minimum Nusselt number radial location moves in synchronization. This movement is such that the minimum Nu moves from the upwash side towards the PV core center, overshooting slightly to a smaller radial location than that of the core, before returning to the original location as the SV moves away from the wall. On the other hand, in the absence of separation (Case $\tau = 0$), the maximum upwash velocity remains approximately at the same location relative to the PV center (about one initial core diameter) and the $Nu_{r,min}$ stays at an approximately constant offset outboard of that location.

A rather unexpected finding is that the deterioration in the Nu is significantly more when separation is not present (Case $\tau = 0$). This is attributed to a significantly stronger upwash velocity near the wall due to the ability of the PV to get very close to the wall, in comparison to the upwash

velocity produced by the interaction of the PV with the separation zone and the SV. However, this closer approach of the PV toward the wall also results in a higher enhancement on the downwash side which is in turn leads to an enhancement in the heat transfer when the Nusselt number is radially-averaged between the locations of the maximum and minimum values. This finding supports the conclusion in section 5.1 that significant potential enhancement in the heat transfer, beyond that documented in the first stage of the study, could be achieved when vortex pairing occurs during the wall interaction, if control strategies are applied to the impingement wall to eliminate/weaken the boundary layer separation and the formation of SV.

Finally, a Lagrangian analysis is conducted to evaluate the renewal hypothesis of Hubble *et al.* [22]. The findings of the analysis are partially consistent with Hubble *et.al.* [22] hypothesis regarding the enhancement of the Nusselt number. However, it is demonstrated that the hypothesis does not take into account the fluid particles thermal energy exchange histories, and the hypothesis assumes that the particles originate from outside TBL, which is not necessarily correct, based on the current results. On the other hand, when it comes to the mechanism of heat transfer deterioration, the Hubble *et al.* hypothesis is found to be based on wrong physics.

5.3. Recommendations

This study led to several recommendations, which are summarized briefly below. It is recommended to broaden this study using experimental and computational works involving different Reynolds and Prandtl numbers to investigate the hypothesis that the interplay between the *wall-normal* velocity and thermal diffusion scales with the product *PrRe* in the isolated vortexwall interaction, and possibly in the impinging jet, heat transfer.

Based on the conclusion from both stages of the study, it is recommended to conduct a CFD case to investigate the hypothesized significant enhancement in the heat transfer,

corresponding to vortex pairing while interacting with the wall, when boundary layer separation is eliminated; i.e. using zero wall shear stress ($\tau = 0$) boundary condition. Depending on the finding of such study, another recommendation is to expand the study by implementing CFD/experimental studies using different, realistic, control strategies to control the unsteady separation of the hydrodynamic boundary layer.

Finally, it is recommended to expand the Lagranagian analysis to gain deeper insight into the heat transfer deterioration on the upwash side of the PV. This could be done by tracking more particles at different radial locations in the vicinity of the separation region and correlate their motion to the minimum Nusselt number. The analysis could include, but is not limited to, Lagrangian Coherent Structure (LCS), to identify the unsteady separation and correlate it with thermal energy exchange, near-wall velocity, etc.

APPENDICES

APPENDIX A: Computational Validation

In order to validate the computational results, the independence of the solution of the grid, the domain size, and time step is checked, as shown in this Appendix. Three different grid sizes are chosen to check the grid-size dependency of the solution, i.e. 500×500 , 600×600 and 715×715 grid elements for a domain size $0.06 \text{ m} \times 0.06 \text{ m}$. All other computational parameters are the same as given in section II.B. The results are shown in Figures A.1 through A.4 for the maximum vorticity at the core center of the PV, the maximum vorticity at the core center of the SV, the maximum vorticity of the BL, and for the maximum of the Nusselt number radial distribution, $Nu_{r,max}$. Results presented in this document are obtained using 715×715 -point grid.

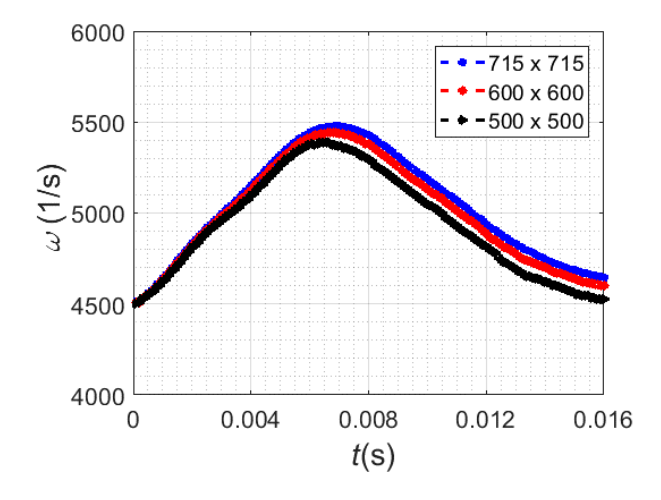


Figure A.1 Evolution of the maximum vorticity at the core center of the PV for different grid resolutions and a domain size of $0.06 \text{ m} \times 0.06 \text{ m}$.

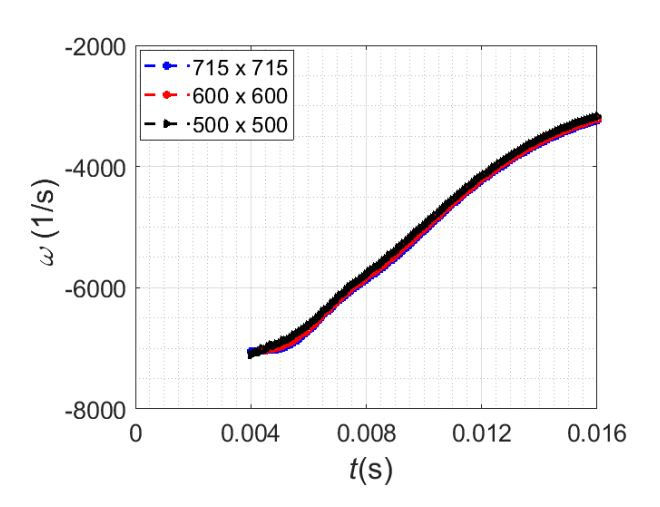


Figure A.2 Evolution of the maximum vorticity at the core center of the SV for different grid resolutions and a domain size of $0.06~\text{m} \times 0.06~\text{m}$.

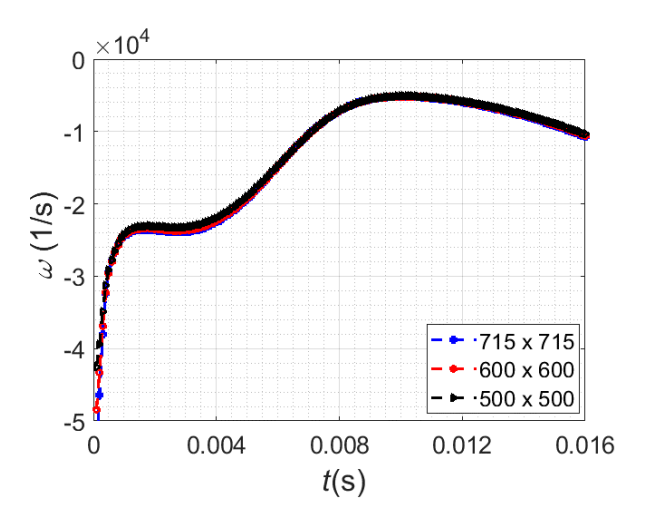


Figure A.3 Evolution of the maximum vorticity of the BL for different grid resolutions and a domain size of 0.06 m \times 0.06 m.

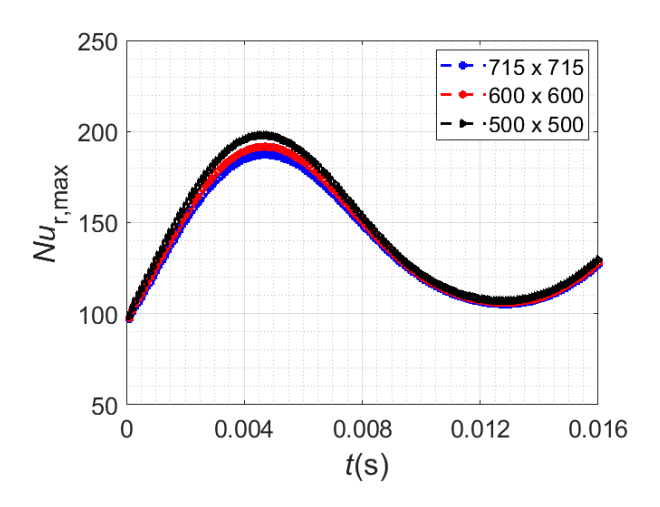


Figure A.4 Evolution of the maximum of Nu_r for different grid resolutions and a domain size 0.06 m \times 0.06 m.

In order to check the domain-size effect, computations are conducted for two different domain sizes while maintaining the same grid resolution (0.00012 m); i.e. 500×500 grid elements for a domain size 0.06 m \times 0.06 m, and 715×715 grid elements for a domain size 0.0858 m \times 0.0858 m. All other computational parameters are the same as given in section II.B. No effect is seen for increasing the domain size beyond the one used for all results in the present work (0.06 m \times 0.06 m); see Figures A.5 through A.8.

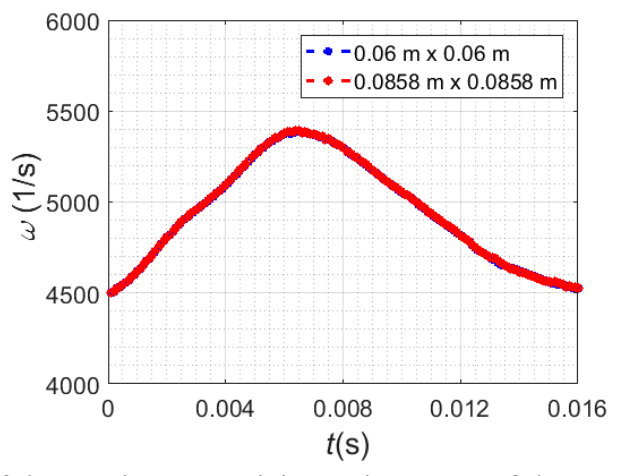


Figure A.5 Evolution of the maximum vorticity at the center of the PV for two different domain sizes while keeping the same grid resolution (0.00012 m).

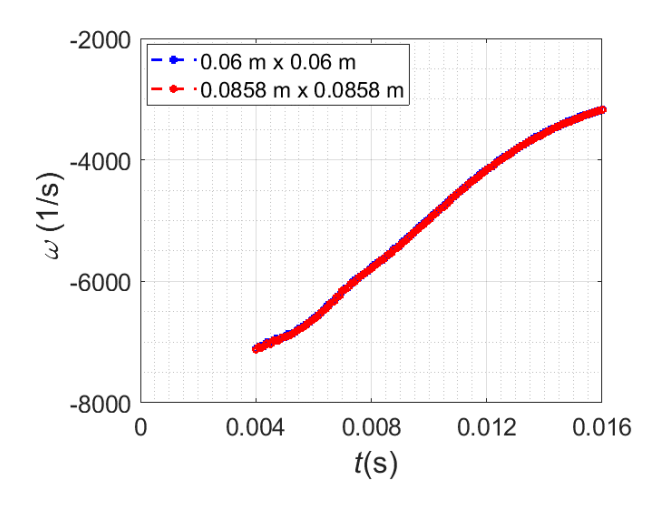


Figure A.6 Evolution of the maximum vorticity at the center of the SV for two different domain sizes while keeping the same grid resolution (0.00012 m).

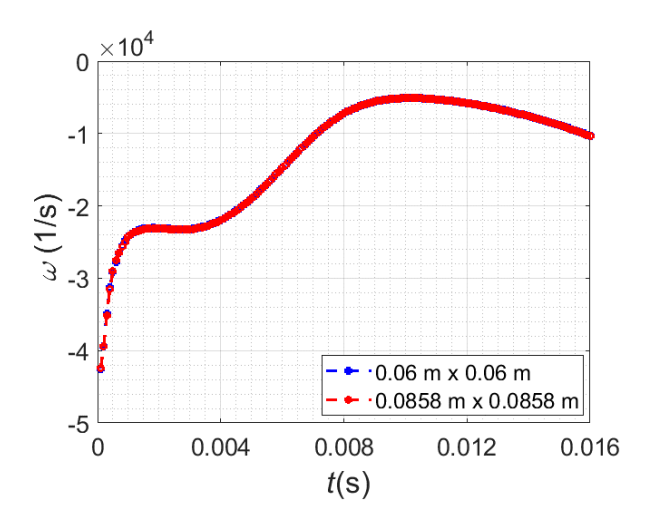


Figure A.7 Evolution of the maximum vorticity of the BL for two different domain sizes while keeping the same grid resolution (0.00012 m).

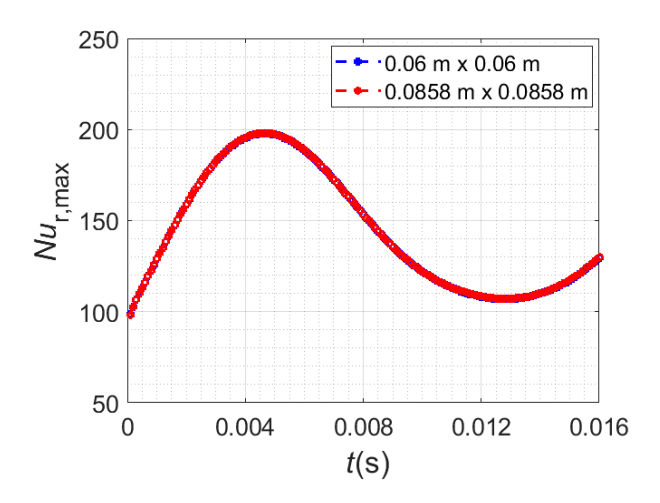


Figure A.8 Evolution of the maximum of Nu_r for two different domain sizes while keeping the same grid resolution.

Results from three time-step sizes are compared for a domain size of $0.06 \text{ m} \times 0.06 \text{ m}$, and 715×715 grid elements. All other computational parameters are the same as given in section II.B. The results, depicted in Figures A.9 through A.12, show that the time step size of 0.0001s, used for all calculations, is sufficiently small to obtain time-step independence.

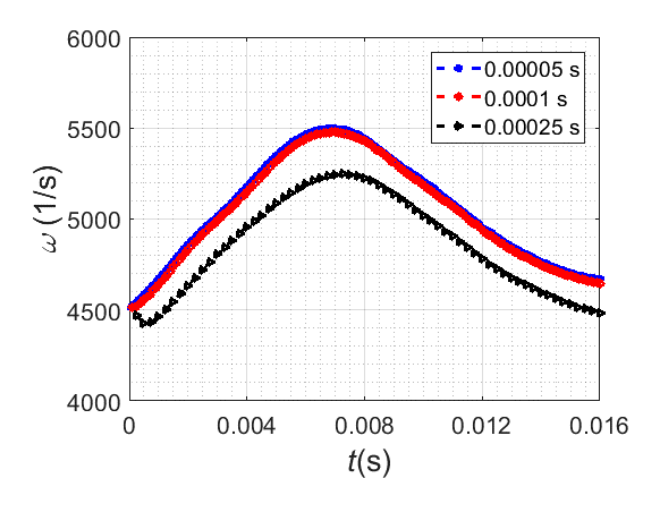


Figure A.9 Evolution of the maximum vorticity at the center of the PV for different time-step sizes, and a domain size of $0.06 \text{ m} \times 0.06 \text{ m}$ and $715 \times 715 \text{ grid elements}$.

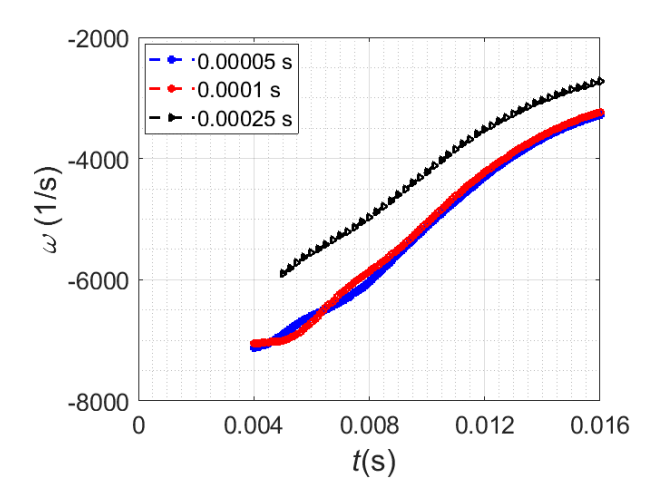


Figure A.10 Evolution of the maximum vorticity at the center of the SV for different time-step sizes, and a domain size of 0.06 m \times 0.06 m and 715 \times 715 grid elements.

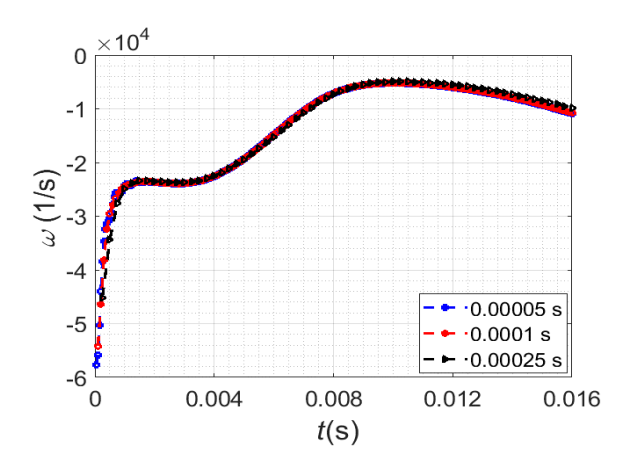


Figure A.11 Evolution of the maximum vorticity of the BL for different time-step sizes, and a domain size of $0.06 \text{ m} \times 0.06 \text{ m}$ and $715 \times 715 \text{ grid elements}$.

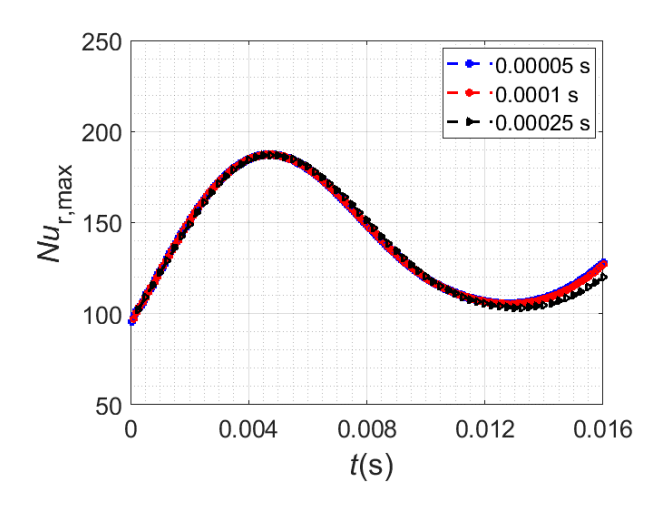


Figure A.12 Evolution of the maximum of Nu_r for different time-step sizes, and a domain size of 0.06 m × 0.06 m and 715 × 715 grid elements.

Finally, the convergence of the solution is checked by using different number of iterations (see Figures A.13 through A.16). All calculations done here utilize 200 iterations.

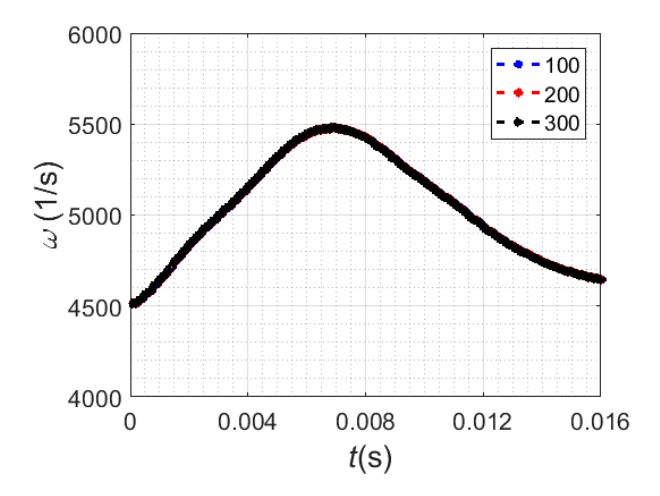


Figure A.13 Evolution of the maximum vorticity at the center of the PV for different number of iterations, and a domain size of $0.06 \text{ m} \times 0.06 \text{ m}$ and $715 \times 715 \text{ grid}$ elements. The legend shows the number of iterations.

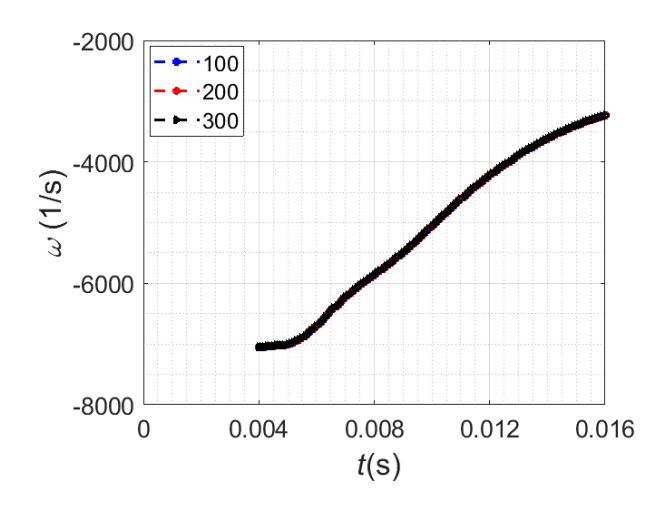


Figure A.14 Evolution of the maximum vorticity at the center of the SV for different number of iterations, and a domain size of $0.06 \text{ m} \times 0.06 \text{ m}$ and $715 \times 715 \text{ grid}$ elements. The legend shows the number of iterations.

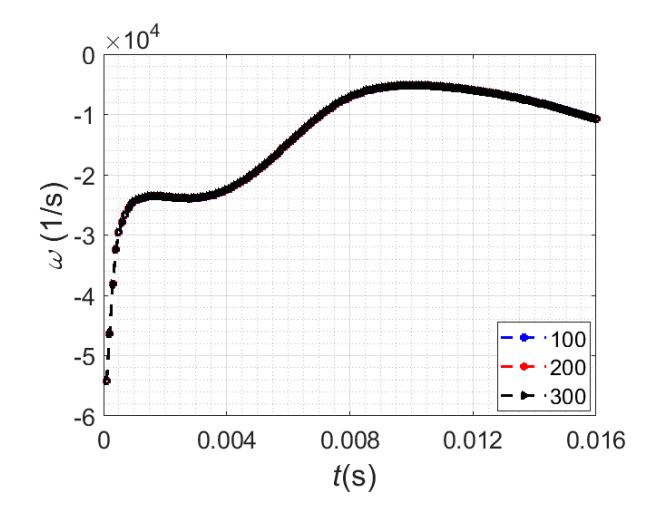


Figure A.15 Evolution of the maximum vorticity of the BL for different number of iterations, and a domain size of $0.06 \text{ m} \times 0.06 \text{ m}$ and $715 \times 715 \text{ grid}$ elements. The legend shows the number of iterations.

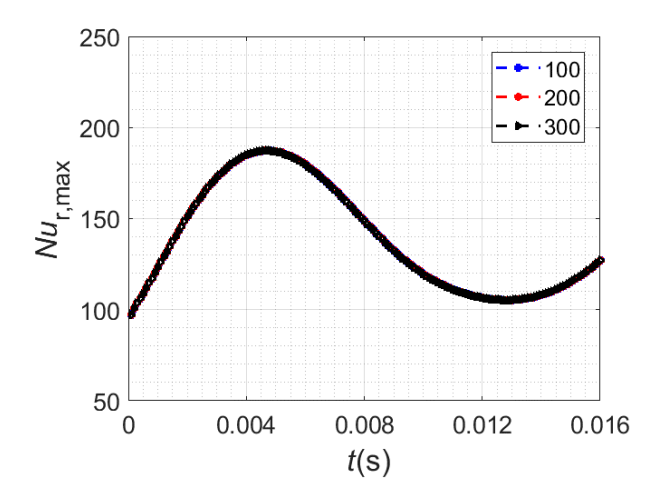
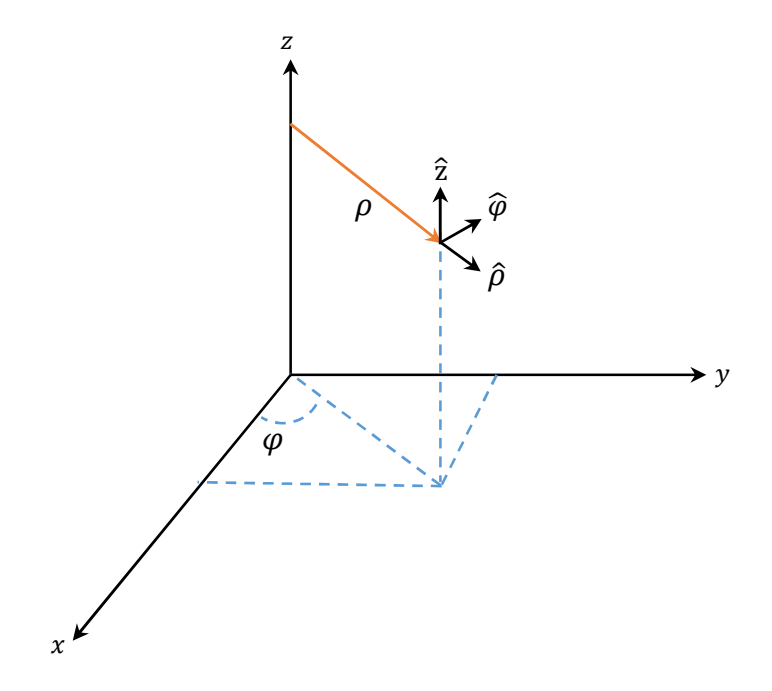


Figure A.16 Evolution of the maximum of Nu_r evolution for different number of iterations, and a domain size of 0.06 m \times 0.06 m and 715 \times 715 grid elements. The legend shows the number of iterations.

APPENDIX B: Derivation of Q Value in Cylindrical Coordinate



The transformation between the rectangular and cylindrical coordinate is shown below:

$$\rho = \sqrt{x^2 + y^2}$$

$$x = \rho \cos(\varphi)$$

$$\varphi = \arctan(\frac{y}{x})$$

$$y = \rho \sin(\varphi)$$

$$z = z$$

$$z = z$$

The unit vectors of the cylindrical coordinate are:

$$\hat{\rho} = \frac{\vec{\rho}}{\rho} = \frac{x\hat{x} + y\hat{y}}{\rho} = \hat{x}\cos(\varphi) + \hat{y}\sin(\varphi)$$

$$\hat{\varphi} = \hat{z} \times \hat{\rho} = \hat{z} \times (\hat{x}\cos(\varphi) + \hat{y}\sin(\varphi))$$

$$= \cos(\varphi) (\hat{z} \times \hat{x}) + \sin(\varphi) (\hat{z} \times \hat{y})$$

$$= \hat{y}\cos(\varphi) - \hat{x}\sin(\varphi)$$

$$\hat{z} = \hat{z}$$

The derivatives of each unit vector with respect to the other coordinate are obtained from the equations above:

$$\frac{\partial \hat{\rho}}{\partial \rho} = 0 \qquad \frac{\partial \hat{\varphi}}{\partial \rho} = 0 \qquad \frac{\partial \hat{z}}{\partial \rho} = 0$$

$$\frac{\partial \hat{\rho}}{\partial \varphi} = -\hat{x}\sin(\varphi) + \hat{y}\cos(\varphi) = \hat{\varphi} \qquad \frac{\partial \hat{\varphi}}{\partial \varphi} = -\hat{x}\cos(\varphi) - \hat{y}\sin(\varphi) = -\hat{\rho} \qquad \frac{\partial \hat{z}}{\partial \varphi} = 0$$

$$\frac{\partial \hat{\rho}}{\partial z} = 0 \qquad \frac{\partial \hat{\varphi}}{\partial z} = 0 \qquad \frac{\partial \hat{z}}{\partial z} = 0$$

The gradient of velocity vector defined as

$$\nabla \vec{V} = (\hat{\rho} \frac{\partial}{\partial \rho} + \hat{\varphi} \frac{1}{\rho} \frac{\partial}{\partial \varphi} + \hat{\rho} \frac{\partial}{\partial \rho})(u_{\rho}\hat{\rho} + u_{\varphi}\hat{\varphi} + u_{z}\hat{z}) \qquad B.1$$

$$\hat{\rho} \left[\frac{\partial}{\partial \rho} (u_{\rho}\hat{\rho}) \quad \frac{\partial}{\partial \rho} (u_{\varphi}\hat{\varphi}) \quad \frac{\partial}{\partial \rho} (u_{z}\hat{z}) \right]$$

$$\nabla \vec{V} = \frac{\hat{\varphi}}{\rho} \left[\frac{\partial}{\partial \varphi} (u_{\rho}\hat{\rho}) \quad \frac{\partial}{\partial \varphi} (u_{\varphi}\hat{\varphi}) \quad \frac{\partial}{\partial \varphi} (u_{z}\hat{z}) \right] \qquad B.2$$

$$\hat{z} \left[\frac{\partial}{\partial z} (u_{\rho}\hat{\rho}) \quad \frac{\partial}{\partial z} (u_{\varphi}\hat{\varphi}) \quad \frac{\partial}{\partial z} (u_{z}\hat{z}) \right]$$

$$\hat{\rho} \left[\left(u_{\rho} \frac{\partial \hat{\rho}}{\partial \rho} + \hat{\rho} \frac{\partial u_{\rho}}{\partial \rho} \right) \quad \left(u_{\varphi} \frac{\partial \hat{\varphi}}{\partial \rho} + \hat{\varphi} \frac{\partial u_{\varphi}}{\partial \rho} \right) \quad \left(u_{z} \frac{\partial \hat{z}}{\partial \rho} + \hat{z} \frac{\partial u_{z}}{\partial \rho} \right) \right]$$

$$= \hat{\varphi} \qquad \qquad = -\hat{\rho} \qquad 0$$

$$\nabla \vec{V} = \frac{\hat{\varphi}}{\rho} \left[\left(u_{\rho} \frac{\partial \hat{\rho}}{\partial \varphi} + \hat{\rho} \frac{\partial u_{\rho}}{\partial \varphi} \right) \quad \left(u_{\varphi} \frac{\partial \hat{\varphi}}{\partial \varphi} + \hat{\varphi} \frac{\partial u_{\varphi}}{\partial \varphi} \right) \quad \left(u_{z} \frac{\partial \hat{z}}{\partial \varphi} + \hat{z} \frac{\partial u_{z}}{\partial \varphi} \right) \right] \qquad B.3$$

$$\hat{z} \left[\left(u_{\rho} \frac{\partial \hat{\rho}}{\partial z} + \frac{\partial u_{\rho}}{\partial z} \hat{\rho} \right) \quad \left(u_{\varphi} \frac{\partial \hat{\varphi}}{\partial z} + \frac{\partial u_{\varphi}}{\partial z} \hat{\varphi} \right) \quad \left(u_{z} \frac{\partial \hat{z}}{\partial z} + \frac{\partial u_{z}}{\partial z} \hat{z} \right) \right]$$

$$\nabla \vec{V} = \begin{bmatrix} \frac{\partial u_{\rho}}{\partial \rho} \hat{\rho} \hat{\rho} & \frac{\partial u_{\varphi}}{\partial \rho} \hat{\varphi} \hat{\rho} & \frac{\partial u_{z}}{\partial \rho} \hat{\rho} \hat{z} \\ \left(\frac{1}{\rho} \frac{\partial u_{\rho}}{\partial \varphi} - \frac{u_{\varphi}}{\rho} \right) \hat{\varphi} \hat{\rho} & \left(\frac{u_{\rho}}{\rho} + \frac{\partial u_{\varphi}}{\partial \varphi} \right) \hat{\varphi} \hat{\varphi} & \frac{1}{\rho} \frac{\partial u_{z}}{\partial \varphi} \hat{\varphi} \hat{z} \\ \frac{\partial u_{\rho}}{\partial z} \hat{\rho} \hat{z} & \frac{\partial u_{\varphi}}{\partial z} \hat{\varphi} \hat{z} & \frac{\partial u_{z}}{\partial z} \hat{z} \hat{z} \end{bmatrix}$$
 B.4

$$\left(\nabla \vec{V} \right)^T = \begin{bmatrix} \frac{\partial u_{\rho}}{\partial \rho} \hat{\rho} \hat{\rho} & \left(\frac{1}{\rho} \frac{\partial u_{\rho}}{\partial \varphi} - \frac{u_{\varphi}}{\rho} \right) \hat{\varphi} \hat{\rho} & \frac{\partial u_{\rho}}{\partial z} \hat{\rho} \hat{z} \\ \frac{\partial u_{\varphi}}{\partial \rho} \hat{\varphi} \hat{\rho} & \left(\frac{u_{\rho}}{\rho} + \frac{\partial u_{\varphi}}{\partial \varphi} \right) \hat{\varphi} \hat{\varphi} & \frac{\partial u_{\varphi}}{\partial z} \hat{\varphi} \hat{z} \\ \frac{\partial u_{z}}{\partial \rho} \hat{\rho} \hat{z} & \frac{1}{\rho} \frac{\partial u_{z}}{\partial \varphi} \hat{\varphi} \hat{z} & \frac{\partial u_{z}}{\partial z} \hat{z} \hat{z} \end{bmatrix}$$
 B.5

$$:: S = \frac{1}{2} \left[\nabla \vec{V} + \left(\nabla \vec{V} \right)^T \right]$$
 B.6

$$S = \frac{1}{2} \begin{bmatrix} 2\frac{\partial u_{\rho}}{\partial \rho}\hat{\rho}\hat{\rho} & \left(\frac{1}{\rho}\frac{\partial u_{\rho}}{\partial \varphi} - \frac{u_{\varphi}}{\rho} + \frac{\partial u_{\varphi}}{\partial \rho}\right)\hat{\varphi}\hat{\rho} & \left(\frac{\partial u_{z}}{\partial \rho} + \frac{\partial u_{\rho}}{\partial z}\right)\hat{\rho}\hat{z} \\ \left(\frac{1}{\rho}\frac{\partial u_{\rho}}{\partial \varphi} - \frac{u_{\varphi}}{\rho} + \frac{\partial u_{\varphi}}{\partial \rho}\right)\hat{\varphi}\hat{\rho} & 2\left(\frac{u_{\rho}}{\rho} + \frac{\partial u_{\varphi}}{\partial \varphi}\right)\hat{\varphi}\hat{\varphi} & \left(\frac{1}{\rho}\frac{\partial u_{z}}{\partial \varphi} + \frac{\partial u_{\varphi}}{\partial z}\right)\hat{\varphi}\hat{z} \\ \left(\frac{\partial u_{z}}{\partial \rho} + \frac{\partial u_{\rho}}{\partial z}\right)\hat{\rho}\hat{z} & \left(\frac{1}{\rho}\frac{\partial u_{z}}{\partial \varphi} + \frac{\partial u_{\varphi}}{\partial z}\right)\hat{\varphi}\hat{z} & 2\frac{\partial u_{z}}{\partial z}\hat{z}\hat{z} \end{bmatrix}$$

..... B.7

$$: \Omega = \frac{1}{2} \left[\nabla \vec{V} - (\nabla \vec{V})^T \right]$$
 B.8

$$\Omega = \frac{1}{2} \begin{bmatrix} 0 & \left(\frac{u_{\varphi}}{\rho} - \frac{1}{\rho} \frac{\partial u_{\rho}}{\partial \varphi} + \frac{\partial u_{\varphi}}{\partial \rho}\right) \hat{\varphi} \hat{\rho} & \left(\frac{\partial u_{z}}{\partial \rho} - \frac{\partial u_{\rho}}{\partial z}\right) \hat{\rho} \hat{z} \\ -\left(\frac{u_{\varphi}}{\rho} - \frac{1}{\rho} \frac{\partial u_{\rho}}{\partial \varphi} + \frac{\partial u_{\varphi}}{\partial \rho}\right) \hat{\varphi} \hat{\rho} & 0 & \left(\frac{1}{\rho} \frac{\partial u_{z}}{\partial \varphi} - \frac{\partial u_{\varphi}}{\partial z}\right) \hat{\varphi} \hat{z} \\ -\left(\frac{\partial u_{z}}{\partial \rho} + \frac{\partial u_{\rho}}{\partial z}\right) \hat{\rho} \hat{z} & -\left(\frac{1}{\rho} \frac{\partial u_{z}}{\partial \varphi} - \frac{\partial u_{\varphi}}{\partial z}\right) \hat{\varphi} \hat{z} & 0 \end{bmatrix}$$

..... В.9

For (ρ, z) plane

$$S = \frac{1}{2} \begin{bmatrix} 2\frac{\partial u_{\rho}}{\partial \rho}\hat{\rho}\hat{\rho} & 0 & \left(\frac{\partial u_{z}}{\partial \rho} + \frac{\partial u_{\rho}}{\partial z}\right)\hat{z}\hat{\rho} \\ 0 & 2\left(\frac{u_{\rho}}{\rho}\right)\hat{\varphi}\hat{\varphi} & 0 \\ \left(\frac{\partial u_{z}}{\partial \rho} + \frac{\partial u_{\rho}}{\partial z}\right)\hat{\rho}\hat{z} & 0 & 2\frac{\partial u_{z}}{\partial z}\hat{z}\hat{z} \end{bmatrix} \dots B.10$$

$$\Omega = \frac{1}{2} \begin{bmatrix} 0 & 0 & \left(\frac{\partial u_z}{\partial \rho} - \frac{\partial u_\rho}{\partial z}\right) \hat{\rho} \hat{z} \\ 0 & 0 & 0 \\ -\left(\frac{\partial u_z}{\partial \rho} - \frac{\partial u_\rho}{\partial z}\right) \hat{\rho} \hat{z} & 0 & 0 \end{bmatrix} \qquad \dots \dots B.11$$

The Euclidean norm of *S* given below:

$$||S||^2 = \left[\left(\frac{\partial u_{\rho}}{\partial \rho} \right)^2 + \left(\frac{u_{\rho}}{\rho} \right)^2 + \left(\frac{\partial u_z}{\partial z} \right)^2 + 2 \left(\frac{1}{2} \frac{\partial u_z}{\partial \rho} + \frac{1}{2} \frac{\partial u_{\rho}}{\partial z} \right)^2 \right] \qquad \dots B.12$$

$$\therefore 2\left(\frac{1}{2}\frac{\partial u_z}{\partial \rho} + \frac{1}{2}\frac{\partial u_\rho}{\partial z}\right)^2 = 2\left[\left(\frac{1}{2}\frac{\partial u_z}{\partial \rho}\right)^2 + \left(\frac{1}{2}\frac{\partial u_\rho}{\partial z}\right)^2 + \frac{1}{2}\frac{\partial u_z}{\partial \rho}\frac{\partial u_\rho}{\partial z}\right] \qquad ... B.13$$

$$\|\Omega\|^2 = \left[\left(-\frac{1}{2} \frac{\partial u_z}{\partial \rho} + \frac{1}{2} \frac{\partial u_\rho}{\partial z} \right)^2 + \left(\frac{1}{2} \frac{\partial u_z}{\partial \rho} - \frac{1}{2} \frac{\partial u_\rho}{\partial z} \right)^2 \right] \qquad ... B.15$$

$$\|\Omega\|^2 = \left[\frac{1}{2} \left(\frac{\partial u_z}{\partial \rho} \right)^2 + \frac{1}{2} \left(\frac{\partial u_\rho}{\partial z} \right)^2 - \frac{\partial u_z}{\partial \rho} \frac{\partial u_\rho}{\partial z} \right]$$
 B.16

$$Q = \frac{1}{2} [\|\Omega\|^2 - \|S\|^2]$$
 B.17

$$Q = \frac{-1}{2} \left[\left(\frac{\partial u_{\rho}}{\partial \rho} \right)^{2} + \left(\frac{u_{\rho}}{\rho} \right)^{2} + \left(\frac{\partial u_{z}}{\partial z} \right)^{2} + 2 \frac{\partial u_{z}}{\partial \rho} \frac{\partial u_{\rho}}{\partial z} \right]$$
 B.18

APPENDIX C: 1D Model Solution

Define the normalized temperature

$$\theta = \frac{T(t,z) - T_w}{T_\infty - T_W}$$

1.Steady state solution for 1D energy equation

B.c's
$$z = 0 \rightarrow \theta_o = 0$$
,

$$z \to \infty \to \theta_0 = 1$$

$$u_z \frac{\partial \theta}{\partial z} = \alpha \frac{\partial^2 \theta}{\partial z^2}$$
 C1.1

where $u_z = -v_o$

Assume
$$\theta = e^{mz} \rightarrow \frac{\partial \theta}{\partial z} = m e^{mz}$$
 C1.2

$$\frac{\partial^2 \theta}{\partial z^2} = m^2 e^{mz}$$
 C1.3

Substitute equations C.2 and C.3 in C.1

$$-v_o m e^{mz} = \alpha m^2 e^{mz}$$

$$(-v_0 m - \alpha m^2)e^{mz} = 0$$

$$-v_o m - \alpha m^2 = 0$$

$$m(-v_o - \alpha m) = 0$$

Result in two solution $\rightarrow m = 0$, and $m = \frac{-v_0}{\alpha}$

where C_1 and C_2 are constants. Apply the B.c's into equation C1.4

at
$$z = 0 \rightarrow C_1 = -C_2$$

at
$$z \to \infty$$
 $\to \theta = 1 = -C_2 e^{-\infty} + C_2 \to C_1 = -1$, $C_2 = 1$

$$\bullet \quad \theta_o = 1 - e^{\frac{-\nu_o}{\alpha}Z}$$
 C1.5

2. Unsteady state solution for 1D energy equation with perturbation

Assume the solution of the unsteady energy equation with perturbation is in the form of series expression and up to the first order of ε

where $\varepsilon << 1$ and $\neq 0$, θ_1 is the first order solution, ω is the angular frequency and t is the time with B.c's z=0 $\rightarrow \theta_1=0$,

$$z \to \infty \to \theta_1 = 0$$

the equation C2.2 below is the solution of the 1D, z-momentum equation.

$$u_z(t) = -v_o(1 + \varepsilon e^{i\omega t})$$
 C2.2

by substitute equations C2.1 and C2.2 into the 1D normalized unsteady energy equation (C2.3)

$$\frac{\partial \theta}{\partial t} + u_z(t) \frac{\partial \theta}{\partial z} = \alpha \frac{\partial^2 \theta}{\partial z^2}$$
 C2.3

this leads to

$$i\varepsilon\omega\,\theta_1e^{i\omega t}+(-v_o(1+\varepsilon\,e^{i\omega t}\,))(\frac{\partial\theta_0}{\partial z}+\varepsilon\,e^{i\omega t}\,\frac{\partial\theta_1}{\partial z})\,=\,\alpha\,(\frac{\partial^2\theta_0}{\partial z^2}+\varepsilon\,e^{i\omega t}\,\frac{\partial^2\theta_1}{\partial z^2})\quad\dots\dots$$
C2.4

by collecting the term of $O(\varepsilon)$ and neglect the higher order term of ε , and keep in mind the other remaining term will give the steady state solution.

$$i\omega \theta_1 - v_o \frac{\partial \theta_0}{\partial z} - v_o \frac{\partial \theta_1}{\partial z} - \alpha \frac{\partial^2 \theta_1}{\partial z^2} = 0$$
 C2.6

$$\frac{\partial^2 \theta_1}{\partial z^2} + \frac{v_o}{\alpha} \frac{\partial \theta_1}{\partial z} - i \frac{\omega}{\alpha} \theta_1 = -\frac{v_o}{\alpha} \frac{\partial \theta_0}{\partial z}$$
 C2.7

$$\because \frac{\partial \theta_o}{\partial z} = \frac{v_o}{\alpha} e^{\frac{-v_o}{\alpha}z} \quad \text{form equation C1.5. Substitute into equation C2.7}$$

$$\frac{\partial^2 \theta_1}{\partial z^2} + \frac{v_o}{\alpha} \frac{\partial \theta_1}{\partial z} - i \frac{\omega}{\alpha} \theta_1 = -\frac{v_o^2}{\alpha^2} e^{\frac{-v_o}{\alpha} z}$$
 C2.8

equation C2.8 is a non-Homogenous PDE and the solution is

where θ_H and θ_P is the homogenous and particular solutions of PDE respectively.

by starting with the homogenous solution,

$$\frac{\partial^2 \theta}{\partial z^2} = m^2 e^{mz} \qquad C2.11$$

substitute equation C2.10 and C2.11 into homogenous part of equation C2.8, will results

$$m^2 e^{mz} + \frac{v_o}{\alpha} m e^{mz} - i \frac{\omega}{\alpha} e^{mz} = 0$$

$$\left(m^2 + \frac{v_o}{\alpha} m - i \frac{\omega}{\alpha}\right) e^{mz} = 0$$

$$m^2 + \frac{v_o}{\alpha} m - i \frac{\omega}{\alpha} = 0$$
 C2.12

Solve equation C2.12 for *m*

$$m = \frac{-\frac{v_o}{\alpha} \pm \sqrt{(\frac{v_o}{\alpha})^2 + 4\frac{\omega}{\alpha}i}}{2}$$

$$m = -\frac{v_o}{2\alpha} \pm \frac{1}{2\alpha} \sqrt{v_o^2 + 4\alpha\omega i}$$
 C2.13

let
$$\widehat{\omega} = \frac{4\alpha\omega}{v_o^2} = \frac{4\alpha\omega}{\frac{\alpha^2}{\alpha^2}v_o^2} = \frac{4\omega l_o^2}{\alpha}$$
 C2.14

where
$$l_o = \frac{\alpha}{v_o}$$

$$\therefore m = -\frac{1}{2l_0} \pm \frac{1}{2l_0} \sqrt{1 + \widehat{\omega}i}$$
 C2.15

let
$$\sqrt{1+\widehat{\omega}i} = \sqrt{a+bi} = p+qi$$

 $a+bi = (p+qi)^2$
 $a+bi = p^2 + 2pai - a^2$

find q from equation C2.17 and substitute it in equation C2.16

$$p^4 - ap^2 - \frac{1}{4}b^2 = 0 C2.18$$

solving equation C2.16 to find p

$$p^2 = \frac{a \pm \sqrt{a^2 + b^2}}{2} = \sqrt{\frac{a^2 \pm \sqrt{a^2 + b^2}}{2}}$$

$$\therefore p^2 = \sqrt{\frac{a^2 + \sqrt{a^2 + b^2}}{2}}$$
; ignoring the minus sign inside the square root since p must be a real number

$$\therefore p = \pm \sqrt{\frac{a^2 + \sqrt{a^2 + b^2}}{2}} = \pm \sqrt{\frac{1 + \sqrt{1 + (\widehat{\omega})^2}}{2}} = \pm \Omega^*$$
 C2.19

$$q = \frac{b}{2p} = \frac{\widehat{\omega}}{\pm 2\sqrt{\frac{1 + \sqrt{1 + (\widehat{\omega})^2}}{2}}} = \pm \frac{\widehat{\omega}}{2\Omega^*}$$
 C2.20

substitute p and q in equation C2.15

$$m = -\frac{1}{2l_o} \pm \frac{1}{2l_o} \left(\pm \Omega^* \pm \frac{\widehat{\omega}}{2 \Omega^*} i \right)$$
 C2.21

since $\widehat{\omega} > 0 \rightarrow p$ and q must be the same sign, this will reduce the solution to two roots only

$$m_{2} = -\frac{1}{2l_{o}} - \frac{1}{2l_{o}} \Omega^{*} - i \frac{1}{4l_{o}} \frac{\widehat{\omega}}{\Omega^{*}} = \frac{-1}{2l_{o}} (\Omega^{*} + 1) - i \frac{1}{4l_{o}} \frac{\widehat{\omega}}{\Omega^{*}} \qquad \cdots$$
 C2.23

$$: \theta_H = C_3 e^{m_1 z} + C_4 e^{m_2 z}$$
 C2.24

where C_3 and C_4 are constants

$$\theta_H = C_3 e^{\frac{1}{2l_o}(\Omega^* - 1)z} e^{i\frac{1}{4l_o\Omega^*}z} + C_4 e^{\frac{-1}{2l_o}(\Omega^* + 1)z} e^{-i\frac{1}{4l_o\Omega^*}z} \qquad \dots$$
 C2.25

$$\theta_{H} = C_{3} e^{\frac{1}{2l_{o}}(\Omega^{*}-1)z} \left[cos\left(\frac{1}{4l_{o}}\frac{\widehat{\omega}}{\Omega^{*}}z\right) + i sin\left(\frac{1}{4l_{o}}\frac{\widehat{\omega}}{\Omega^{*}}z\right) \right] \dots$$

let $z^* = \frac{z}{4l_o}$, and substitute in equation C2.26. this will lead to

$$\theta_H = C_3 \, e^{2(\Omega^*-1)z^*} \left[\cos \left(\frac{\widehat{\omega}}{\Omega^*} z^* \right) + i \, \sin \left(\frac{\widehat{\omega}}{\Omega^*} z^* \right) \right] \, \dots$$

... +
$$C_4 e^{-2(\Omega^*+1)z^*} \left[cos\left(\frac{\widehat{\omega}}{\Omega^*}z^*\right) - i sin\left(\frac{\widehat{\omega}}{\Omega^*}z^*\right) \right]$$
 C2.27

For the particular solution,

$$\rightarrow \frac{\partial \theta_P}{\partial z} = -A \frac{v_o}{\alpha} e^{\frac{-v_o}{\alpha}z} \qquad C2.29$$

$$\rightarrow \frac{\partial^2 \theta_P}{\partial z^2} = A \frac{v_o^2}{\alpha^2} e^{\frac{-v_o}{\alpha}z}$$
 C2.30

substitute equations C2.28, C2.29 and C2.30 into equation C2.8

$$A\frac{v_o^2}{\alpha^2}e^{\frac{-v_o}{\alpha}z} + \frac{v_o}{\alpha}(-A\frac{v_o}{\alpha}e^{\frac{-v_o}{\alpha}z}) - i\frac{\omega}{\alpha}Ae^{\frac{-v_o}{\alpha}z} = -\frac{v_o^2}{\alpha^2}e^{\frac{-v_o}{\alpha}z} \qquad \cdots$$
 C2.31

rearrange equations C2.30 and solve for A

$$A\left(\frac{v_o^2}{\alpha^2} - \frac{v_o^2}{\alpha^2} - i\frac{\omega}{\alpha}\right) = -\frac{v_o^2}{\alpha^2} \rightarrow A = \frac{v_o^2}{\alpha \omega i}$$

$$A = \frac{v_o^2}{\alpha \omega i} \times \frac{-\alpha \omega i}{-\alpha \omega i} = \frac{-v_o^2}{\alpha \omega} i \qquad C2.32$$

$$\therefore \theta_P = \frac{-v_0^2}{\alpha \omega} i \ e^{\frac{-v_0}{\alpha} z}$$
 C2.33

substitute equation C2.27 and C.34 into equation C2.9, will lead to

apply the 1st B.c $(z \to \infty \to \theta_1(z) = 0 \to \theta_1(z^*) = 0)$ in equation C2.35 will lead to $C_3 = 0$

because
$$\Omega^* \ge 1$$
 , and $(\Omega^*-1) \ge 0 \to e^{2(\Omega^*-1)z^*} = \infty$ for $(\Omega^*-1) > 0$
$$= 1 \text{ for } (\Omega^*-1) = 0$$

thus; equation C2.35 become

$$\theta_1 = C_4 e^{-2(\Omega^* + 1)z^*} \left[\cos \left(\frac{\widehat{\omega}}{\Omega^*} z^* \right) - i \sin \left(\frac{\widehat{\omega}}{\Omega^*} z^* \right) \right] - \frac{4i}{\widehat{\omega}} e^{-4z^*} \quad \dots \quad C2.36$$

apply the 2nd B.c $(z = 0 \rightarrow \theta_1(z) = 0 \rightarrow \theta_1(z^*) = 0)$ in equation C2.36 will lead to

$$0 = C_4 - \frac{4i}{\widehat{\omega}} \to C_4 = \frac{4i}{\widehat{\omega}}$$

$$\therefore \theta_1 = \frac{4i}{\widehat{\omega}} e^{-2(\Omega^* + 1)z^*} \left[\cos \left(\frac{\widehat{\omega}}{\Omega^*} z^* \right) - i \sin \left(\frac{\widehat{\omega}}{\Omega^*} z^* \right) \right] - \frac{4i}{\widehat{\omega}} e^{-4z^*} \quad \dots \dots \quad C2.37$$

let
$$t^* = \frac{\alpha t}{4l_o^2}$$
, and from equation C2.14 $\widehat{\omega} = \frac{4\omega l_o^2}{\alpha}$, substitute into equation C2.38

substitute equation C2.37 and C2.39 will result

$$\therefore \ \theta_1 = \theta_1 \ e^{i\omega^*t^*} = \theta_1 [\cos(\widehat{\omega}t^*) + i \sin(\widehat{\omega}t^*)] \qquad \cdots$$
 C2.39

simplify equation C2.40 and take the only real part of Θ

$$\theta_{1} = \frac{4}{\widehat{\omega}} e^{-2(\Omega^{*}+1)z^{*}} sin\left(\frac{\widehat{\omega}}{\Omega^{*}}z^{*}\right) cos(\widehat{\omega}t^{*}) - \frac{4}{\widehat{\omega}} e^{-2(\Omega^{*}+1)z^{*}} cos\left(\frac{\widehat{\omega}}{\Omega^{*}}z^{*}\right) sin(\widehat{\omega}t^{*})...$$

$$... + \frac{4}{\widehat{\omega}} e^{-4z^{*}} sin(\widehat{\omega}t^{*}) \qquad \qquad C2.41$$

rearrange equation C2.41

$$\theta_{1} = \frac{4}{\widehat{\omega}} \left[e^{-4z^{*}} - e^{-2(\Omega^{*}+1)z^{*}} cos\left(\frac{\widehat{\omega}}{\Omega^{*}}z^{*}\right) \right] sin(\widehat{\omega}t^{*}) \dots$$

$$\dots + \frac{4}{\widehat{\omega}} e^{-2(\Omega^{*}+1)z^{*}} sin\left(\frac{\widehat{\omega}}{\Omega^{*}}z^{*}\right) cos(\widehat{\omega}t^{*}) \dots C2.42$$
let
$$\theta_{1} = A(\widehat{\omega}, z^{*}) sin(\widehat{\omega}t^{*}) + B(\widehat{\omega}, z^{*}) cos(\widehat{\omega}t^{*}) \dots C2.43$$

$$\rightarrow \quad \theta_{1} = \mathcal{A}(\widehat{\omega}, z^{*}) cos(\widehat{\omega}t^{*} - \Phi(\widehat{\omega}, z^{*})) \dots C2.44$$
where
$$A(\widehat{\omega}, z^{*}) = \frac{4}{\widehat{\omega}} \left[e^{-4z^{*}} - \frac{4}{\widehat{\omega}} e^{-2(\Omega^{*}+1)z^{*}} cos\left(\frac{\widehat{\omega}}{\Omega^{*}}z^{*}\right) \right]$$

$$B(\widehat{\omega}, z^{*}) = \frac{4}{\widehat{\omega}} e^{-2(\Omega^{*}+1)z^{*}} sin\left(\frac{\widehat{\omega}}{\Omega^{*}}z^{*}\right)$$

$$\mathcal{A}(\widehat{\omega}, z^{*}) = \sqrt{A(\widehat{\omega}, z^{*})^{2} + B(\widehat{\omega}, z^{*})^{2}}$$

$$\Phi(\widehat{\omega}, z^{*}) = tan^{-1} \left(\frac{A(\widehat{\omega}, z^{*})^{2}}{B(\Omega, z^{*})}\right)$$

where $\mathcal{A}(\widehat{\omega}, z^*)$ and $\Phi(\widehat{\omega}, z^*)$ are the amplitude and the phase shift of Θ_1 now, take the derivative of Θ_1 with respect to z^* using equation C2.42

$$\frac{d\theta_{1}}{dz^{*}} = \frac{4}{\widehat{\omega}} \left[-4e^{-4z^{*}} - \frac{\widehat{\omega}}{\Omega^{*}} e^{-2(\Omega^{*}+1)z^{*}} \left(-\sin\left(\frac{\widehat{\omega}}{\Omega^{*}}z^{*}\right) \right) \dots \right]$$

$$\dots - (-2(\Omega^{*}+1))e^{-2(\Omega^{*}+1)z^{*}} \cos\left(\frac{\widehat{\omega}}{\Omega^{*}}z^{*}\right) \left[\sin(\widehat{\omega}t^{*}) \dots \right]$$

$$\dots + \frac{4}{\widehat{\omega}} \left[\frac{\widehat{\omega}}{\Omega^{*}} e^{-2(\Omega^{*}+1)z^{*}} \cos\left(\frac{\widehat{\omega}}{\Omega^{*}}z^{*}\right) \dots \right]$$

$$\dots + (-2(\Omega^{*}+1))e^{-2(\Omega^{*}+1)z^{*}} \sin\left(\frac{\widehat{\omega}}{\Omega^{*}}z^{*}\right) \left[\cos(\widehat{\omega}t^{*}) \right]$$

$$\dots + (-2(\Omega^{*}+1))e^{-2(\Omega^{*}+1)z^{*}} \sin\left(\frac{\widehat{\omega}}{\Omega^{*}}z^{*}\right) \left[\cos(\widehat{\omega}t^{*}) \right]$$

$$\dots + (-2(\Omega^{*}+1))e^{-2(\Omega^{*}+1)z^{*}} \sin\left(\frac{\widehat{\omega}}{\Omega^{*}}z^{*}\right) \left[\cos(\widehat{\omega}t^{*}) \right]$$

now find the derivative of $\frac{d\theta_1}{dz^*}$ at $z^* = 0$ using equation C2.45

$$\rightarrow \frac{d\theta_{1}}{dz^{*}}\Big|_{z^{*}=0} = \left[\frac{-16}{\widehat{\omega}} + \frac{8(\Omega^{*} + 1)}{\widehat{\omega}}\right] sin(\widehat{\omega}t^{*}) + \frac{4}{\Omega^{*}} cos(\widehat{\omega}t^{*})$$

$$C2.46$$

$$\frac{d\theta_{1}}{dz^{*}}\Big|_{z^{*}=0} = C(\widehat{\omega}) sin(\widehat{\omega}t^{*}) + D(\widehat{\omega}) cos(\widehat{\omega}t^{*})$$

$$C2.47$$

$$\frac{d\theta_{1}}{dz^{*}}\Big|_{z^{*}=0} = \tilde{\mathcal{A}}(\widehat{\omega}) cos(\widehat{\omega}t^{*} - \tilde{\boldsymbol{\Phi}}(\widehat{\omega}))$$

$$C2.48$$

where
$$C(\widehat{\omega}) = \left[\frac{-16}{\widehat{\omega}} + \frac{8(\Omega^* + 1)}{\widehat{\omega}}\right]$$

$$D(\widehat{\omega}) = \frac{4}{\Omega^*}$$

$$\widetilde{\mathcal{A}}(\widehat{\omega}) = \sqrt{C(\widehat{\omega})^2 + D(\widehat{\omega})^2}$$

$$\widetilde{\Phi}(\widehat{\omega}) = tan^{-1}\left(\frac{C(\widehat{\omega})}{D(\widehat{\omega})}\right)$$

Where $\tilde{\mathcal{A}}(\widehat{\omega})$ and $\tilde{\Phi}(\widehat{\omega})$ are the amplitude and the phase shift of $\frac{d\theta_1}{dz^*}\Big|_{z^*=0}$

BIBLIOGRAPHY

BIBLIOGRAPHY

- 1. Jambunathan, K., Moss, M. A. and Button, B. L. (1992). A review of heat transfer data for single circular jet impingement. *International Journal of Heat and Fluid Flow*, 13(2), 106-115.
- 2. Carlomagno, G. M. and Ianiro, A. (2014). Thermo-fluid-dynamics of submerged jets impinging at short nozzle-to-plate distance: a review. *Experimental thermal and fluid science*, 58, 15-35.
- 3. Drubka, R. E., Reisenthel, P., & Nagib, H. M. (1989). The dynamics of low initial disturbance turbulent jets. *Physics of Fluids A: Fluid Dynamics*, *1*(10), 1723-1735.
- 4. Drazin, P. G., & Reid, W. H. (2004). *Hydrodynamic stability*. Cambridge university press.
- 5. Michalke, A. (1972). The instability of free shear layers. *Progress in Aerospace Sciences*, *12*, 213-216.
- 6. Popiel, C. O. and Trass, O. (1991). Visualization of a free and impinging round jet. *Experimental Thermal and Fluid Science*, 4(3), 253-264.
- 7. Ho, C. M., & Huang, L. S. (1982). Subharmonics and vortex merging in mixing layers. *Journal of Fluid Mechanics*, 119, 443-473.
- 8. Walker, J. D. A., Smith, C. R., Cerra, A. W., & Doligalski, T. L. (1987). The impact of a vortex ring on a wall. *Journal of Fluid Mechanics*, *181*, 99-140.
- 9. Glezer, A., & Amitay, M. (2002). Synthetic jets. *Annual review of fluid mechanics*, 34(1), 503-529.
- 10. Greco, C. S., Cardone, G. and Soria, J. (2017). On the behavior of impinging zero-net-mass-flux jets. *Journal of Fluid Mechanics*, 810, 25-59.
- 11. Doligalski, T. L., & Walker, J. D. A. (1984). The boundary layer induced by a convected two-dimensional vortex. *Journal of Fluid Mechanics*, *139*, 1-28.
- 12. Fabris, D., Liepmann, D. and Marcus, D. (1996). Quantitative experimental and numerical investigation of a vortex ring impinging on a wall. *Physics of Fluids*, 8(10), 2640-2649.
- 13. Orlandi, P., & Verzicco, R. (1993). Vortex rings impinging on walls: axisymmetric and three-dimensional simulations. *Journal of Fluid Mechanics*, *256*, 615-646.

- 14. Gendrich, C., Bohl, D., Koochesfahani, M., Gendrich, C., Bohl, D. and Koochesfahani, M. (1997). Whole-field measurements of unsteady separation in a vortex ring/wall interaction. 28th AIAA Fluid Dynamics Conference. *AIAA paper 97-1780*.
- 15. Martin, R. and Zenit, R. (2008). Heat transfer resulting from the interaction of a vortex pair with a heated wall. *Journal of Heat Transfer*, 130(5), 051701.
- 16. Reulet, P., Marchand, M. and Millan, P. (1998). Experimental characterization of the convective heat transfer in a vortex-wall interaction. *Revue Générale de Thermique*, 37(8), 661-668.
- 17. Cassel, K. W. (2001). The effect of convective heat transfer on unsteady boundary-layer separation. *Journal of Fluid Mechanics*, 428, 107-131.
- 18. Chung, Y. M., & Luo, K. H. (2002). Unsteady heat transfer analysis of an impinging jet. *Journal of heat transfer*, 124(6), 1039-1048.
- 19. Hadžiabdić, M. and Hanjalić, K. (2008). Vortical structures and heat transfer in around impinging jet. *Journal of Fluid Mechanics*, 596, 221-260.
- 20. Pavolva, A. and Amitay, M. (2006). Electronic cooling using synthetic jet impingement. *Journal of Heat Transer*, 128(9), 897-907.
- 21. Greco, C. S., Paolillo, G., Ianiro, A., Cardone, G. and de Luca, L. (2018). Effects of the stroke length and nozzle-to-plate distance on synthetic jet impingement heat transfer. *International Journal of Heat and Mass Transfer*, 117, 1019-1031.
- 22. Hubble, D.O., Vlachos, P.P. and Diller, T.E. (2013). The role of large-scale vortical structures in transient convective heat transfer augmentation. *Journal of Fluid Mechanics*, 718, 89-115.
- 23. Al-Aweni, M. O. (2013). Simultaneous flow visualization and unsteady-surface-pressure measurements in normal and oblique impinging jets. *Doctoral Dissertation*, Michigan State University, East Lansing, Michigan, USA.
- 24. Yule, A. J. (1978). Large-scale structure in the mixing layer of a round jet. *Journal of Fluid Mechanics*, 89(3), 413-432.
- 25. Kataoka, K., Suguro, M., Degawa, H., Maruo, K. and Mihata, I. (1987). The effect of surface renewal due to largescale eddies on jet impingement heat transfer. *International Journal of Heat and Mass Transfer*, 30(3), 559-567.

- 26. Violato, D., Ianiro, A., Cardone, G. and Scarano, F. (2012). Three-dimensional vortex dynamics and convective heat transfer in circular and chevron impinging jets. *International Journal of Heat and Fluid Flow*, 37, 22-36.
- 27. Schram, C. F. (2003). Aeroacoustics of subsonic jets: prediction of the sound produced by vortex pairing based on particle image velocimetry. PhD. Thesis. Eindhoven University of Technology.
- 28. Didden, N. and Ho, C. M. (1985). Unsteady separation in a boundary layer produced by an impinging jet. *Journal of Fluid Mechanics*, 160, 235-256.
- 29. Fornberg, B. (1988). Generation of finite difference formulas on arbitrarily spaced grids. *Mathematics of computation*, 51(184), 699-706.
- 30. Shrikhande, G. (2012). Assessment of Taylor-series Model for Estimation of Vortex Flows Using Surface Stress Measurements. *Master thesis*, Michigan State University, East Lansing, Michigan, USA.
- 31. Incropera, F. P. and DeWitt, D. P. (2007). Fundamentals of heat and mass transfer. J. Wiley, New York.
- 32. Hunt, J. C., Wray, A. A., & Moin, P. (1988). Eddies, streams, and convergence zones in turbulent flows.
- 33. Jeong, J., & Hussain, F. (1995). On the identification of a vortex. *Journal of fluid mechanics*, 285, 69-94.
- 34. Schlichting, H., & Gersten, K. (2016). Boundary-layer theory. Springer.
- 35. Lighthill, M. J. (1954). The response of laminar skin friction and heat transfer to fluctuations in the stream velocity. *Proceedings of the Royal Society of London. Series A. Mathematical and Physical Sciences*, 224(1156), 1-23.
- 36. Stuart, J. T. (1955). A solution of the Navier-Stokes and energy equations illustrating the response of skin friction and temperature of an infinite plate thermometer to fluctuations in the stream velocity. *Proceedings of the Royal Society of London. Series A. Mathematical and Physical Sciences*, 231(1184), 116-130.
- 37. Watson, J. (1958). A solution of the Navier–Stokes equations illustrating the response of a laminar boundary layer to a given change in the external stream velocity. *The Quarterly Journal of Mechanics and Applied Mathematics*, 11(3), 302-325.

38. Nix, A. C., Diller, T. E., & Ng, W. F. (2007). Experimental measurements and modeling of the effects of large-scale freestream turbulence on heat transfer. *Journal of turbomachinery*, *129*(3), 542-550.